

DECK THE WALLS: CURVATURE-MEDIATED ASSEMBLY IN CONFINED
NEMATIC LIQUID CRYSTALS

Yimin Luo

A DISSERTATION

in

Chemical and Biomolecular Engineering

Presented to the Faculties of the University of Pennsylvania

in

Partial Fulfillment of the Requirements for the

Degree of Doctor of Philosophy

2018

Supervisor of Dissertation

Kathleen J. Stebe, Deputy Dean for Research and Richer and Elizabeth
Goodwin Professor of Engineering and Applied Science

Graduate Group Chairperson

John C. Crocker, Professor of Chemical and Biomolecular Engineering

Dissertation Committee

Francesca Serra, Assistant Professor, Department of Physics and Astronomy, Johns
Hopkins University

John C. Crocker, Professor of Chemical and Biomolecular Engineering

Robert A. Riggelman, Associate Professor of Chemical and Biomolecular Engineering

DECK THE WALLS: CURVATURE-MEDIATED ASSEMBLY IN CONFINED
NEMATIC LIQUID CRYSTALS

© COPYRIGHT

2018

Yimin Luo

To my parents.

ACKNOWLEDGEMENT

I would like to thank my thesis advisors, Professor Kathleen J. Stebe and Professor Francesca Serra for guidance throughout my doctorate studies. Francesca worked alongside me during the initial stage of my PhD as a postdoc and that was very special. My thesis topic is very exploratory and would have been unmanageable without both of their visions and knowledge bases. They have both worked extremely hard and motivated me especially during hard times. They have also advised me closely both within and outside of research, including the extremely stressful postdoc search towards the end. I will strive to be the type of mentors they both have been to me as I go down my path of teaching and research.

I would like to thank Professor John Crocker and Professor Rob Riggelman for being great teachers and for serving on my thesis committee. They have been so accessible over the course of my time at Penn that I can easily pick on their brains just by knocking on their doors.

I have also like to thank faculty members who do not advise me directly but are always generous with their time in providing me with guidance for my research and career: Professor Daeyeon Lee, Professor Randall Kamien and Professor Shu Yang.

My experimental work would not have been possible without my long-time simulation collaborator, Dan, for being some responsive in modifying the code and answering my questions.

I wish to thank my professors and mentors from Rice, who always give me incredible advice and guidance: Professor Stan Dodds, Professor Matteo Pasquali, Professor Anson Ma (currently at UConn), Dr. Francesca Mirri (currently at Saint-Gobain), and Dr. Vida Jamali (currently at UC Berkeley).

I have relied on having access to shared facilities to perform characterization and microscopy. Special thanks to Jamie and Matt at Singh Center for SEM and AFM training and Andrea and Jasmine at CDB Microscopy Core for confocal microscopy training.

The secretaries and business administrators at CBE and Towne, past and present, Tamika, Aiasha, Jamie, Denice, Erin, Stacy, Charlotte, Jackie, Donald and Dawn, also played an integral role in my PhD study. They helped me out of countless situations, helped me with payroll and reimbursement and I could not have made it out without them.

My CBE cohort, Jyo Lyn, Sangkyun, Brad, Chen, Daming, Gang, Alok, JaeMin, David, and Tzia-Ming, has made the transition from undergrad to graduate school so much easier. I wish you guys the best in your future endeavors. My officemates, Robert, Chris, Amruthesh, Jennifer and Emily, have made time at work go by fast and provided great conversations.

I would like to thank past and present members of the Stebe lab: Iris, Ningwei, Liana, Sarah, Nate, Mehdi, Jiayi, Giuseppe DV, Giuseppe B, Nick, Sam, Yang, Xu, Caroline, Wilfredo, Tianyi, Renjing, Alismari, Neha, Martin, Lisa, Laura, Tagbo, Nima, Rohini, Mohamed, and Giulia. I am so glad that our paths have crossed, and you have made my journey infinitely easier. Special thanks to Iris, Ningwei and Mohamed for helping and training me in the first two years, Laura for idea-spinning, Sam from Baumgart Lab for handling ellipsoids, Hye-Na from Yang Lab for SEM help. I would also like to thank Denise and Ed at GRASP lab for working with magnets, Naik and Ani for path-planning, Brian and Nader for crash course on optics, and many useful discussions.

My life in Philadelphia would not have been the same without my friends, Sonia, Christine, Patrick, Margret, Kristen, Debbie, Lufei, Jen, Henry, Mary, Alex, Jimin, Ed, Valerie, Parul, Rosie, Jin A, Kathy, and Jacky. Thank you for home-cooked breakfast, birthday celebrations, Fourth of July barbecue, rock-climbing, clamming, s'mores, deer jerky, cooking lessons, taco festival, sailing, dim sum, corn maze, restaurant weeks, and many awesome things I cannot remember right now. All in all, I am grateful to have you guys in my life. You guys watched me through many lowest of the lows and celebrated my highest of highs. I am thankful for my friends who live outside of Philadelphia I can still go to for advice, crash with when I travel and hang out at conferences, Anjie, Wendy, Yijie, Yuan, Sarah, Hazzel, Victor, Ryan, Steve and Elaa. I would like to thank Mengyang (Michael) for being

a constant source of motivation and inspiration.

I cannot thank my Waller (Texas) family enough, Iris, Julissa, Anthony and Welita, who are the reason why I came to this country at age 16, and who have always been there for me (with fresh huevos con salsa).

Finally, I am deeply indebted to my parents, who cross the Atlantic Ocean year after year to spend time with me because I cannot go home regularly. I am eternally grateful for their sacrifice and support; for being my beacon and my sanctuary; for their understanding and generosity; and above all, for having faith in me before I have faith in myself.

Faith consists in believing when it is beyond the power of reason to believe.

-Voltaire

ABSTRACT

DECK THE WALLS: CURVATURE-MEDIATED ASSEMBLY IN CONFINED NEMATIC LIQUID CRYSTALS

Yimin Luo

Kathleen J. Stebe

Tailoring particle interaction among individual building blocks remains an important challenge in a bottom-up assembly scheme. Elastic interactions in anisotropic fluids can be harnessed for this goal. For my thesis, I am particularly interested in investigating the role of confined liquid crystals as a dispersing medium in driving particle assembly. Nematic liquid crystals (NLCs) are made of rod-like molecules that tend to co-align with their neighbors, in a field called the director field. Anchoring refers to the orientation of the NLC molecules at the boundary. Elasticity arises where the molecules deviate from the director field, in three modes of distortion, splay, twist and bend. When a continuous director field cannot be present everywhere, topological defects form, resulting in small melted regions where the order parameter is undefined. It is well-known that particle with perpendicular anchoring generates associated defects, in the form of a Saturn ring or a dipole. These particles have unique symmetry, analogous to electrostatics.

A wall with homeotropic anchoring repels a colloid with the same anchoring; yet by changing the surface topography from planar to concave, one can turn repulsion into attraction. This study is inspired by biology, in the so-called “lock-and-key” interaction. I demonstrate the ability to design precise docking sites, near an undulated boundary with peaks and valleys, for both Saturn rings and dipoles. The domain is engineered to be defect-free in order to avoid strong trapping sites. By tailoring wall curvature, I define sites of attraction and equilibrium loci for colloids that vary from near contact to several particle radii from the boundary. Particles dock in wells of similar radii obeying simple geometric argument

that allows particle to maximize splay and bend matching. Wells of large radius stabilized colloids with a distorted Saturn ring. In certain cases, Saturn rings transform to dipolar configurations driven by wall interactions. I can also define sites of repulsion to propel colloids away from these boundaries and find unstable loci from which colloids depart along multiple paths. Small perturbations of colloid position allow selection among these paths. Colloids with different defects interact distinctly with these boundaries, depending on their near field director field. Finally, I demonstrate the ability of a colloid in motion, like “Goldilocks”, to select from wells of different sizes for preferred docking. Landau de Gennes (LdG) simulations, the standard numerical method in solving for the director field without prior knowledge of the position of the defect, are useful tools in elucidating our experimental findings. We have expanded the work to simulate dipoles, as well as mapping the energy landscape to calculate force field to corroborate experimental trajectories.

These docking sites are useful tools in building structures. I have observed “eyelashes”, topological dipole chains that follow the local, curved director field. These beget wires that connect the groove corners to topographical features on the cell lid to yield oriented, curvilinear colloidal wires spanning the cell, following the curvature of the director field. As the groove aspect ratio changes, I find different ground states, including the ones that contain defect lines which compete with the corner. Anisotropic particles are natural extension to the spherical particles. I have also shown that ellipsoids have distinct energy landscape that depends on both their aspect ratio and orientation. The interaction relies on near-field director field matching rather than strength of particle-sourced distortion, thus the platform has the potential to be scaled down for nanoscale manipulation.

In summary, I study how to guide the formation of reconfigurable structures in NLCs. This was achieved by using boundaries to mold the director field. Docking sites can be exploited for structure formation, such as wiring along the director field. Directing particles toward or away from boundaries provides new tools to steer colloid motion. The abilities to transform defect configuration allows for nano-manufacturing in the defect site.

TABLE OF CONTENTS

ACKNOWLEDGEMENT	iv
ABSTRACT	vii
LIST OF ILLUSTRATIONS	xiv
CHAPTER 1 : Introduction	1
1.1 Motivation	1
1.2 Liquid crystals	3
1.2.1 Topological defects	4
1.2.2 Q-tensor theory	10
1.2.3 Types of LC phases	13
1.3 Particle assembly in nematic liquid crystals	15
1.4 Outline of Thesis	16
CHAPTER 2 : Materials & Methods	19
2.1 Experimental details	19
2.1.1 Photolithography	20
2.1.2 Surface functionalization	22
2.1.3 Particle treatment and synthesis	24
2.1.4 Cell fabrication and sample preparation	27
2.1.5 Imaging	29
2.1.6 Applying a magnetic field	32
2.2 Simulations	32
2.2.1 Landau deGennes (LdG) simulations	32
2.2.2 COMSOL simulation	39

CHAPTER 3 : Lock-and-key interaction in nematic liquid crystals	42
3.1 Background: Lock-and-key interaction	42
3.2 Defect-free system as a system for colloidal assembly	43
3.3 Docking behaviors of particle with Saturn ring defect	48
3.4 More detailed drag analysis	53
3.5 Docking behaviors of particles with hedgehogs	56
3.6 The effect of wall geometry on colloidal behaviors	57
3.7 Conclusions	58
 CHAPTER 4 : Energy landscape near an undulated boundary	 61
4.1 Colloidal assembly in elastic energy landscape	61
4.2 Attraction to well	63
4.3 Modeling the effect of confinement	65
4.4 Equilibrium position: Splaying matching and distorted Saturn rings	66
4.5 Dynamics of quadrupole-to-dipole transition	70
4.6 Simulation of quadrupole-to-dipole transition	72
4.7 Saturn ring as manufacturing site	77
4.8 Multiple stable states for particles of various defect types	78
4.9 Bistable docking of Saturn rings and dipoles	81
4.10 Site selection under the influence of gravity	82
4.11 Conclusions	86
 CHAPTER 5 : Wiring particles along director field	 88
5.1 Colloidal wiring and structure formation in nematic liquid crystals	88
5.2 Wide grooves	89
5.3 Point-to-point wiring of particles	92
5.4 Dynamics of the assembly	93
5.5 Particle-corner interaction	94
5.6 Narrow grooves	96

5.7	Fluorescent Confocal Polarizing Microscopy (FCPM)	99
5.8	Simulations	100
5.9	Conclusion	103
CHAPTER 6 : Open issues		105
6.1	Ellipsoids	106
6.1.1	Isolated ellipsoids	107
6.1.2	Behaviors of ellipsoids near walls	108
6.1.3	Rotation	112
6.2	Asymmetry of particle behaviors near ratchet-like surface	114
6.3	Hanging chains near sharp features	117
6.4	Scaling down lock-and-key	120
6.5	Assembly in other LC phases	123
CHAPTER 7 : Conclusion and outlook		124
Appendix A		127
Appendix B		130
BIBLIOGRAPHY		138

LIST OF ILLUSTRATIONS

FIGURE 1.1 : The liquid crystalline phase	3
FIGURE 1.2 : Distortions in liquid crystals	3
FIGURE 1.3 : Gauss’s Theorem and Poincaré Theorem	7
FIGURE 1.4 : Homeotropic colloids and their assemblies	9
FIGURE 1.5 : The laboratory frame and the local frames of reference	11
FIGURE 1.6 : Other liquid crystal phases	14
FIGURE 2.1 : Wavy wall cell fabrication	21
FIGURE 2.2 : Groove cell	22
FIGURE 2.3 : Colloid treatment with strong hometropic anchoring condition	24
FIGURE 2.4 : Synthesized particles	27
FIGURE 2.5 : Lipids partition into defects	30
FIGURE 2.6 : Schlieren texture under crossed-polarizers	31
FIGURE 2.7 : Mapping the energy landscape by sampling and calculating particle trajectories by force field	36
FIGURE 2.8 : COMSOL outputs	41
FIGURE 3.1 : Cell fabrication	47
FIGURE 3.2 : Experimental realization of the lock-and-key interaction	49
FIGURE 3.3 : Trajectory analysis	51
FIGURE 3.4 : Drag coefficients	54
FIGURE 3.5 : Docking of dipoles	57
FIGURE 3.6 : Colloids in wells of different dimensions.	58
FIGURE 4.1 : Colloid-wall interaction range versus wavelength λ	64
FIGURE 4.2 : Confinement truncates the decay length of wall perturbations in the director field	66

FIGURE 4.3 : Particle-wavy wall interactions	67
FIGURE 4.4 : Energy of the quadrupole and dipole in wells	69
FIGURE 4.5 : Dynamics of the quadrupole to dipole transition	71
FIGURE 4.6 : Simulated energy density for dipole and quadrupole near a wavy boundary	74
FIGURE 4.7 : Simulation of total energy of the system E versus the reaction co- ordinate θ	75
FIGURE 4.8 : Simulated energy density for dipole and quadrupole near a wavy boundary	76
FIGURE 4.9 : Defects as template for assembly	78
FIGURE 4.10 : Multiple states and reconfigurable docking	80
FIGURE 4.11 : Equilibrium distance of particles away from a flat homeotropic wall	82
FIGURE 4.12 : Repulsion and bistable docking of dipoles and Saturn rings	83
FIGURE 4.13 : A “Goldilocks” colloid in motion docks in a preferred well	85
FIGURE 5.1 : A single eyelash	90
FIGURE 5.2 : Curvilinear assembly forming eyelashes and wires in confined cells	91
FIGURE 5.3 : Cell-spanning wires created by imposing topographical cues	93
FIGURE 5.4 : Dynamics of assembly for eyelashes	95
FIGURE 5.5 : Far- and near- field attraction	95
FIGURE 5.6 : Attraction of the corner	96
FIGURE 5.7 : Transition from eyelashes along director field to strings of colloids along disclination lines	97
FIGURE 5.8 : Iso-nematic transition in narrow channels	98
FIGURE 5.9 : FCPM measurements with 5CB and CCN mixture	101
FIGURE 5.10 : Simulation of channels of different aspect ratio	102
FIGURE 6.1 : Ellipsoids and their defects	108
FIGURE 6.2 : The self-assembly of ellipsoids	109

FIGURE 6.3 : Anisotropy docking behavior of ellipsoids	110
FIGURE 6.4 : Anisotropy docking behavior of higher AR ellipsoids	111
FIGURE 6.5 : Time lapse video of a ellipsoid docking inside a deep well	112
FIGURE 6.6 : Rotation of ellipsoids with dipolar defects	113
FIGURE 6.7 : Energy landscape near a ratchet surface	115
FIGURE 6.8 : Trajectories of particles near a ratchet surface	116
FIGURE 6.9 : NLC near walls with sharp features	117
FIGURE 6.10 :Formation of defect line at phase transition	118
FIGURE 6.11 :Different behaviors of chains get entangled on the structure with different angle	119
FIGURE 6.12 :Scaling down of the lock-and-key interaction	122
FIGURE 7.1 : Concept map	126

Chapter 1

Introduction

1.1. Motivation

To realize new materials from microscale building blocks, new strategies are needed to direct assembly of reconfigurable, hierarchically organized structures with non-trivial arrangements that apply to broad ranges of materials.

There are approaches to fabricating materials that include microscale elements. Top-down schemes use processes like additive manufacturing or lithography to build microscale objects from a particular material at a particular location. In contrast, bottom up self-assembly schemes use colloidal building blocks with interactions similar in magnitude to thermal energies to make organized structures [17, 18]. The structures that emerge rely on the geometry of the building blocks and the distribution of features on them, so objects that are faceted or patchy assemble differently from spheres. Directed assembly relies on interactions between colloidal building blocks that are far greater than thermal energies. These energies are often generated via application of external fields that interact with particular materials properties of the colloids. For example, polarizable particles in external electrostatic fields interact via dipolar interactions to form chains oriented along field lines. Fabrication through directed assembly can provide a route to create and control hierarchical materials via scalable processes that might be practical to implement.

In recent years, new strategies for directed assembly have been developed that do not rely on particular material properties, but rather on interactions that emerge when colloids are

placed in soft matter. To accommodate the particle, the soft medium distorts. The distortion has an associated energy field that drives particle assembly. Furthermore, if the host medium is globally deformed, *e.g.* within a confining vessel, the distortion made by the particle interacts with the global field to organize particles over large domains. These ideas have been demonstrated in several media. For example, proteins adhered to lipid bilayers interact to minimize distortions made by the proteins. The adhered proteins perturb membrane curvature, and assemble to minimize this perturbation [38, 109]. Colloidal particles on curved lipid bilayers [58] and particles at curved fluid interfaces are other motivating examples. The particles change the area of the membrane or interface, with energetic consequences. Because this area perturbation depends on the curvature field, particles migrate along curvature gradients to minimize the distortion.

The aim of this thesis is to extend these concepts to confined liquid crystals. The understanding of colloidal assembly in nematic liquid crystalline hosts has been developing at a rapid pace since the seminal work of Poulin [85, 102], as reviewed, for example in Refs. [54, 73]. However, the opportunities for directed assembly that can be achieved by combining nematic LCs with well designed boundaries have been largely unexplored. We focus on two systems that allows assembly in two- and three-dimensions. The first system consists of a nematic liquid crystal (NLC) confined within vessels with wavy boundaries. The second system consists of a nematic liquid crystal (NLC) confined within grooves. In both cases, the confining vessels mold the NLC director field and define an energy landscape. By placing a colloid within this confined NLC, the colloid finds preferred paths and sites for assembly. Since the director field in NLC can be manipulated by changing vessel shape or using external fields, this work defines new routes to make reconfigurable materials.

We explore the analogies and differences between NLC and related interfacial systems and electrostatics systems. In particular, we explore some important consequences of topological defects, absent in the interfacial systems, and present in NLC, and exploit them for assembly.

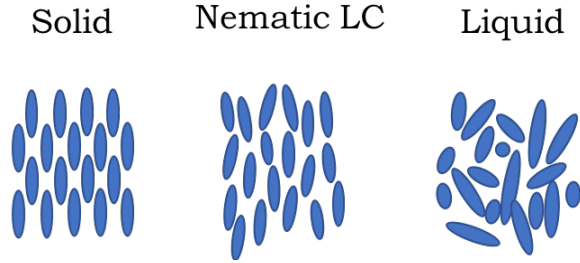


Figure 1.1: The liquid crystalline phase. Liquid crystals consist of rod-like molecules that come in between anisotropic liquids and crystalline solids.

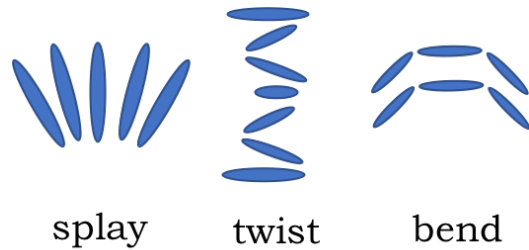


Figure 1.2: Distortions in liquid crystals. The three main types of distortion are splay, twist and bend, which penalize distortion from the director field.

1.2. Liquid crystals

Liquid crystals (LCs) are phases of matter between crystalline solids and disordered liquids (Fig. 1.1). The simplest liquid crystalline phase is the nematic phase, formed by rod-like molecules which co-orient spontaneously to maximize their positional entropy. In the continuum limit, the alignment can be characterized by a headless vector, termed the director \mathbf{n} . Since deviations from this preferred direction cost energy, this spontaneous alignment gives rise to elasticity, manifested in three primary modes of distortion in bulk: splay, twist and bend (Fig. 1.2, [29]). The Frank elastic free energy density f_b in bulk is described by Eq. 1.1:

$$f_b = \frac{1}{2}K_1(\nabla \cdot \mathbf{n})^2 + \frac{1}{2}K_2(\mathbf{n} \cdot \nabla \times \mathbf{n})^2 + \frac{1}{2}K_3(\mathbf{n} \times \nabla \times \mathbf{n})^2 \quad (1.1)$$

where K_1 , K_2 and K_3 are the splay, twist and bend elastic constants. In commonly studied NLCs, these constants are of similar order of magnitude. For simplification, in the one-

constant limit, they are assumed to be equal, $K_1 = K_2 = K_3 \sim 10^{-11}N$. The total free energy is the sum of surface energy and bulk distortion (Eq. 1.2):

$$F = \int_S f_s dS + \int_V f_b dV \quad (1.2)$$

The surface distortion is expressed by Eq. 1.3:

$$f_s = W(\mathbf{n} \cdot \boldsymbol{\nu})^2 \quad (1.3)$$

where W is the anchoring strength (expressed in N/m) and $\boldsymbol{\nu}$ denotes the preferred orientation of NLC on the surface.

Surface anchoring refers to the preferred molecular orientation at a bounding surface, and it is typically controlled in experiment by either laying down polymeric commanding layers to induce parallel orientation or by adsorbing surfactant monolayers to impose perpendicular anchoring or homeotropic anchoring. In recent years, even more exquisite control of the anchoring has been achieved by microscale lithography [114], micro-rubbing using an AFM tip [1], and photo-alignment [71, 80, 81].

The ratio of the bulk elastic constant to the surface anchoring is called the extrapolation length $l = K/W$. It roughly describes the distance where the anchoring of a particular surface decays away. For typical anchoring strength $K \approx 10^{-11} N$ and $W \approx 10^{-5} J m^{-2}$, $l \approx 1 \mu m$. For colloids radius $a \ll l$, the director field remains uniform at the cost of the boundary conditions; for $a \gg l$, surface anchoring dominates and particles generate associated topological defects [53], which are reviewed in the next section. Most of the colloids we study are in the μm range, so they carry defects.

1.2.1. Topological defects

Topological defects arise due to frustration of the director field. They are small melted regions where the scalar order parameter S vanishes. S is defined as:

$$S = \langle 3\cos^2\theta - 1 \rangle \quad (1.4)$$

where θ denotes the angle between the molecules and the local nematic director.

Defects are characterized by their topological charge, which in two dimensions coincides with the winding number. The winding number is defined conventionally as the angle by which the director \mathbf{n} rotates around the defect, divided by 2π . In the example above, at the poles of the sphere, the director rotates by 2π , therefore its charge is $+1$. Nematic liquid crystals also allow defects with semi-integer charges ($\pm\frac{1}{2}$).

The concept of topological charge also applies in the three dimensions. However, in this case, it is not defined in terms of the winding number. For NLC, since the director is represented by a headless vector ($\mathbf{n} \equiv -\mathbf{n}$), the order parameter space, *i.e.* all possible realization of the director field, is the projective plane (P2). The charge N is calculated by considering the direction of \mathbf{n} along the surface of a small volume that includes the entire defect. N is defined as the solid angle spanned by the director field on the P2 plane. Formally, the topological charge N is calculated by carrying out the integration on the P2 sphere surrounding the defect [53]:

$$N = \frac{1}{4\pi} \iint \left(\frac{d\theta}{du} \frac{d\phi}{dv} - \frac{d\phi}{du} \frac{d\theta}{dv} \right) \sin\theta dudv \quad (1.5)$$

where we parameterize the director field as:

$$\mathbf{n} = \{ \sin\theta \sin\phi, \sin\theta \cos\phi, \cos\theta \} \quad (1.6)$$

where the azimuthal angle ϕ and polar angle θ are specified on the P2 sphere.

In systems with the same topology, the total charge is conserved. For example, a uniform

director field has no defects and zero total charge. The charge of the defect is related to the topology of the object. Two objects are said to have the same topology when one can be continuously transformed to the other. For instance, a sphere has the same topology as a tetrahedron, a cube and a icosahedron. It is useful to define the Euler characteristic of the object:

$$E = \textit{vertices} + \textit{face} - \textit{edges} \tag{1.7}$$

All the the objects mentioned above have Euler characteristic $E = 2$. Another way to define the topology is through the concept of genus. Genus is related to Euler characteristic in the following way:

$$E = 2(1 - g) \tag{1.8}$$

It is best understood as the number of holes an object has, but can be generalized into more complex geometries. Spheres, tetrahedrons, cubes, and icosahedrons all have $g = 0$. On the other hand, a coffee mug and a donut both have $g = 1$.

With the concept of Euler characteristic, we are now ready to introduce the Gauss's Theorem, which applies to an object with homeotropic anchoring. Gauss's Theorem states that the total charge m_i within an object is equal to half of its Euler's characteristic E :

$$\sum m_i = E/2 \tag{1.9}$$

By introducing into this system a sphere with homeotropic anchoring one essentially introduces a charge of $m_i = +1$ in the system originally free of defect (Fig. 1.3a), so a companion defect must form of charge -1 .

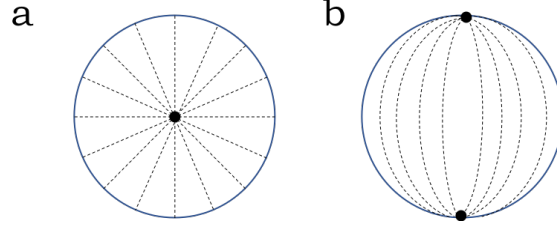


Figure 1.3: Gauss's Theorem and Poincaré Theorem. (a) Particle of homoetropic anchoring introduces charges sum up to half of the Euler's characteristic inside. (b) Particles with planar anchoring introduces charges that sum up the Euler's characteristic at its exterior.

The companion defect can be in the form of a point defect (Fig. 1.4a), also called a hedgehog, or of a disclination line encircling the particle, also called a Saturn ring (Fig. 1.4b). These two configurations are topologically equivalent with charge -1 . Intuitively, we can see that the ring can shrink into a point. While the total topological charge of particle and associated defect is always zero, the energetics of hedgehogs and Saturn rings are very different. There are electrostatic analogies for these objects in the far-field. In the limit of small slopes and weak gradients in the director field in the one-constant approximation ($K = K_1 = K_2 = K_3$), the associated Euler-Lagrange equation that governs the spatial dependence of each component of the director field can be shown to reduce to Laplace's equation. I show this briefly here for a one dimensional spatial dependence by finding the function $f(x)$ that maximizes or minimizes a given functional I subject to certain constraints, *e.g.* $f(a) = A$ and $f(b) = B$. Suppose L , the integrand function, is twice differentiable. The functional to be maximized or minimized is I :

$$I = \int_a^b L(x, f(x), f'(x)) dx \quad (1.10)$$

The Euler-Lagrange Equation for $f(x)$ is specified:

$$\frac{\partial L}{\partial f} - \frac{d}{dx} \cdot \frac{\partial L}{\partial f'} = 0 \quad (1.11)$$

Now consider the free energy density of the bulk elasticity under the single elastic constant

approximation, Eq. 1.1 can be simplified to have the form:

$$\begin{aligned} f_b &= \frac{1}{2}K[(\nabla \cdot \mathbf{n})^2 + (\nabla \times \mathbf{n})^2] = \frac{1}{2}(\partial_\alpha n_\beta)^2 \\ f_b &= \frac{1}{2}K(\nabla n_x)^2 + \frac{1}{2}K(\nabla n_y)^2 + \frac{1}{2}K(\nabla n_z)^2 \end{aligned} \quad (1.12)$$

In the absence of bulk topological defects, the total free energy is minimized by integrating the bulk elastic density, thus, we choose the integrand function L :

$$L = \frac{1}{2}(\nabla n_x)^2 = \frac{1}{2} \left(\frac{\partial n_x}{\partial x} + \frac{\partial n_x}{\partial y} + \frac{\partial n_x}{\partial z} \right)^2 \quad (1.13)$$

the Euler-Lagrange Equation (Eq. 1.11) that contains a single function with multiple variables is expressed as the following:

$$\frac{\partial L}{\partial f} - \sum_{j=1}^n \frac{\partial}{\partial x_j} \cdot \frac{\partial L}{\partial \frac{\partial f}{\partial x_j}} = 0 \quad (1.14)$$

The partial derivatives are:

$$\frac{\partial L}{\partial f} = 0 \quad (1.15)$$

$$\begin{aligned} \frac{\partial L}{\partial \frac{\partial f}{\partial x}} &= \frac{1}{2} \cdot 2 \left(\frac{\partial n_x}{\partial x} + \frac{\partial n_x}{\partial y} + \frac{\partial n_x}{\partial z} \right) \frac{\partial \left(\frac{\partial n_x}{\partial x} + \frac{\partial n_x}{\partial y} + \frac{\partial n_x}{\partial z} \right)}{\partial \frac{\partial n_x}{\partial x}} \\ &= \left(\frac{\partial n_x}{\partial x} + \frac{\partial n_x}{\partial y} + \frac{\partial n_x}{\partial z} \right) = \nabla n_x \end{aligned} \quad (1.16)$$

$$\frac{\partial L}{\partial \frac{\partial f}{\partial y}} = \frac{\partial L}{\partial \frac{\partial f}{\partial z}} = \nabla n_x \quad (1.17)$$

Substitute into Eq. 1.14 to get:

$$\left(\frac{\partial}{\partial x} + \frac{\partial}{\partial y} + \frac{\partial}{\partial z} \right) \cdot \nabla n_x = 0 \quad (1.18)$$

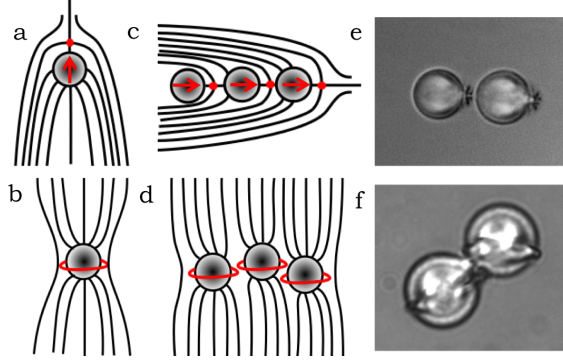


Figure 1.4: Homeotropic colloids and their assemblies. Sketches of (a) hedgehog (b) Saturn ring (c) dipoles assemble in linearized fashion, red arrows denote direction of the dipole (d) Saturn rings assemble in zig-zag manner. The defect structures are shown in red. Bright field microscopic images showing the assemblies of a pair of colloids with (e) dipolar defect and (f) Saturn rings.

The outcome of Euler-Lagrange is that the director field obeys the Laplacian:

$$\nabla^2 n_x = 0 \quad (1.19)$$

Thus, the distortion fields in the small distortion limit obeys Laplace's equation, and is described by a multipole expansion. Far from the particles, the particle-hedgehog pair is a dipole and the particle with Saturn ring is a quadrupole, with associated algebraically decaying fields. Like their electrostatic counterparts, the dipoles assemble head-to-tail (Fig. 1.4c, [65]), and the direction of the dipole is denoted by red arrows in Fig. 1.4d; while the quadrupoles assemble in a zig-zag manner (Fig. 1.4d). Experimental images of assemblies of a pair of dipoles and a pair of quadrupoles are shown in Fig. 1.4e, f.

For a particle with planar anchoring (Fig. 1.3b), Poincaré Theorem provides important insight. This theorem states that an object with director field that conforms to its surface introduces charges that sum up to:

$$\sum m_i = E \quad (1.20)$$

For particles with planar anchoring, the most commonly observed configuration is the bipolar state, with two -1 defects, called “boojums” located at the two poles. The boojum colloids also behaves as quadrupoles, and assemble in a zig-zag manner. Surface defects like boojums stay on the surface while Saturn rings and hedgehogs can move to a distance away and pin to objects in space.

1.2.2. *Q-tensor theory*

In this thesis, in order to model the behavior of the nematic liquid crystal, we simulate the director field using a numerical code in which the minimum energy configuration for the nematic liquid crystal is determined based on Q-tensor theory. The main concepts of Q-tensor theory are reviewed here in a discussion adapted from [72]. This approach uses a phenomenological model that uses a tensorial order parameter \mathbf{Q} to describe the biaxial ordering of the molecules. Instead of having fore-and-aft symmetry, like a cylinder, a biaxial molecule is like a plank of wood. A biaxial molecule has no rotational symmetry, but does have reflection symmetry. Similarly, the arrangement of a molecule can be either uniaxial or biaxial. This is a more nuanced concept: the easiest way to understand is to related back to the concept of the order parameter that was defined in Eq. 1.4. For each direction, we might find the projection of all molecules on the perpendicular plane and define a scalar order parameter S_1 , S_2 and S_3 . It can be shown that the S_3 can be derived from S_1 and S_2 . For a uniaxial arrangement of the molecule, two of the three order parameters are equal (and the remaining one is zero); while in a biaxial arrangement, all three of them are distinct. Instead of defining the director \mathbf{n} , now we may define an additional set of perpendicular axis \mathbf{m} , along which the shorter axis of the molecule aligns, while the third can be obtained by $\mathbf{n} \times \mathbf{m}$. It is assumed, without loss of generality that the director has unit length: $|\mathbf{m}| = |\mathbf{n}| = 1$. To understand the Q-tensor model, we must first understand that it uses the most general model of nematics, which is the biaxial arrangement of uniaxial molecules. This model is used because it is related to the structure inside the defect. Thus, the arrangement of the molecule anywhere within the system can be fully described by S_1 ,

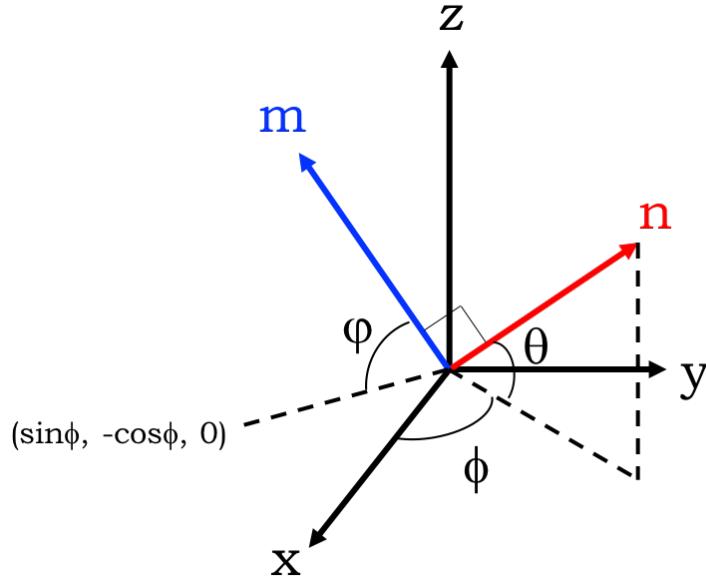


Figure 1.5: The laboratory frame and the local frames of reference. (x, y, z) denotes the laboratory frame, while \mathbf{n} , and \mathbf{m} are expressed in terms of θ , ϕ and ψ in the local frame of reference.

S_2 , \mathbf{n} , and \mathbf{m} . To understand this order, it is helpful to have two frames of reference: a laboratory frame (x, y, z) and a local frame $(\mathbf{m}(\mathbf{r}, t), \mathbf{n}(\mathbf{r}, t))$ (Fig. 1.5). The directors can be described by three angles θ , ϕ and ψ , these values are depended on where we are in the sample, the location is denoted by \mathbf{r} .

$$\mathbf{n} = (\cos\theta\cos\phi, \cos\theta\sin\phi, \sin\theta) \quad (1.21)$$

$$\mathbf{m} = (\sin\theta\cos\psi - \sin\psi\sin\theta, -\sin\phi\sin\psi\sin\theta - \cos\phi\cos\psi, \sin\psi\cos\theta) \quad (1.22)$$

A theory can be formed by five variables: $\theta(\mathbf{r}, t)$, $\phi(\mathbf{r}, t)$ and $\psi(\mathbf{r}, t)$, $S_1(\mathbf{r}, t)$, and $S_2(\mathbf{r}, t)$. Instead of writing these parameters, we will now take the mean square projections of the dyadic product to obtain a 3x3, symmetric, and traceless matrix \mathbf{Q} that contains all infor-

mation of the director field:

$$Q_{\alpha\beta} = S_1 n_\alpha n_\beta + S_2 m_\alpha m_\beta - \frac{1}{3} \delta_{\alpha\beta} \quad (1.23)$$

The eigenvector and corresponding largest eigenvalue are: \mathbf{n} , the director field, and S :

$$S = \frac{1}{3}(2S_1 - S_2) \quad (1.24)$$

for $S_1 > S_2$. In the uniaxial limit, local selection of \mathbf{m} disappears, $S_2 = 0$ and $S_1 = \frac{3}{2}S$ and:

$$Q_{\alpha\beta} = \frac{3}{2}S(n_\alpha n_\beta - \frac{1}{3}\delta_{\alpha\beta}) \quad (1.25)$$

The system free energy can now be expressed in terms of Q-tensor, the bulk term F_{LdG} and contribution of the surface terms Φ_s :

$$F = F_{LdG} + \sum_s \Phi_s \quad (1.26)$$

The surface anchoring is expressed:

$$\Phi_s = W_0^s \int dA \text{tr}(\mathbf{Q} - \mathbf{Q}^B) \quad (1.27)$$

where W_0^s is the anchoring strength and \mathbf{Q}^B is the preferred orientation at the surface of the boundary. The bulk term is expressed:

$$F_{LdG} = \int (f_{phase} + f_d) dV \quad (1.28)$$

where f_{phase} is the phase term that stabilize the nematic phase against the isotropic phase, and f_d is the energy density of the elastic distortion:

$$f_{phase} = \frac{1}{2} A \text{tr} \mathbf{Q}^2 + \frac{1}{3} B \text{tr} \mathbf{Q}^3 + \frac{1}{4} C [(\mathbf{Q}^2)]^2 \quad (1.29)$$

where the A term drives the transition, which depends on temperature, the B term guarantees the asymmetry of S , and the third term bounds the values of S . These are the minimum number of terms needed to describe the transition. f_d uses scalar invariants of the Q-tensor to penalize the elastic distortions, with single elastic constant approximation:

$$f_d = \frac{L}{2} \frac{\partial Q_{ij}}{\partial x_k} \frac{\partial Q_{ij}}{\partial x_k} \quad (1.30)$$

where L is the non-dimensionalized elastic constant $L = \frac{2}{9} \frac{K}{S^2}$.

This phenomenological approach allows both μm scale modeling of the distortion as well as sub- μm -scale modeling of the defect.

1.2.3. Types of LC phases

There are several different LC phases. While these other phases are not the subject of research of this thesis, we included them here to give context to possible extension, which will be discussed later in this thesis.

The cholesteric phase can be generated by introducing a chiral dopant to the simplest nematic phase (Fig. 1.6a), which favor twist. The director field \mathbf{n} twists in space. Let \hat{z} be the helical axis, \mathbf{n} has the following form [29]:

$$\begin{cases} n_x = \cos(q_0 z + \phi) \\ n_y = \sin(q_0 z + \phi) \\ n_z = 0 \end{cases} \quad (1.31)$$

Since the director is headless, the spatial period is half of the pitch. Temperature, chemical composition, and external fields are known to influence the pitch size. Cholesterics can also adjust their pitch slightly based on boundary. Confinement has been shown to be able to modify cholesteric textures [33]. The common method to measure pitch is by making a Grandjean-Cano wedge cell [100].

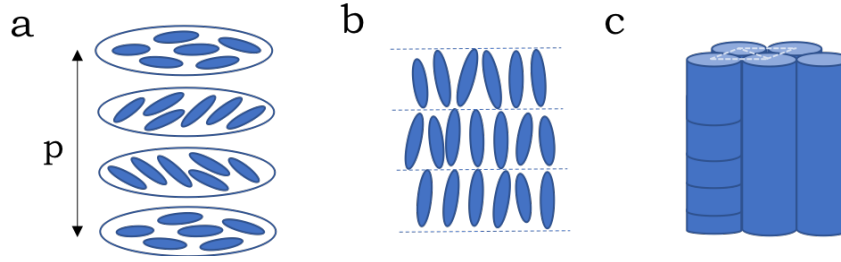


Figure 1.6: Other liquid crystal phases. (a) Cholesterics. (b) Smectic A. (c) Columnar.

The ability to adapt to local boundary and spontaneously twist have lead to efforts in using cholesterics as template colloidal assemblies, such as by using arrays of disclination line at cholesteric-oil interface [61]. The conflict between anchoring and bulk distortion is more pronounced in cholesterics than in nematics, as has been shown in many experimental settings (droplets [79], shells [19], tori [25], *etc.*).

Smectic A phase consists of layered structure (Fig. 1.6b). Within each layer, orientational order persists while positional order is only in one-dimension. Splaying of the molecule is equivalent to bending of the layers, while keeping the layers parallel to each other. Bend mode is not allowed in smectics because that would disrupt the layer spacing. Under conflicting boundary conditions, *i.e.* one planar and one homeotropic surface, defects are formed instead. They form because of energy, rather than topology. One type of defects is the “oily-streaks”, one-dimensional, parallel defect domains, which occur for a thin film on flat surface with uniform planar anchoring, while the other side in contact with air, which has homotropic anchoring [118]. On the other hand, focal conic domains (FCDs) form with the random anchoring on one surface and homeotropic on the other surface.

Columnar phase are also called “calamitic” or “discotic”. The disks form stacks of columns which are arranged in a hexagonal lattice (Fig. 1.6c), while the disk themselves in the columns have irregular spacing [29]. The discussion of columnar phase is beyond the scope of this thesis. But the stacks behave as the rods in nematic phase.

1.3. Particle assembly in nematic liquid crystals

Nematic liquid crystals (NLCs) are excellent candidates as a dispersing medium for a bottom-up assembly approach. NLCs distort near boundary and around particles. Their anisotropy gives rise to long-range, complex behaviors. The elastic energy landscape provides strong guidance ($Ka \sim 10^4 k_B T$ for colloids of radius $a = 1 \mu m$) to position particles, and acts in long range (several particle radii). Furthermore, the molecular ordering disappears when they are heated above their clearing points, and they behave as isotropic fluid. Therefore, NLCs are also reconfigurable.

However, a global melting strategy seldom leads to a highly regular structure: in isotropic phase, the particles are not kept apart by elastic repulsion, and instead fall into trapped state where their defects becomes an entangled mess. Strategy to induce localized melting in NLC can be realized using azobenzene. The molecule goes from a trans-configuration to a cis-configuration upon irradiation. The transformation disrupts local ordering where the light shines on the sample. It has been exploited for collecting and organizing particles in liquid crystals [50, 57]. By more direct intervention, colloids can be guided into a remarkable array of complex structures by exploiting laser tweezers. These methods rely on “local surgeries”, *i.e.* targeted melting using laser tweezers to help the system find metastable states. Assemblies of remarkable regularity ranging from photonic crystals [73], colloidal wires [88], entangled knots [108], and hierarchical assembly [98] have been formed using this approach. Laser tweezers are fantastic tools to probe inter-particle interaction but they require highly-specialized equipment, personnel training, and are challenging to scale up.

An equally promising route to particle assembly focuses on engineering defects, which can be made to appear predictably by rules of topology around colloids and lithographic features. Topological defects are powerful trapping sites for microscale and nanoscale particles. In many of the systems studied, the particles were drawn to the melted cores irrespective of their surface chemistry, orientation, or geometry and were sequestered in the defect core. For example, a cell-spanning disclination line, created by anchoring conditions that require

its formation, has been used to collect colloids to create a microwire [1, 27]. In recent literature, micro- and nano-particles have been successfully assembled by point and line defects [6, 35, 83]. This is also true for all kinds of defects: Saturn rings [98], point defects of strength $m_i = \pm 1$ in capillary [111], and boojums [113]. The location of these defects can be organized by confinement [2] or by topography [11], so hierarchical assemblies can be formed. For larger colloids, on the order of $10 \mu m$ in diameter, a study on disclination loops tied to a fiber shows that it is possible to sort particles based on the orientation of the colloid and its associated defect and defect type with the disclination loop [74]. Assemblies in defects are seldom reversible. There are interactions within NLC that might allow reversible assembly. For example, particles can assemble at preferred sites on a boundary based on geometrical complementarity via the so-called lock-and-key interaction [97]. We develop this concept further in this thesis. Related methods rely on matching the distortion field made by the particle with the director field. For example, particles can migrate to preferred sites on a surface that has been photo-patterned to dictate regions of splay and bend deformation that match the bend and splay associated with the colloid [80, 81, 82]. This migration and docking at preferred sites depends non-trivially on the host director field. Rather, these effects rely on the colloid surface anchoring, defect configuration, and orientation within these fields.

1.4. Outline of Thesis

My thesis has focused on directed particle assembly in distorted director field. The main objective of this thesis is to find new routes to colloid assembly by imposing boundary and anchoring to mold the director field, which in turn controls the assembly of the colloids within. The director field serves as a platform for particles to interact with each other and with the field to form well-defined structures or migrate to predefined locations. Particles interact via elastic interactions. These interactions depend strongly on the shape of the boundary, as well as particle geometry and surface properties. In this dissertation, we combine experiments and simulations to study the behavior of particles in confined nematic

liquid crystals.

In chapter 2 we describe the experimental techniques used for our work, from the preparation of NLC cells to the observation with polarized microscopy.

In chapter 3 we demonstrate experimentally that the lock-and-key mechanism can robustly localize a particle with Saturn rings and dipoles at specific topographical features. We observe the complex trajectories traced by the particles as they dock on the dales, estimate the binding energy, and explore a range of parameters that favor or disfavor the docking event.

Chapter 4 describes in greater detail the energy landscape near a wavy wall. A microparticle in this field displays a rich set of behaviors, as this system has multiple stable states, repulsive and attractive loci, and interaction strengths that can be tuned to allow reconfigurable states. We relate the equilibrium position of the particles geometric arguments, explore the range of particle-wall interaction, and put forth a detailed analysis of a case where director field rearrangement around the particle leads to unexpected transformation. Finally, we demonstrate that microparticles can move along distinct paths, and select sites for preferred docking.

In the above study, we have worked predominately with a two-dimensional system to allow easy visualization of the trajectories and flexibility in changing the geometry of the boundary. In Chapter 5, we seek strategies to create three-dimensional assembly. Utilizing the edges of square grooves as attraction sites for the particles, we show that particles can wire along a non-singular director field, forming highly regular, curvilinear chains. Furthermore, we demonstrate the ability to control the mode of assembly by changing the geometry of the system.

Chapter 6 identifies opportunities and open questions for future investigation of the field. A natural continuation of this work is to explore how anisotropic particles such as ellipsoids interact with a wavy boundary. Particles of different aspect ratios have distinct energy

landscape near wall. Walls of different symmetry and sharpness are also explored. Finally, we demonstrate that the platform has the potential to be scaled down to nanoscale assembly.

Chapter 7 summarizes the conclusions of key findings in this thesis.

Chapter 2

Materials & Methods

2.1. Experimental details

We are interested in using confinement to mold the director field in a NLC, and placing colloids with controlled anchoring within this director field. We fabricate confining vessels with interesting boundary topography using photolithography, as described in Section 2.1.1. We functionalize particles and bounding surfaces to have appropriate anchoring boundary conditions to control the orientation of NLCs as described in Section 2.1.2. We describe a set of methods we have used to fabricate particles with different shapes, anchoring conditions, and surface roughness in Section 2.1.3. In Section 2.1.4, we describe how SU-8 features are incorporated to make a cell or confining vessel for each geometry studied, and describe some general procedures to prepare the cell for observation.

We are interested in observing particle trajectories in real-time, in deducing the orientation of the director field, and in reconstructing 3D textures. A set of imaging techniques used in this thesis are presented in Section 2.1.5. We use a magnetic field to control the initial position of ferromagnetic colloids. To do this, we have used both permanent magnets and coils, as described in Section 2.1.6.

Simulation is used to guide our thinking. We present the basic framework of Landau de Gennes (LdG) simulation, widely used to compute regions of order and disorder in bounded geometries through a global free energy minimization. In addition, we present specific extension to the model to describe experimental findings pertaining to this thesis in Section

2.2.1. In some cases, we have simulated approximate solutions of the director field using COMSOL to solve the Laplacian to compute particle-free, small-slope director fields, as described in Section 2.2.2.

All chemicals were purchased from Sigma Aldrich unless otherwise specified.

2.1.1. Photolithography

This method, which originated in the semiconductor industry to manufacture microelectronic circuits, is now widely used to fabricate experimental vessels and anisotropic objects with well defined geometries. We primarily use the negative photo-resist epoxy resin SU-8 since it is easy to use and is mechanically and is relatively chemical stable. We also use the negative photoresist KMPR. Negative photo-resists cross-link upon irradiation [20]. By projecting UV light through a patterned mask, illuminated regions of the photo-resist are cross linked, and blocked parts are subsequently etched away. The detailed processing steps, including soft baking or heating of the resist film prior to exposure, and hard baking or heating after exposure, are provided in detail instructions from the manufacturers of the epoxy resin, MicroChem Corp. To define the pattern, the photomask is first drawn with AutoCAD, then translated and printed by CAD/Art Services, Inc.

Wavy wall

In Chapters 3, 4, and 6, we study colloids interacting with NLC adjacent to wavy walls (Fig. 2.1). The walls are confined between parallel plates; all surfaces have well defined anchoring conditions. The wavy walls are made with standard lithographic methods of SU-8 2025 epoxy resin (MicroChem Corp.) on glass coverslips. First, the glass coverslips are plasma etched for 60 seconds prior to lithography. The epoxy resin SU-8 is spin-coated onto the glass substrate (500 rpm for 5 seconds and 4000 rpm for 35 seconds), soft baked (75 °C for 30 minutes, 105 °C for 2 hours and 75 °C for 2 hours) and exposed to 365 nm UV light (OAI Hybralign Series 200) through a photomask with a 70% filter at 140 mJ/cm^2 . The substrate is hard baked at 75 °C for 30 minutes, then at 105 °C for 1.5

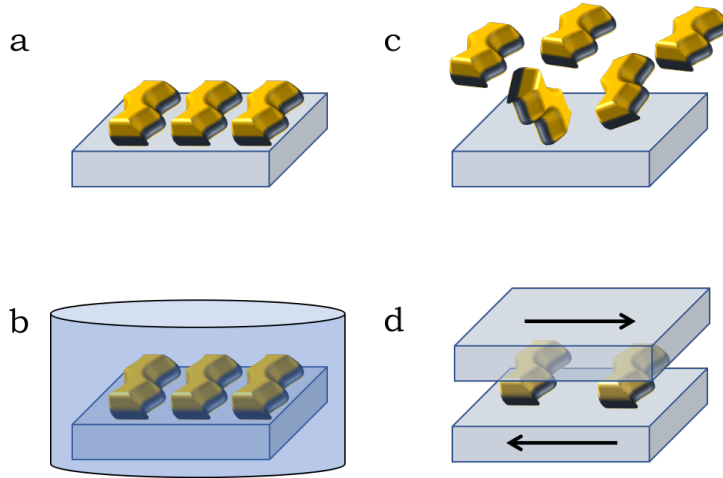


Figure 2.1: Wavy wall cell fabrication. (a) Fabricate the wavy wall on glass coverslips via SU-8 lithography. (b) Treat the structure to have homeotropic anchoring. (c) Liberate the strips by razor blade. (d) Sandwich the wall between two glass slides rubbed in an antiparallel fashion.

hours. Subsequently, the glass substrate is placed in a developer solution (1-methoxy-2-propyl acetate, MicroChem Corp.) to remove the regions that have not been cross linked. We explore wavy walls with a variety of geometries. For example, in one study, we study colloidal interaction with wavy walls with periodic structures featuring wells and hills. The periodic structure has wavelengths λ ranging from $27 - 80 \mu\text{m}$ and consists of smoothly connected circular arcs of radius R between $7 - 40 \mu\text{m}$, and thickness between $T = 20 - 28 \mu\text{m}$.

Grooves

In Chapter 5, we study colloids interacting with NLC confined in grooves. The grooves are made with standard lithographic methods of SU-8 2015, SU-8 2025 and SU-8 2050 epoxy resin (MicroChem Corp.) on glass coverslips. Different photoresists are selected depending upon the film thickness to be used in making the structures. Omni-coat is used to make sure the feature sticks to the glass. The features are soft baked (65°C for 1 hour, 95°C for 4 hours, 65°C for 1 hour) and exposed with a 70% filter at $150 \text{ mJ}/\text{cm}^2$, then hard baked at 65°C for 1 hour, then at 95°C for 2 hours. The grooves have height $h \approx 10, 20, 50 \mu\text{m}$,

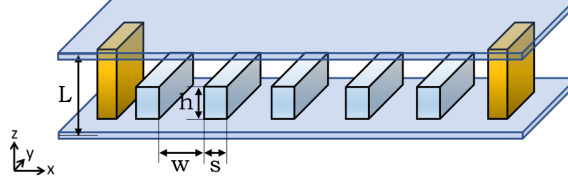


Figure 2.2: Groove cell. L denotes thickness of the cell. s denotes width of the groove, w denotes separation between the grooves and h denotes height of the groove.

width $s = 200 \mu\text{m}$, and separation $w = 15, 30, 50, 75, 100, 150 \mu\text{m}$ (Fig. 2.2).

2.1.2. Surface functionalization

Homeotropic anchoring

When adjacent to a surface with homeotropic anchoring, NLC molecules align perpendicular to the surface. Generally, surfactant molecules are chemisorbed to the surface with their hydrophobic tails exposed. At these surfaces, NLC molecules interdigitate with the surfactant tails to adopt this perpendicular configuration.

The surfactants that are commonly used for this purpose are the silane compounds dimethyl octadecyl[3-(trimethoxysilyl)propyl] (DMOAP) or tri-chloro(octadecyl)silane (OTS). Furthermore, they easily bond to silica or PDMS (polydimethylsiloxane) or most metal surfaces. However, they do not bind to the epoxy resins SU-8 or KMPR. Thus, structures made by photolithography must first be coated with either metal or silica for silanization to be effective.

To coat the surface with metal, the sample is pre-cleaned with plasma etching and placed in a custom sputtering chamber to coat a 30-nm film of chromium/nickel/silver/copper protected under argon gas.

To coat the surface with silica, the sample is pre-cleaned with plasma etching and placed in a desiccation chamber connected to a vacuum pump. The chamber must be wiped with acetone and pumped down to reduce humidity to minimize debris hitting the surface and

introducing imperfections. A drop of silica tetrachloride is pipetted from a syringe onto a glass coverslip placed adjacent to the sample. A vacuum is pulled for 7 minutes to carry out the chemical vapor deposition.

Silanization is carried out by immersing the silica surface or silica or metal coated structure in a 3wt% DMOAP solution for 10 minutes. The structure is rinsed with deionized (DI) and cured on a hot plate at 80 °C for 1 hour.

Planar anchoring

Untreated SU-8 and glass surfaces have degenerate planar anchoring in contact with NLC. However, in order to obtain strong or oriented planar anchoring, a polymer commanding layer must be coated onto these surfaces. In general, a long chain polymer is coated for strong anchoring and rubbed in one direction. The rubbing lays down microgrooves to dictate uniform anchoring of the NLC molecules at the surface.

There are several different polymer solutions that are used to make the command layer. These include a solution of 1wt% polyvinyl alcohol (PVA) in DI water, polyimide, a solution of 5vol% (3-Glycidyloxypropyl)trimethoxysilane (GLYMO) in DI water, or APTES (3-Aminopropyl)triethoxysilane). The glass slides or coverslips to be treated must be pre-cleaned with plasma etching. A PVA or a GLYMO film is spin-coated on glass at 2000 rpm for 20 seconds. A polyimide film is spin-coated at 4000 rpm for 40 seconds; longer spin coating is needed because of this solution's higher viscosity. The coated glass slides or cover slips are then cured at 80 °C for 1 hour. Note that a polyimide film appears opaque when first coated, but the opacity gradually disappear as the film is baked. To obtain oriented planar anchoring, the coated side is rubbed gently with a velvet cloth in the direction of least resistance, 7-10x in one direction. Finally, in one case, an APTES solution is also drop-casted on epoxy features and dried at 80 °C to induce extremely weak planar anchoring.

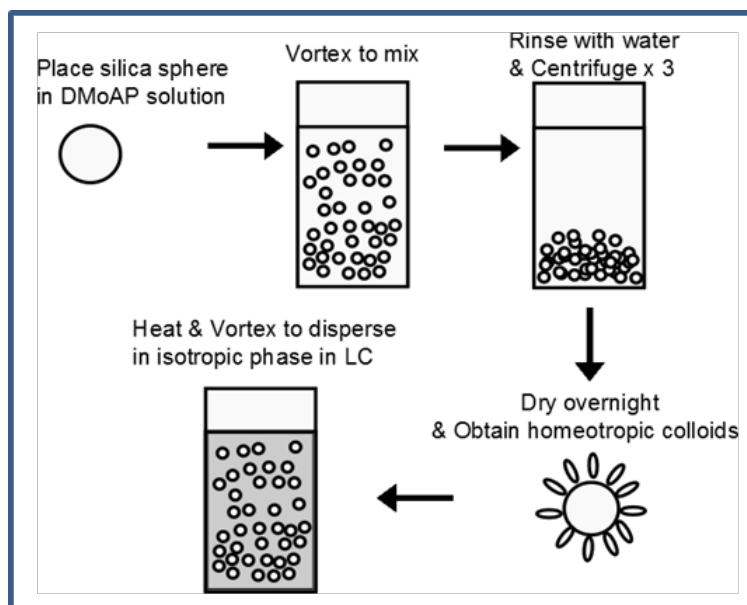


Figure 2.3: Colloid treatment with strong homeotropic anchoring condition.

2.1.3. Particle treatment and synthesis

Surface treatment of silica particles and ferromagnetic particles

In our study we typically use silica spherical particles ($a = 7.6 \pm 0.8 \mu\text{m}$, Corpuscular Inc. and radius $a = 5 \pm 0.5 \mu\text{m}$, Polysciences Inc.) and ferromagnetic spherical particles ($a = 4.3 \pm 0.4 \mu\text{m}$, Spherotech, Inc.) with polystyrene core and coated with chrome dioxide, treated with DMOAP to have homeotropic anchoring. The particles are first washed 3x with DI water, centrifuging at 1960 rpm for 5 minutes each time. They are then placed in a solution of 3wt% DMOAP, vortexed to mix for 30 min, and subsequently placed in oven at $80 \text{ }^\circ\text{C}$ for 1 hour to react. Once removed from the oven, they are washed again for 3x with DI water and dried overnight under vacuum at $80 \text{ }^\circ\text{C}$ (Fig. 2.3).

Occasionally, certain small molecules have strong affinity for the surface of silica particles, *e.g.* lipid dye (BODIPY-C5, 4,4-Difluoro-5,7-Dimethyl-4-Bora-3a,4a-Diaza-s-Indacene-3-Pentanoic Acid, Life Technologies Corporation). In these cases, it becomes necessary to attach an even longer chain to the particles so the dye does not absorb as strongly. Another

possible candidate to impose homeotropic anchoring is OTS. The covalent bond must form in the absence of water. Cleaned particles are first dried thoroughly in the oven overnight. Then they are placed in a solution of 1 vol% OTS in toluene, and vortex for 30 minutes in a sealed vial. The particles are then rinsed 3x with toluene (1960 rpm, 5 minutes each) and heated in the oven at 80 °C over nitrogen protection for 1 hour to evaporate additional solvent.

To impose strong planar anchoring, silica particles are placed in 1wt% PVA solution, vortexed to mix for 30 min, placed in oven at 80 °C for 1 hour, rinsed for 3x with DI water and dried overnight under vacuum at 80 °C.

Ferromagnetic droplets

In Chapter 4, we used custom-made emulsion droplets ($a = 4.3 - 8 \mu\text{m}$) consisting of a water phase that is loaded with magnetic nanoparticles and subsequently crosslinked suspended in an external oil phase. The oil phase consisted of 5CB mixed with 2wt% Span 80. The water phase was a 50:50 mixture of water loaded with iron oxide nanoparticles and a pre-mixed crosslinking mixture. The magnetic nanopowder iron (II, III) oxide (50-100 nm) was first treated with citric acid to make it hydrophilic [55]. The crosslinking mixture is pre-mixed with HEMA (2-hydroxyl ethyl methacrylate): PEG-DA (poly(ethylene glycol) diacrylate): HMP (2-hydroxyl-2-methylpropiophenone) in 5:4:1 ratio. Water and oil phases are emulsified with a vortex mixer to reach desired colloid size range. The two are combined in a vial treated with OTS (trichloro(octadecyl)silane) to minimize wetting of the wall by the water phase during the crosslinking process. The emulsion is crosslinked by a handheld UV lamp (UVP, LLC) at $\lambda = 270 \text{ nm}$ at roughly power $P = 1 \text{ mW cm}^{-2}$ for 3 hours. The emulsion is stored in a refrigerator for stability. Span 80 ensures that the liquid crystal-water interface would have homeotropic anchoring (Fig. 2.4a). The size and polydispersity of the colloids are characterized by measuring a number of colloids using the program FIJI.

Ellipsoids

The interaction of ellipsoidal particles with wavy walls is discussed in Chapter 6. The ellipsoidal particles are fabricated by a controlled stretching procedure from spherical polystyrene (PS) particles [36]. The PS particles ($2a = 10 \mu\text{m}$ and $2a = 25 \mu\text{m}$) are embedded in a polymer matrix by dispersing two drops of stock solution in 20 mL of a 5wt% PVA solution (average Mw 85,000-124,000, 87-89% hydrolyzed), and swirled to mix. The solution is placed in a Petri dish to dry over the course of two weeks. The dried film is then cut into strips and clamped down on both sides. The strip is stretched to twice its original length continuously while being heated with a heat gun ($\sim 500 \text{ }^\circ\text{C}$) to stretch the PS particles along with the PVA matrix (Fig. 2.4b). The stretched films are then dissolved in a 80:20 DI water to isopropanol solution sonicate to dissolve. Finally, the particles are washed 3x with DI water (1960 rpm, 5 minutes).

To functionalize the surfaces of these particles to impose anchoring, it is necessary to first coat them with silica or metal. Chemical vapor deposition or sputtering leads to contact line pinning and therefore solution processing is preferable. The following procedure has been adopted from [39]. The stretched PS particles are dispersed in DI water ($\sim 1\text{wt}\%$), 8.28 mL of the solution is combined with 61.1 mL ethanol, and 10.1 mL ammonia in a bottle, and the content is constantly stirred. A 5 wt% solution of TEOS (tetraethyl silicate) is slowly added at the rate of 1 mL every 25 minutes. A total of 5 mL of solution is added. The particle is recovered and washed by centrifuging (1790 rpm, 3x). Once the particle is coated with silica, it is treated with DMOAP as previously stated to give homeotropic anchoring.

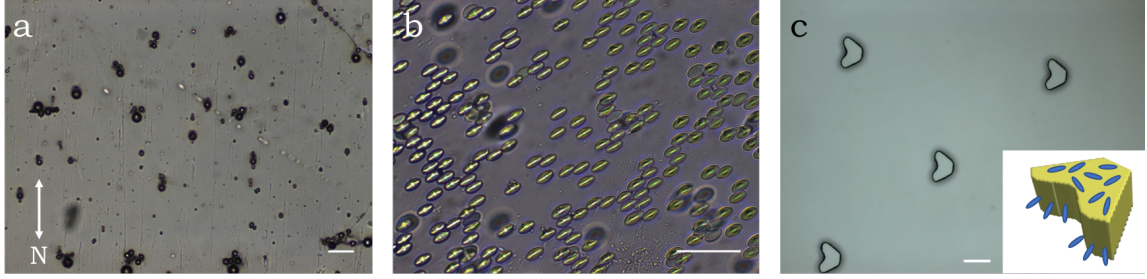


Figure 2.4: Synthesized particles. (a) Ferromagnetic droplet in NLC. Hedgehog defects are clearly visible. (b) Stretch polystyrene particles of aspect ratio 2 embedded in PVA matrix. (c) Anisotropic platelet made with SU8. Inset: schematic that shows the anchoring condition on the particle. The scale bars are $50 \mu\text{m}$.

2.1.4. Cell fabrication and sample preparation

Assembly of the vessel containing the wavy wall

The wavy strips made by photolithography (Fig. 2.1a) are treated to have homeotropic anchoring (Fig. 2.1b). Thereafter, the wall is carefully removed from the substrate with a razor blade to form a strip (Fig. 2.1c): in this way we could obtain a floating strip in which three sides, including the “wavy” one, has homeotropic anchoring, and one (the one that was previously in contact with the glass) retains the native degenerate planar anchoring from SU-8. Two glass cover slips are prepared with uniform planar anchoring. The treated strip is then carefully placed between the cover slips to form a planar cell “sandwiching” a wavy wall (Fig. 2.1d). Mylar spacers (either single $25 \mu\text{m}$ or multiple $6 \mu\text{m}$ spacers) are placed between the cover slips to give thickness that matches the thickness of the strips. The cover slips are aligned in anti-parallel fashion to minimize splay due to pre-tilt angle in the cell, which destabilizes Saturn rings even under confinement and creates a bias in the direction of the dipoles. Once assembled, the long axis of the wall is perpendicular to the oriented planar anchoring on the bounding surfaces. We secure the cover slips with binder clips first, then bind them with optical glue and remove the binder clip. We observe that in some LC cells the actual thickness is larger than expected, which is attributed to a gap above the strip. In those cases we noticed that some small colloids can remain trapped

between the wavy strip and the top glass surface, so the effective thickness can be as large as $35 - 40 \mu\text{m}$. In this way, the sides of the strips in contact with the LCs are the straight homeotropic wall and the wavy homeotropic wall.

Assembly of groove structures into a confining vessel

The groove are treated to have homeotropic anchoring, and capped with a homeotropic coverslip. The total thickness of the cell was controlled by a Mylar spacer to locate the lid $10-20 \mu\text{m}$ above the grooves. For some experiments, we added additional features to the top glass to guide the assembly: an SU-8 square pillar array (height $h = 5 \mu\text{m}$, sides $s = 5 \mu\text{m}$, pitch $p = 50 \mu\text{m}$) to the top coverslip. The substrate with pillars and the top cover slip are both treated to have homeotropic anchoring (Fig. 2.2).

Filling a closed NLC cell

We use the nematic liquid crystal 5CB (4-cyano-4'-pentylbiphenyl, Kingston Chemicals) as purchased. Typically, a stock solution is made inside the hood (while wearing N95 masks). The stock solution is diluted based on needs. All closed cells are filled by capillarity with a suspension of colloids in the isotropic phase, and subsequently quenched into the nematic phase ($T_{NI} = 34.9^\circ\text{C}$).

Preparation of lipid-dye solution

In Chapter 4, the adsorption of lipid-dye molecules into Saturn ring defects for colloids near the wavy wall is discussed. In Refs. [111, 112], BODIPY-C5 (4,4-Difluoro-5,7-Dimethyl-4-Bora-3a,4a-Diaza-s-Indacene-3-Pentanoic Acid, Life Technologies Corporation) is shown to self-assemble inside the defect at concentrations above $59 \mu\text{M}$, but only by dimerizing. It is noteworthy that monomeric and dimeric BODIPY-C5 have different optical spectra: $\lambda^{ex} = 456-502 \text{ nm}$ and $\lambda^{em} = 510-562 \text{ nm}$ for monomers, and $\lambda^{ex} = 533-584 \text{ nm}$ and $\lambda^{em} = 606-684 \text{ nm}$ for dimers. Thus, the assembled structure can only be imaged by the latter

set of conditions. In order for us to visualize assembled structure inside the defect, we must either add longer chains to the BODIPY dye, *e.g.* BODIPY-C12, or dye another lipid which can partition into the defect with BODIPY-C5. The dyed lipids are imaged with monomeric λ^{ex} and λ^{em} .

One choice is DLPC (1,2-dilauroyl-sn-glycero-3-phosphocholine, Avanti Polar Lipids, Inc.), which is doped with 3 mol % BODIPY-C5. To make a solution with DLPC, a 0.1 g/mL solution is prepared (average Mw = 621.826), or 160.8 mM. It is diluted 100x to make a solution of 1608 μM in chloroform. BODIPY-C5 comes dispersed in methanol in solution form, at around 2000 μM in concentration. BODIPY-C5 is first added to the DLPC solution at 3 mol %. The lipids are swirl to mix. Typically, we make a 100 μL solution of 5CB. The BODIPY-C5-diyne mixture is added to the 5CB with a Hamilton syringe. The solution is well-mixed and placed in oven for 3 hours to evaporate solvents under the vacuum. The particles are introduced to the 5CB right before the experiment to prevent dye absorption onto the surface of the colloids.

Following the procedures in Refs. [111, 112], for crosslinkable lipids, we make a 20 μM lipid solution with 2 mol% BODIPY-C5 dye or 0.4 μM . Diyne PC (1,2-bis(10,12-tricosadiynoyl)-sn-glycero-3-phosphocholine, Avanti Polar Lipids, Inc.) comes in dry powder form (Average Mw = 914.3). It is first dispersed in chloroform to make a stock solution of 0.1 g/mL, which converts to 109.3 mM. The stock solution is diluted 100x to make a solution of 1093 μM in chloroform with a Hamilton syringe. Similar procedure as the DLPC above is used to mix the diyne and BODIPY-C5 into 5CB.

2.1.5. Imaging

Birefringence of liquid crystals

Birefringence means that the index of refraction of the material depends on the polarization of light, in liquid crystal, this quantity is defined as the difference of $\Delta n = n_1 - n_2$, where n_1 and n_2 are the indices of refraction in the direction parallel (extraordinary index of

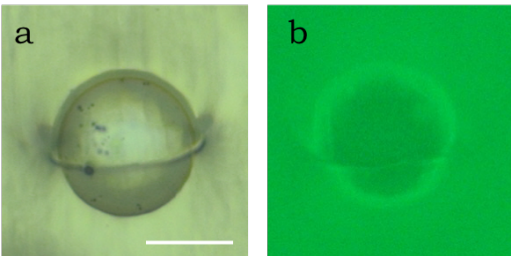


Figure 2.5: Lipids partition into defects. Stronger signals from the defects are detected under fluorescent microscopy. The LC phase contains $20 \mu M$ diyne, $0.4 \mu N$ BODIPY. The scale bar is $50 \mu m$.

refraction) and perpendicular (ordinary index of refraction) to the local director field (optical axis). These values are temperature dependent, and birefringence decreases with increasing temperature. Liquid crystals are commonly observed between crossed polarization to infer the director field from the light and dark textures. When an isotropic liquid is placed between crossed polarizers, light first crosses the polarizer, as it travels through the isotropic medium, it remains polarized in the same way. Thus, when it travels to the analyzer, which has perpendicular polarization, all light is blocked. However, when liquid crystal is placed between crossed polarizers, light travels at different rates in these two directions. Light traveling along the optical axis travels with a refractive index n_2 , while light traveling perpendicular to it travels with an effective index of refraction n_{eff} :

$$n_{\text{eff}} = \sqrt{\frac{n_1^2 n_2^2}{n_1^2 \cos^2 \theta + n_2^2 \sin^2 \theta}} \quad (2.1)$$

where θ is the angle between the light propagation direction and the local director field. The light is polarized again by the LC. The dark region denotes locations where the director field is parallel to either the polarizer or analyzer. Liquid crystal confined between two glass cover slips with degenerate planar anchoring forms the famous Schlieren texture (Fig. 2.6). The dark brushes meet where defects are located. Four brushes denote a ± 1 defect, and two brushes denote a $\pm \frac{1}{2}$ defect. The sign of the defect can be further elucidated by rotation of the sample. Throughout this thesis, we use polarized microscopy to verify the anchoring

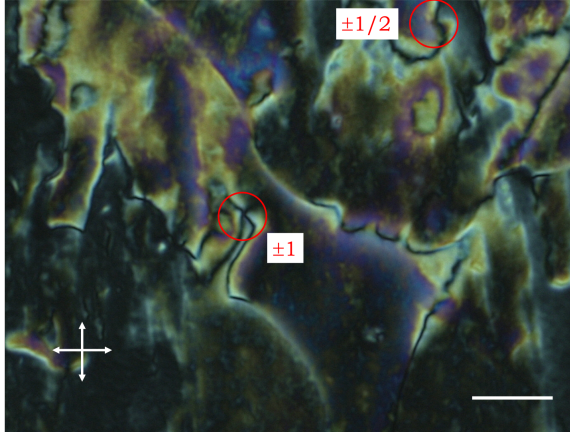


Figure 2.6: Schlieren texture under crossed-polarizers. The red circles denote defects. The scale bar is $20 \mu\text{m}$.

on our bounding surfaces.

Bright field and cross-polarizing microscopy

The channels were imaged by an upright microscope (Zeiss AxioImager M1m) in the transmission mode equipped with crossed polarizers. The images were captured by a high-resolution camera (Zeiss AxioCam HRc). Objective magnification ranged from 20x to 100x.

Fluorescent confocal polarizing microscopy (FCPM)

In Chapter 5, to determine the director field orientation, fluorescence confocal polarizing microscopy (FCPM) was performed, following the method in Ref. [101], with an inverted IX81 Olympus microscope equipped with a half-wave plate between the objective and filter cubes, which serves to change the polarization of the scanning laser. While FCPM is useful to characterize LC director fields in many settings, in this particular case one has to take into account optical aberrations that can neither be ignored nor avoided.

Scanning Electron Microscopy (SEM)

SEM images are acquired with a Quanta 600 FEG Mark II microscope equipped with a low voltage detector for environmental SEM (Singh Nanoscale Characterization Facility at the University of Pennsylvania). We used 10 kV voltage and about 1 Torr of chamber pressure, and the samples are not coated with any metal layer.

2.1.6. Applying a magnetic field

In Chapter 4, we use a permanent magnet to control the initial position of a ferromagnetic particle or droplet to probe their behavior in a distorted elastic field. The magnetic field was applied by using a series of 8 NdFeB magnets (K&J Magnetics, Inc.) attached to the end of a stick. The magnets was placed roughly 0.5 cm from the sample; the field applied is estimated to be roughly 40-60 mT, far below the strength required to reorient the NLC molecules, but sufficiently strong to overcome the drag and move magnetic droplets and particles in arbitrary directions.

For controlled rotation, two pairs of orthogonal coils are used. Two types of coils are used here: (1) inner Diameter of 0.5 in., outer diameter of 0.87 in., coil turns of 260, and field Intensity of 1.2 mT in the middle; (2) Inner diameter of 1.47 in., outer diameter of 2.375 in., coil turns of 160 and field intensity of 1.6 mT in the middle. The systems are adopted from Ref. [41].

2.2. Simulations

2.2.1. Landau deGennes (LdG) simulations

Model overview

The basis of the simulation (Q-tensor theory) has been outlined in detail in Chapter 1, Section 1.2.2. To simulate the director field of NLC in scaled down models of our geometry, the total energy of the system is minimized with a finite difference scheme on a regular

cubic mesh. Defects are defined as the regions where the order parameter S is significantly less than the bulk value.

We can incorporate different levels of complexity: unequal elastic constants, varying elastic constants, importing custom geometry, and applying an electromagnetic field. These topics are discussed in detail in [3]. The variation of S introduces a characteristic length, the correlation length ξ_N , which can be obtained by assuming one-constant and uniaxial \mathbf{Q} . The phase free energy density Eq. 1.29 can be written as:

$$f_{phase} = \frac{3}{4}AS^2 + \frac{1}{4}BS^3 + \frac{9}{16}CS^4 \quad (2.2)$$

The distortion free energy density Eq. 1.30 can be reduced to:

$$f_d = \frac{L}{2}(\nabla\mathbf{Q})^2 = \frac{L}{2}(\nabla S)^2 \quad (2.3)$$

The free energy density of LdG can be written as [89]:

$$f_{LdG} = \frac{3}{4}AS^2 + \frac{1}{4}BS^3 + \frac{9}{16}CS^4 + \frac{3}{4}L(\nabla S)^2 \quad (2.4)$$

By minimizing energy with Euler-Lagrange (EL) assuming variation in S only. we obtain:

$$\frac{3}{2}L\nabla^2 S - \frac{\partial f_{LdG}}{\partial S} = 0 \quad (2.5)$$

Linearize for small Δs with respect to the equilibrium position S_0 :

$$S(\mathbf{x}) = S_0 + \Delta S(\mathbf{x}) \quad (2.6)$$

to obtain the correlation length:

$$\begin{aligned}\xi_N &= \sqrt{\frac{3}{2} \frac{L}{\partial^2 f_{LdG}/\partial S^2|_{S_0}}} \\ &= \sqrt{\frac{L}{A + BS_0 + \frac{9}{2}CS_0}}\end{aligned}\tag{2.7}$$

The correlation length roughly determined the size of the defect and the mesh size of the simulation ($\Delta x = 4.5$ nm), which does not scale with system size. As a result, it introduces complexity in modeling micron-sized particles. Due to the difference in scale, the exact final configurations of numerics and experiment must be compared with caution. Nevertheless, it is an invaluable tool to corroborate and elucidate experimental findings. The numerics and minimization model were written by Daniel A. Beller [3]. Our contributions in expanding and applying the code to specific experimental systems, are explained below.

Mapping the energy landscape near a wavy wall and calculating trajectories

In Chapter 4, Q-tensor simulations are used to find minimum energy configurations. The geometry of the system, the boundary conditions, and elastic constants for the NLC are inputs to the numerical relaxation procedure. The one-constant approximation is used. Since we have a quasi-2D system, with the director field expected to lie in the plane of the wavy wall, the effect of changing the twist constant is expected to be weak in comparison to changing the splay and bend elastic constants. Specifically, the particle is bounded by walls with oriented planar anchoring separated by thickness $T = 4a$, unless otherwise specified. The anchoring at the boundary opposite of the wavy wall is set to zero, and that of the flat plates sandwiching the colloid and the wavy wall is set to oriented planar. The Nobili-Durand anchoring potential is used [75]. Because the size of simulation is much smaller than the experimental system, much stronger anchoring is applied. For most of our results, infinite anchoring strength is applied unless otherwise specified.

In order to gain insight into the energy landscape of a colloid near the wall, numerical mod-

eling was performed for a colloid located at different locations between two identical wells. The colloid center of mass (COM) was first placed at a fixed location. The corresponding energy field for the NLC was found. The colloid location was then moved to a new location on a grid. The spacing between COM locations was set to 2.5 times the simulation mesh size, corresponding to 11 nm. The rest of the simulation parameters are as follows, with lengths given in multiples of the simulation mesh size: colloid radius $a = 12$, which corresponds to 54 nm; wavelength of the well $\lambda = 60$, which corresponds to 270 nm; amplitude $A = 6$, which corresponds to 27 nm, with well curvature radius R of roughly 22, corresponding to 98 nm. Thus, $\lambda/a = 5$ and $R/a = 8$ and adjacent grid points are separated by $\sim 0.2a$. The colloid surface imposes homeotropic anchoring of infinite strength.

To calculate the liquid crystal free energy, the colloid is centered at a specified location on the grid and the Landau-de Gennes free energy is minimized numerically over the entire Q-tensor field. The output from two representative colloid locations are shown in Fig. 2.7a, b. The discretized liquid crystal free energies as a function of colloid center position (denoted by black dots) is expressed in the heat map shown in Fig. 2.7 c, by choosing the energy of the system when a colloid is located at $(x, y) = (\lambda/2, \lambda)$ as reference, and performing the conversion from simulation units to real units ($1 \text{ s.u.} = 3.7 k_B T$). Assuming symmetry and periodicity, we can fit a smooth function $g(x, y)$ over the entire space. The fitting of $g(x, y)$ requires trial and error, with the goal of finding the simplest model that capture the variation of the field without over fitting. A sample fit model is detailed in Appendix B. As the energy landscape becomes even more complex, interpolation should be explored. However, interpolation is also expected to introduce additional complexity in dealing with taking the gradient. By taking the gradient of this energy field $g(x, y)$, we obtain the direction of the elastic force field experienced by the particle. This elastic force includes the distortion and defect sourced by a colloid in the domain. Hills are repulsive, and wells are attractive in the case of a colloid with homeotropic anchoring in a Saturn ring configuration (Fig. 2.7d).

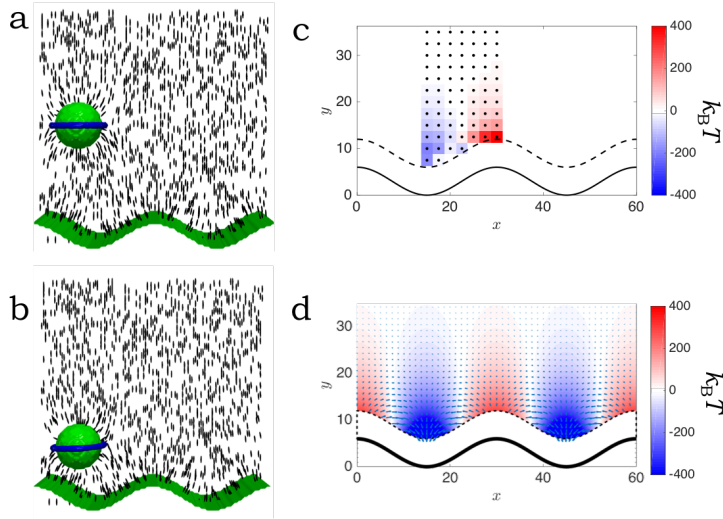


Figure 2.7: Mapping the energy landscape by sampling and calculating particle trajectories by force field. (a, b) Sample LdG numerical modeling results with a colloid centered at two different grid locations above a wavy wall. (c) Discretized form of energy by choosing the site above the center of the well ($\lambda/2, \lambda$) as the reference energy. (d) Smoothed energy field extended by assuming symmetry and periodicity.

Finally, we simulate trajectories of a colloid released at different locations near the wavy wall. Consider a colloid is placed at an initial position (x_0, y_0) . The force balance on the colloid is simplified in the limits explored in experiment: given the low Reynolds number applicable to the colloid's motion, acceleration is negligible; furthermore, since the colloids move in a deterministic manner, Brownian motion is also negligible. Thus, the colloid moves quasi-statically along a path determined by the elastic force, which is balanced by viscous drag on the particle. We are interested here in the particle path, which is determined by the elastic force. The direction and magnitude of the elastic force at the initial location is calculated by the gradient of the field $g(x, y)$ at that point, as described above. Colloidal paths are simulated by updating the particle position by a step path length Δs , according to explicit Euler scheme:

$$\begin{cases} x_{i+1} = x_i - \frac{\partial g}{\partial x}|_{x_i, y_i} \Delta s \\ y_{i+1} = y_i - \frac{\partial g}{\partial y}|_{x_i, y_i} \Delta s \end{cases} \quad (2.8)$$

Trajectories starting from arbitrary locations can thereby be calculated, in qualitative agree-

ment with experimental trajectories. We show that the trajectories are very sensitive to initial locations. This method does not take into account hydrodynamic interactions with the wall or Brownian motion.

Modification to model dipoles

Based on Eq. 1.29, to increase the defect core energy, we replace the ratios of the material constants $B/A \approx 12.33$, $C/A \approx -10.06$, commonly used to model 5CB [89], with $B/A = 106$, $C/A = -86.5$. With $A < 0$ held fixed, this replacement increases the minimum absolute value of f_{phase} by a factor of 2.6, which sets the defect core energy density.

In addition, we also initialized the system with a dipole-like director field around the colloids before relaxation: $\mathbf{n}(\mathbf{r}) = \hat{i} + PR_c^2 \frac{\mathbf{r}-\mathbf{r}_c}{|\mathbf{r}-\mathbf{r}_c|^3}$, where R_c is the colloid radius, \mathbf{r}_c is the location of the colloid center, $P = 3.08$ is the dipole moment, and \hat{i} is the far-field director [103]. This expression is applied only in a sphere of radius $2R_c$ around \mathbf{r}_c . With this implementation, we are able to stabilize dipole at colloid diameter $D = 180$ nm as opposed to the $D = 720$ nm theoretical value in simulation [103]. In comparing the energy of the Saturn ring and the dipole, we must keep in mind that the Saturn ring is more stable for very small colloids, while the dipolar configuration is stable for larger colloids. Thus, the Saturn ring always has the lower energy in the numerics, while the opposite is true in experiment. A scaling argument for a very specific case of colloids near wall is discussed in detail in Chapter 4.

Introducing the wavy wall

The original LdG code does not contain wavy boundary, however, it is easy to add user-defined boundaries from input. The file is put into the command line as `-b inputfilelabel`. In this file, which we have written through MATLAB, we specify the number of total object, followed by a list of object identifier, anchoring type and anchoring strength. This is followed by a object position (x, y, z) as well as outward normal (ν_x, ν_y, ν_z) . All points that belong to the boundary must be specified, not only those on the surface, but also those in the

interior. The interior points has their normal vector specified as place holder, and are not factored into the energy calculation.

Here is an example run for goldilocks on a 160x48x100 grid: with a colloid COM located at (pos1, pos2) which goes through the numbers in the lists (seq 70 5 150) and (seq 25 5 70), with a radius of 12.

```
for pos1 in $(seq 70 5 150); do echo $pos1; for pos2 in $(seq 25 5 70); do
  echo $pos2; ./nematic.out -f GL_$pos1\__$pos2 -b diffperiod_2x.dat -Lx
  160 -Ly 48 -Lz 100 -outputskiprods 4 -numcolloids 1 -Wcolloidtype 0 -
  colloidradius 12 -Cx $pos1 -Cz $pos2 -XPBC 1 -YPBC 0 -Wxytype 2 -ZPBC 0
  -Wtoptype 0 -inittype 1 -quitQstep 1e-4; done; done
```

The output file name is called GL_\$pos1__\$pos2. -outputskiprods is set to 4 so director field is only saved on a coarser grid to reduce output file size. The boundary conditions are set so the colloid has homeotropic anchoring, the top and bottom glass slides has uniform planar anchoring (they are not shown in Paraview in order to minimally obstruct view of the director field).

It must be noted that in the geometry we are trying to simulate, -XPBC is set to be 1 (true), the wavy wall must have the same size as the box size. Otherwise, LC will penetrate the wall and introduces error in energy calculation. The MATLAB file used to write the geometry of the boundary file can be found in Appendix.

Modeling director field inside grooves

In Chapter 5, the director field is simulated for NLC confined in grooves with homeotropic anchoring. For this system, the simulation is 222 times smaller than the experimental settings. All corners are rounded with a circular arc of radius 9 nm. In the simulations with colloids, the colloids have diameters of $d = 22.5$ nm. The anchoring strength on the surface of the colloids is set to be the same as the wall and equal to 5.82 in the simulation

unit, corresponding to a typical anchoring strength of $W_0 = 1 \times 10^{-2} J/m^2$. In simulations without colloids, the wall has infinite anchoring strength. Each simulation is carried out in a thin slice in \hat{y} of thickness = 22.5 nm. The simulation box has the same depth as the colloid diameter (22.5 nm), but is several times larger in length (225 nm) and width (450 nm). With periodic boundary conditions along the y -direction (depth), the simulation is quasi-2D. We have verified that the director field in the simulation does not vary in \hat{y} -direction.

2.2.2. COMSOL simulation

Comsol simulations were performed to simulate the director field absent defects in the limit of small distortions. Since the individual components of the director field are governed by the Laplacian as detailed in Chapter 1, Eq: 1.19, they can be solved by COMSOL separately in x - and z - directions, whereas the y - direction depends on x and y : $n_y = \sqrt{1 - n_x^2 - n_z^2}$. In COMSOL, this is easiest if implemented by the Electrostatics Module. The model solves the electrostatic equivalence of

$$\nabla^2 V = 0 \tag{2.9}$$

Within a defined two-dimensional space, V is a scalar and is the same as one component of our field n_x or n_z in our study. We assume zero charge to maintain the validity of Eq. 2.9. We use this system to guide our thinking for nematic liquid crystal placed near a wavy wall. The following boundary conditions are imposed: (1) Periodic boundary conditions are enforced in x -direction; (2) Uniform planar anchoring ($n_x|_{\text{glass}} = 0, n_y|_{\text{glass}} = 0$) is enforced on the z -direction; (3) Perpendicular anchoring ($n_x|_{\text{wavy wall}} = \frac{F'(x)}{\sqrt{(1+F'(x))^2}}, n_z|_{\text{wavy wall}} = 0$) is enforced on the wavy wall where $y = F(x)$ defines the shape of the wavy wall. At the boundary opposite the wavy wall at the top of the simulation cell, a free boundary condition is applied. In the single constant approximation, these boundary conditions require that n_z everywhere. In a system with no colloids, the distortion is determined by variation of n_x alone.

We mesh the space with a triangular mesh (Fig.2.8a) and calculate x - and y - components separately (Fig. 2.8b,c), then output the results in grid form and reconstruct the vector in MATLAB. Specifically, we calculate the splay and bend distortion by Eqs. 2.10 and 2.11, then combined the two components in MATLAB:

$$S = \frac{1}{2}K(\nabla \cdot \mathbf{n})^2 = \frac{1}{2}K \left(\frac{\partial n_x}{\partial x} + \frac{\partial n_z}{\partial z} \right)^2 \quad (2.10)$$

$$\begin{aligned} B &= \frac{1}{2}K(\mathbf{n} \times \nabla \times \mathbf{n})^2 = K \left(\frac{\partial n_x}{\partial x} + \frac{\partial n_z}{\partial z} \right)^2 \\ &= \frac{1}{2}K \left\{ \mathbf{n} \times \left[\left(\frac{\partial n_z}{\partial y} - \frac{\partial n_y}{\partial z} \right) \hat{i} + \left(\frac{\partial n_x}{\partial z} - \frac{\partial n_z}{\partial x} \right) \hat{j} + \left(\frac{\partial n_y}{\partial x} - \frac{\partial n_x}{\partial y} \right) \hat{k} \right] \right\}^2 \\ &= \frac{1}{2}K \left[\mathbf{n} \times \left(\frac{\partial n_x}{\partial z} - \frac{\partial n_z}{\partial x} \right) \hat{j} \right]^2 \\ &= \frac{1}{2}K \left[n_x \left(\frac{\partial n_x}{\partial z} - \frac{\partial n_z}{\partial x} \right) \hat{k} - n_z \left(\frac{\partial n_x}{\partial z} - \frac{\partial n_z}{\partial x} \right) \hat{i} \right]^2 \\ &= \frac{1}{2}K \left(\frac{\partial n_x}{\partial z} - \frac{\partial n_z}{\partial x} \right)^2 \end{aligned} \quad (2.11)$$

A sample director field, bend and splay energy density plot is calculated for surface with shape $h(x) = A(1 + \cos(kx))$ where $A = 2.5$ and $k = \frac{2\pi}{\lambda}$ where $\lambda = 30$, and the heat map output is shown as the following (Fig. 2.8d-f):

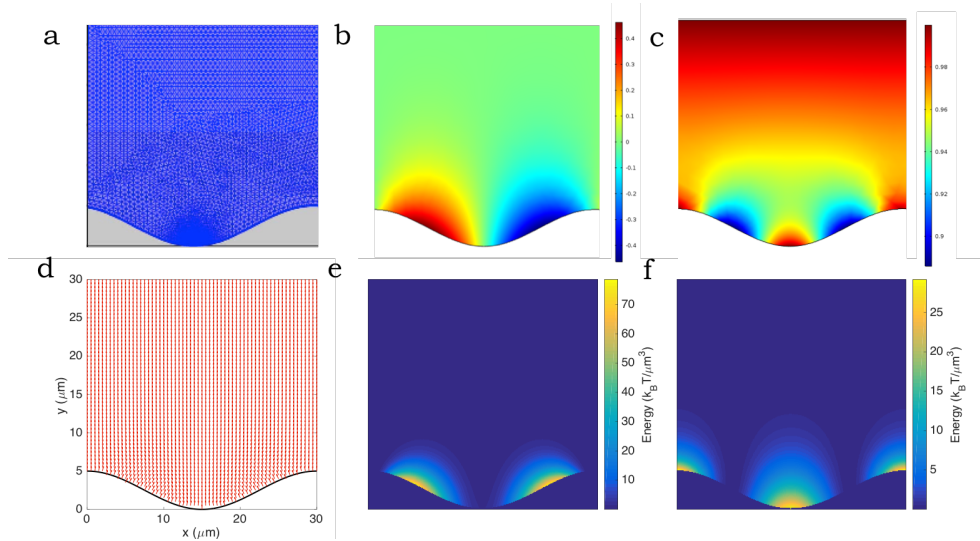


Figure 2.8: COMSOL outputs. (a) The mesh. (b) x -component of the director field n_x . (c) y -component of the director field n_y . (d) The director field. (e) Bend deformation. (f) Splay deformation.

Chapter 3

Lock-and-key interaction in nematic liquid crystals

Reproduced from Ref. [68] with permission from the Royal Society of Chemistry.

3.1. Background: Lock-and-key interaction

The concept of a “lock-and-key” interaction is inspired by biology. In biological systems, a substrate perfectly fits into the cavity of an enzyme, thus promoting catalytic reactions [26]. This mode of interaction has been exploited in colloidal science [69, 90], where particles of complementary shapes come together through depletion interactions that are on the order of thermal energies in an isotropic fluid. Additional studies show that when the particle is anisotropic, such as the case of an ellipsoidal particle, rotational degrees of freedom play important roles in determining the fate of whether the key docks in the lock [49].

A particle in a LC can also feel the attraction from a cavity of complementary shape, mediated by elastic interactions that far exceed thermal energies. This interaction was proposed by Telo de Gama and coworkers [97]. Two-dimensional (2D) simulation predicted that a homeotropic disk in a NLC minimizes its energy by nestling into a well with homeotropic anchoring and the same radius of curvature. In NLC, the boundary does not only serves as a complementary docking site, but also dictates the energy field in the vicinity. Full three-dimensional studies confirmed the initial concept [23], and suggested a mechanism of sorting the particles between topographical peaks and wells, or, as Maxwell would call them, “hills and dales”, based on the anchoring of the particles. The simple rule is that

particles migrate to the dales if the anchoring of the particle and the substrate coincide (*i.e.* both homeotropic or both planar) and to the hills if the anchoring is different for particle and substrate. This phenomenon was shown also in the experimental work by Silvestre *et al.* [96] that showed how a planar particle is preferentially found at the tip of a homeotropic micro-pyramid, while a homeotropic particle is found at the base of the same pyramid [40]. In the three-dimensional simulations, the homeotropic particles always have associated Saturn ring defects. In this work, we explore behaviors of both the dipoles and Saturn rings. This work also highlights the importance of the geometry of the cavity.

The original studies suggested that the interaction between the “lock”, a well in the shape of a semi-circle in an otherwise planar wall, and the “key”, a colloid with a Saturn ring defect, occurred via the “defect sharing” mechanism. A defect, located where the planar wall connects to the semicircle is merged with the defect on the particle [96]. Later, another computational 3D study suggested an additional mechanism: “splay matching” [40], where the interstitial space between the particle and the cavity is filled with uniformly aligned NLCs, due to homeotropic anchoring on both the lock and the key. Both studies point to that topographical features can be used to localize colloids.

3.2. Defect-free system as a system for colloidal assembly

Here we present an experimental system that confirms the lock-and-key mechanism for Saturn ring particles and also allows us to interrogate the behavior of the elastic dipoles. To demonstrate the lock-and-key mechanism, we designed an experimental system (i) to have a 2D-like geometry as in the original simulation, (ii) to control independently the anchoring at the wall and at the particles, (iii) to allow for clear visualization of the process of particle moving towards topographical features and finding its preferred location, (iv) to investigate particles with Saturn rings but also particles with an associated point defect, and (v) to potentially allow for the exploration of many parameters and anchoring configurations. The experimental setup, the sandwich cell, is described in Chapter 2 (Fig. 3.1a). Typically, we observe the sample from a bird’s-eye-view (Fig. 3.1b).

The mismatched anchoring condition between the colloids (homeotropic) and the top and bottom cover slips (planar) causes the colloids to be repelled away from both (Fig. 3.1a). Elastic energy $E_{el} = Ka$ and potential energy $E_g = \frac{4}{3}\pi a^3(\rho_p - \rho)g\frac{T}{2}$, where T denotes thickness of the cell. Given $a = 7.5 \mu m$, $K = 10^{-11} N$, $T = 20 - 28 \mu m$, $g = 9.8 m/s^2$, and $\rho_p - \rho = 0.99 \times 10^3 kg/m^3$ for our system. Using these values to estimate the relevant energies, $E_{el} = 7.5 \times 10^{-17} J = 1.8 \times 10^4 k_B T$, and $E_g = 2.14 \times 10^{-16} J = 5.1 \times 10^4 k_B T$. So gravity and elastic force compete with each other to determine the equilibrium position of the particle. The equilibrium height of a homeotropic particle can be calculated by balancing the elastic repulsion and gravity. The interaction between a dipole and a flat wall is calculated by the pair interaction between the dipole and an image dipole reflected across the flat wall:

$$E_{dp} = 4\pi K \frac{p^2}{r^3} \quad (3.1)$$

where $p = Aa^2$, A is a numerical factor $A \approx 2.04$ [65], thus the force between two dipoles is

$$F_{dp} = \frac{3}{2}\pi K A^2 \left(\frac{2a}{r}\right)^4 \quad (3.2)$$

In a sandwich cell [84]:

$$\begin{aligned} \Sigma F &= F_{bottom} - F_{top} - F_g \\ &= \frac{3}{2}\pi K A^2 \left(\frac{2a}{T - 2\delta}\right)^4 - \frac{3}{2}\pi K A^2 \left(\frac{2a}{T + 2\delta}\right)^4 - \frac{4}{3}\pi a^3(\rho_p - \rho)g \\ &= 0 \end{aligned} \quad (3.3)$$

where F_{bottom} and F_{top} are the repulsion between the dipole and its mirror image located at the bottom ($z = 0$) and the top ($z = T$), where δ is the deviation from the mid-plane ($z = \frac{T}{2}$) due to gravity.

Given the same material constants as above, we can calculate $\delta = 0.3 - 1.7 \mu m$ for dipoles.

For a pair of Saturn rings:

$$F_{qp} = 180\pi K \left(\frac{c^2}{r^6} \right) \quad (3.4)$$

where $c = -\beta a^3$ is the quadrupole moment, $\beta \approx 0.72$, and the balance in the case of Saturn ring is then:

$$\begin{aligned} \Sigma F &= F_{bottom} - F_{top} - F_g \\ &= 180\pi K \beta^2 \left(\frac{a}{T - 2\delta} \right)^6 - 180\pi K \beta^2 \left(\frac{a}{T + 2\delta} \right)^6 - \frac{4}{3}\pi a^3 (\rho_p - \rho)g \\ &= 0 \end{aligned} \quad (3.5)$$

Given the same material constants, we can calculate $\delta = 1.4 - 5.1 \mu m$ for quadrupole. So although the particle is not situated exactly at the mid-plane ($z = \frac{T}{2}$) between the top and bottom glass slide, they are very close to it due to the elastic repulsion. The dipole equilibrate much closer to mid-plane compare to Saturn ring, due to stronger repulsion from the glass cover slips.

The wavy wall forms a series of hills and wells, with amplitude $2A$ measured from the base of the well to the highest point on a hill. Because of strong homeotropic anchoring at the wavy wall, these features impose zones of splay and bend in this domain. In particular, the valleys are sites of converging splay, the hills are sites of diverging splay, and the inflection points are sites of maximum bend. The wavelength of the structure λ can be expressed in terms of the radius of curvature R and the amplitude A : $\lambda = 4R\sqrt{\frac{A}{R}(2 - \frac{A}{R})}$ (Fig. 3.1c). Therefore, λ and R are not independent for fixed A . Different aspects of the colloid-wall interaction are best described in terms of one or the other. For example, the range of the distortion is discussed in terms of λ , and the splay field near the well is described in terms of R . Throughout this study, unless specified otherwise, $2A = 10 \mu m$. The gentle undulations of this wall deform the surrounding director field but do not seed defect structures into the NLC. Deeper wells, such as those discussed later in this Chapter, are also characterized by their well depth Δ , and opening Ω .

As a result of their curvature, the gentle hills and dales of the walls become sites of splay distortion in the nematic director field \mathbf{n} . The distortion in the bulk decays smoothly away from the wall without introducing any topological defects. It is instructive to consider a Fourier mode of the function defining the wall shape:

$$h(x) = A\cos(kx) \tag{3.6}$$

Under the one-constant approximation and assuming small gradients in the director field. In this limit, \mathbf{n} can be expressed simply (Fig. 3.1d):

$$\begin{cases} n_x = A k \sin(kx) e^{-ky} \\ n_y = 1 \end{cases} \tag{3.7}$$

where n_x, n_y are components of the director.

This director field could be realized either near walls with shallow hills and dales, or, alternatively, in regions far enough from the wall that gradients in \mathbf{n} are weak. This form suggests hills and dales are sites with the highest splay energy density, while the inflection points are sites with highest bend energy density. The distortion created by a particle with homeotropic anchoring always induces a defect, either an elastic dipole or a Saturn ring [107].

The alignment of a colloid-free cell is examined under crossed polarizers (Fig. 3.1e, f), which shows that the bulk liquid crystal is defect-free. The much brighter texture at 45°-135° (Fig. 3.1e) compared to the 0°-90° (Fig. 3.1f) also shows good planar alignment along the y -direction. The defects visible in Fig. 3.1e,f are only in the thin NLC film squeezed between the top of the wavy wall and the confining glass, a region which is not accessible to the colloids.

To investigate the lock-and-key mechanism predicted in simulation [23, 97], it is essential to have particles with Saturn rings. We achieve this by utilizing large silica particles ($2a = 15$

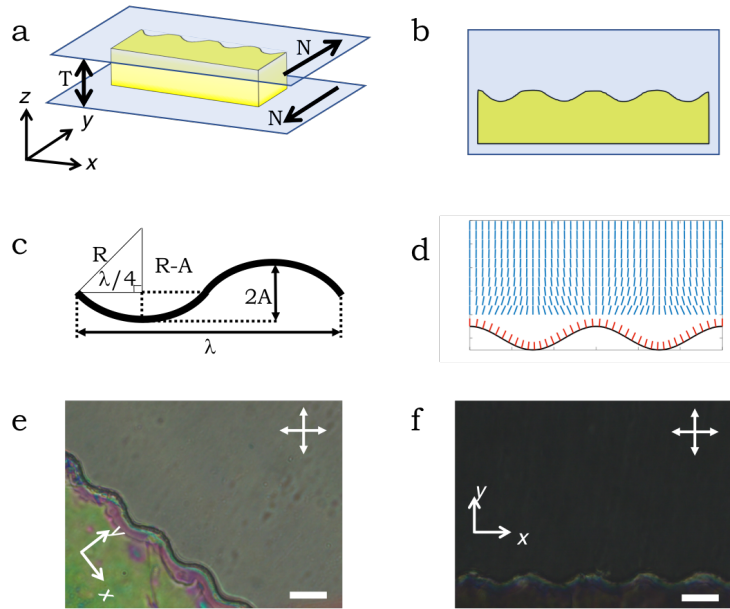


Figure 3.1: Schematics and the director field. (a) Schematic of the experimental setup (\mathbf{N} denotes rubbing direction, T denotes thickness of the cell). (b) Experimental top view. (c) Schematic of the wall shape with relevant parameters: radius of curvature R , amplitude A , and wavelength λ . (d) Simulated director field in the small-slope limit. (e-f) Cross polarized images of liquid crystal near the wavy wall with the long axis either (e) at 45° angle to the polarizer or (f) perpendicular to the polarizer. The scale bars are $20 \mu\text{m}$

μm) whose size not only matched the size of the “lock”, but also is only slightly smaller than the total thickness of the LC cell ($T = 20 - 25 \mu\text{m}$). It is known that confinement from the walls of a LC cell stabilizes Saturn rings against point defects [104]. In particular, the Saturn ring becomes the most stable configuration when the ratio between the radius of the particle and the distance between the particle surface and the wall is bigger than unity. In our case, given the polydispersity of the particles and the uncertainty in the cell thickness, this ratio was between 0.9 and 2.5.

3.3. Docking behaviors of particle with Saturn ring defect

Flat walls with homeotropic anchoring are repulsive to homeotropic colloids [54]. However, wall curvature and the associated splay energy guide the colloid to its preferred site. This occurs only for slowly moving particles located sufficiently close to the wall. Typically, for distance less than $5 \mu\text{m}$, so the elastic energies remain pronounced, and for average drift velocities less than roughly $5 \mu\text{ms}^{-1}$, so distortions of the director field associated with viscous flow are weak. Provided these conditions are obeyed, however, docking is remarkably robust. Close to the edge of the structured wall, a colloidal particle is attracted towards the dale as shown in Fig. 3.2 a-e. The particle, initially situated near a hill on the wavy wall, moves away from this position due to the unfavorable distortion of the director field (Fig. 3.2a). As it floats past the hill, the Saturn ring is visibly distorted away from the equatorial plane to best accommodate the distortion of the external field, indicating that the distortion around the colloidal particle is interacting with the distortion near the wall (Fig. 3.2b). As the particle makes its way toward the dale, the ring is once again distorted, this time lifting a bit, indicating the change of local director field (Fig. 3.2c). Finally, the particle slowly finds its equilibrium position as it sits comfortably in the dale, at the minimum of the shallow well in the wall. As this occurs, the Saturn ring remains distorted (Fig. 3.2e). Here the lock-and-key mechanism appears clearly. In Fig. 3.2f, we present a schematic of the director field around a colloid with a distorted Saturn ring defect docked in a dale. The director field around the colloid matches very well with the director

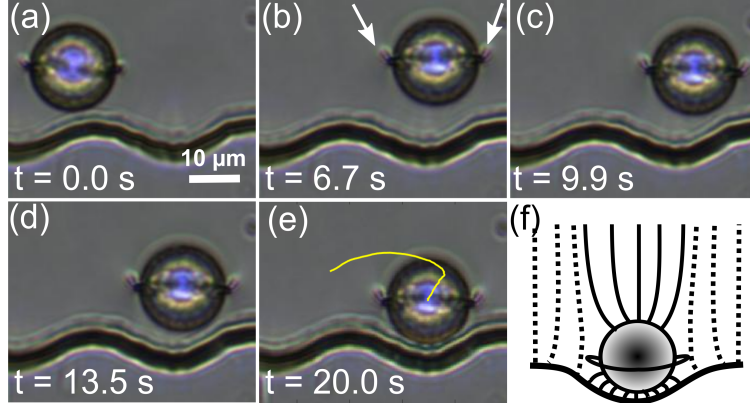


Figure 3.2: Experimental realization of the lock-and-key interaction. (a-e) Time sequence of the particle ($2a = 15 \mu\text{m}$) moving into a cavity of comparable size. White arrows in (b) denote distortion of the Saturn ring. Yellow line in (e) denotes the trajectory of the movement. The trajectory of the particle is extracted by ImageJ and analyzed with MATLAB. This process has been repeated with about 20 different particles and similar trajectories have been observed. (f) Schematic of the director field once the particle docks on the dale, minimizing the total splay distortion.

field inside the dale.

The trajectory traced by the particle's center of mass is shown in Fig. 3.3a; the bold dots demarcate distances of $5 \mu\text{m}$ in arclength s from the initial position of the particle center of mass, which defines $s = 0$. We have observed the signature features of these complex interactions in 5 separate experiments. In the initial stage of the migration, the particle slows down (Fig. 3.3b), owing to viscous dissipation and the elastic energy field near the wall. As the particle migrates past the hill, it accelerates in both \hat{x} and \hat{y} directions, (Fig. 3.3b), as it is “kicked” up diagonally (point **A** in Fig. 3.3a). The particle then moves toward the dale, and slowly overshoots this location (point **B**). At this point, it reverses its direction. Thereafter, it slows down significantly in the last portion as it finds its way into the final docking position (point **C**). Since the kick-reversal-docking behavior is reproducible, we define the binding energy to have contribution from all three components, *i.e.* the entire trajectory as presented in Fig 3.3a.

We measure the average velocity of the particle, and determine the Reynolds number $Re = 3 \times 10^{-6}$ and the Erickson numbers $Er = 0.1$ using typical values for the material constants.

In this limit, viscous forces balance elastic forces that drive the particle’s motion, and the elastic energy landscape is not perturbed by the particle’s motion. This allows the binding energy to be estimated from the energy dissipated over the particle’s trajectory. Since the particle moves in a thin gap of half thickness $l \sim a$ and within a distance $d \sim a$ to the wavy wall (Fig. 3.3c), significant corrections to the viscous drag on the sphere must be addressed to account for these near-wall hydrodynamic interactions. To our knowledge, there are neither analytical results nor simulations of spheres in Stokes flow in a setting akin to our experiment. However, Ganatos et al [28] provide exact solutions for drag on a sphere moving in a thin gap and O’Neill provides drag coefficients for particles parallel to a wall [78]. We estimate the effective drag coefficient by adding these contributions; while this approximation neglects details of the flow in the gap interacting with the flow near the wall, it suffices for an order of magnitude estimate of the interaction energy.

In the NLC 5CB, the viscosity is anisotropic, differing by a factor of roughly 1.6 for motion transverse to or along the director. As most of the particle migration occurs in the x direction, We adopt the value for the viscosity in the transverse direction, *i.e.* $\eta = 14.3$ mPa s, as inferred from the diffusivity measurements of $5 \mu\text{m}$ -sized particles in 5CB reviewed by Lavrentovich [54]. To estimate the energy dissipation U from the initial to final positions, we integrate along the particle path:

$$U = C_D 6\pi\eta a \int_0^{s_f} v ds \quad (3.8)$$

where $C_D \approx 4$ is the effective drag coefficient for this setting, v is the velocity of the particle tangent to the path, and ds is the arclength element. We address the derivation used to obtain C_D in the next section.

We find $U \approx 10^5 k_B T$, orders of magnitude larger than the usual Van der Waals or electrostatic interactions exploited in typical colloidal assembly schemes. A representative graph of the energy dissipated along the trajectory U vs. s is plotted in Fig. 3.3d. This value

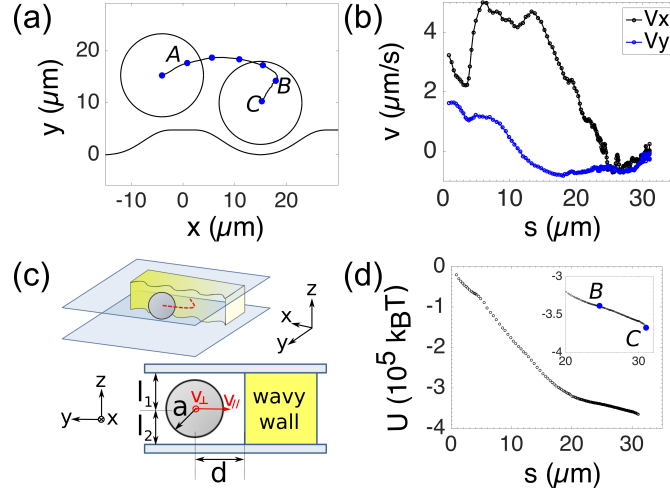


Figure 3.3: Trajectory analysis. (a) Trajectory of the particle: circles denote the initial and final positions. Bold blue dots denotes increments in arc length $s = 0, 5, 10, 15, 20, 25, 30 \mu\text{m}$. Red arrows and capital letters A,B,C denote three events: kick, reverse and docking, respectively. (b) Velocities in x - (black) and y -directions (blue). (c) Particle migrates in a thin gap of half width $l \sim a$ with center of mass a distance $d \sim a$ from wavy wall; hydrodynamic interactions must be addressed in estimate of U . (d) Energy decrease as the colloid approaches docking position.

cannot be compared to simulation, as current computation power precludes detailed simulation of large particles, and addresses energy gradients far weaker than those explored here. Furthermore, most simulations address colloid-well interactions that occur directly above the well, while here most of the interaction occurs as the particles are repelled from hills and move toward dales. If one were to focus only on the final stages of interaction, during the slow reversal and docking process as the colloid moves from **B** to **C** in the last $5 \mu\text{m}$ of the trajectory (Fig. 3.3d inset), energy dissipated is $\approx 10^4 k_B T$. Lock-and-key interaction of particles with wells on walls have been simulated as depletion-driven interactions for particle-wall gap distances similar to the size of solvent molecules [49]. Depletion effects owing to the escape of solvent LC molecules beneath the particle would become significant for gap distances similar to the size of the LC molecules. As our particles settle to gaps of $2 \mu\text{m}$ at the end of the trajectory, we cannot attribute the observed interactions to this effect.

Why do the particles nest in the dales? In simulations of quadrupolar defects docking in

sharp-edged wells [96, 97], the “defect-sharing” mechanism played a prominent role; the particle merged its defect ring with the region of maximum distortion in the director field near the edge of the well. However, in our case (Fig. 3.2), while the Saturn ring is distorted, it is still clearly identifiable. Similarly intact, distorted Saturn rings are shown in Fig. 7 in Hung *et al.* [40] for particles in equilibrium positions in grooves. This suggests a reduced role for defect sharing, and that splay-matching plays a strong role in the particle docking. The localization of particles is related conceptually to particle sorting in the work by Peng *et al.* [80], in which splay deformation was created by photo-alignment. The complex, curved trajectory resembles the curved trajectory analyzed by Pires *et al.* [83], and observed by Skarabot *et al.* [98] and Nikkhou *et al.*[74] for particles docking on a disclination line. In the latter case, the binding energy is very similar to our case, *i.e.* $U \approx 8000 k_B T$. As expected, the value we measure for our particles is larger, as our particles are significantly bigger.[98] This is remarkable, because the director field in our case is non-singular. However, the similarity of the splay field with that around a disclination line may explain the curvature of the trajectory.

The initial position ($s = 0$) (Fig. 3.2a) from which the particle begins its trajectory is roughly one period away from the location where the particle reverses its direction (Fig. 3.2c). This suggests that particles near this location are metastable, and could execute diverging trajectories, one heading over the hill, the other along the “reverse” segment of the trajectory, entering the dale. The distortion of the Saturn ring as the particle travels across different topographical terrains suggests interaction and rearrangement of the director field around it throughout much of the trajectory. Lock-and-key docking on the curved wall is highly reliable. We attribute this robust interaction to gradients in the director field present everywhere near the curved wall that guide particles toward dales, and repel them from other locations on the wall, generating a self-correcting assembly mechanism. In comparison, sharp pyramidal docking sites [96], allow particles to mis-assemble along their planar facets.

In discussing the range of interaction there are two relevant length scales we must consider, the wavelength of the structure and the extrapolation length. In small-slope approximation, assuming infinite anchoring, the disturbance created by the structure decays as $2\pi\lambda^{-1}$ with distance from the structure. However, in real systems, anchoring energies can be finite, causing a second length scale to enter, *i.e.* the extrapolation length, the ratio of elastic constant and anchoring strength, typically also on the microscale. An exploration of system behavior for wavelength comparable to the extrapolation length would be an interesting issue to study in future work to explore how effects associated with finite anchoring energies weaken the elastic energy gradients.

3.4. More detailed drag analysis

In the above discussion, we offer a simplified version of drag analysis to calculate the energy dissipation of the docking event, assuming one-viscosity and average C_D . Yet a rigorous analysis accounting for viscosity anisotropy and position-dependent C_D helps build confidence for future analysis and therefore it is a worthwhile exercise.

In order to account for anisotropic viscosity, we must first decompose the velocity to directions parallel and perpendicular to the wall.

$$\begin{cases} v = \sqrt{v_{\perp}^2 - v_{\parallel}^2} \\ v_{\perp} = v\cos(\theta - \psi) \\ v_{\parallel} = v\sin(\theta + \psi) \end{cases} \quad (3.9)$$

where $\theta = \tan^{-1}\left(\frac{v_y}{v_x}\right)$ and $\psi = \tan^{-1}\left(\frac{dy}{dx}\right) = \tan^{-1}(h'(x))$, assuming the wavy surface is located at $y = h(x)$.

Brenner [9] studies the interaction of a spherical moving perpendicular to a surface, where the Stokes' drag is corrected by a factor of C_{\perp} as a function of normalized distance to the wall $\alpha = \frac{d}{a}$:

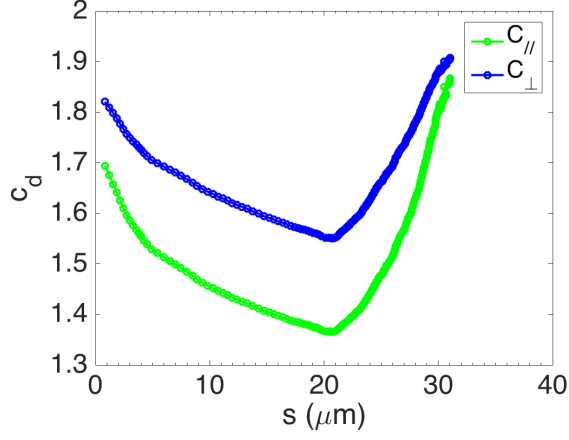


Figure 3.4: Drag coefficients are evaluated at each arclength s from Brenner (C_{\perp}) and O’Neill (C_{\parallel}) calculated from the distance of the colloid from the wall at each point along the trajectory

$$\frac{F_{\perp}}{6\pi\eta av_{\perp}} = C_{\perp}(\alpha) \quad (3.10)$$

C_{\perp} is calculated via Equation (2.19) in Brenner’s paper, the drag correction values are tabulated in Table 1 in the above reference. At $\alpha = 1$, $C_{\perp} \rightarrow \infty$, but for the course of our trajectory, C_{\perp} varies from 1.6 to 1.9 (Fig. 3.4).

The parallel motion of a sphere near the wall is studied by O’Neill [78], the correction to Stokes’ equation owing to the presence of the wall is:

$$\frac{F_{\parallel}}{6\pi\eta av_{\parallel}} = C_{\parallel}(\alpha) \quad (3.11)$$

where C_{\parallel} is also a function of α . It is determined by Equation (26) and tabulated in [78].

Based on the α from our trajectory, C_{\perp} and C_{\parallel} both vary from 1.3-1.9 (as shown in Fig. 3.4).

The movement is also constrained in \hat{z} . Given the symmetries of the experimental configuration and the elastic repulsion from the gap walls, it is reasonable to assume that the particle is centered in the gap. The drag coefficient is given graphically in Fig. 3a in terms of $\beta = \frac{l}{a}$ for a gap of half-width l comparable to the sphere radius a in the analysis of Ganatos, Pfeffer and Weinbaum [28]. From that graph, for spheres and gaps of size that correspond to our experiment, the combined effect of two surfaces yields $C_{gap} = 3$.

Furthermore, the anisotropic viscosity must be accounted for in LC. For micron-sized particle moving in 5CB, typical values of viscosities are $\eta_{\perp} = 14.3 \text{ mPa} \cdot \text{s}$ and $\eta_{\parallel} = 7.83 \text{ mPa} \cdot \text{s}$. Our trajectories consist of prolonged motion parallel to the wall (transverse to the director field), followed by a reversal and docking event (parallel to the director field, with significant near field splay-matching interactions). For this docking segment, the more relevant viscosity is η_{\parallel} .

My aim is to extract an order of magnitude estimate for the interaction energy. We will do this in two ways. In one, we give the transverse viscosity η_{\perp} for the entire trajectory, and estimate the net drag coefficient from the gap and interactions with the wavy wall to be about $C_D \approx 4$. Based on this correction factor, the energy U can be found by integrating the velocity over the entire trajectory using Eq. 3.8. By this method, we find $U \approx 10^5 k_B T$ as stated in the previous section.

In a more careful treatment, we decompose the motion into v_{\perp} and v_{\parallel} . We assume the colloid is close enough to the surface that the relevant viscosity for v_{\perp} is η_{\parallel} , and that for v_{\parallel} is η_{\perp} . We let $C_{gap} \approx 3$. The drag force can be decomposed as follows:

$$\begin{cases} F_{\parallel,gap} = C_{gap}6\pi\eta_{\perp}av \\ F_{\parallel,wall} = C_{\parallel}(\alpha)6\pi\eta_{\perp}av_{\parallel} \\ F_{\perp,wall} = C_{\perp}(\alpha)6\pi\eta_{\parallel}av_{\perp} \end{cases} \quad (3.12)$$

The energy dissipation throughout the trajectory, summing up all contributions:

$$U = 6\pi a \left(\eta_{\parallel} \int_0^{s_f} C_{gap} v ds + \eta_{\parallel} \int_0^{s_f} C_{\parallel} v_{\parallel} ds_{\parallel} + \eta_{\perp} \int_0^{s_f} C_{\perp} v_{\perp} ds_{\perp} \right) \quad (3.13)$$

where s_{\parallel} and s_{\perp} are the parallel and perpendicular components of the arc length s . $s_{\parallel} = s \cdot \sin(\theta - \psi)$ and $s_{\perp} = s \cdot \cos(\theta - \psi)$.

By this method, we find U to differ by 2% from the one viscosity and one drag coefficient approximation. This small difference is owing to the fact that the rate of migration for the last stage of docking after the reversal is extremely slow. For the purposes of an order of magnitude estimate, we give the simpler discussion in the previous section and for the rest of the analysis throughout this thesis.

3.5. Docking behaviors of particles with hedgehogs

We were also able to probe different defect structures around particles. As mentioned, the relative size of the colloids to the LC cell thickness determines whether they form Saturn rings or elastic dipoles. In our experiments, small variations in the size of the particles can favor dipole formation; for particles of diameter $2a = 5 \mu\text{m}$, the elastic dipole is the stable configuration. The elastic dipole also interacts with the curved wall, resulting in a different mode of attraction. The dipole can attach to either hills or dales, according to its orientation with respect to the wall (Fig. 3.5). Our data indicate that the interaction in this case acts at longer range, when the particles are a few tens of microns away from the features. The dipoles migrate towards the surface, since their near field is asymmetrical, they dock selectively onto sites most compatible with the director field. In the case of a dipole with the defect pointing away from the wall, the dale is still the preferred location (Fig. 3.5a,b), but if the defect is oriented towards the wall, the equilibrium position of the colloid is on the hill (Fig. 3.5c,d).

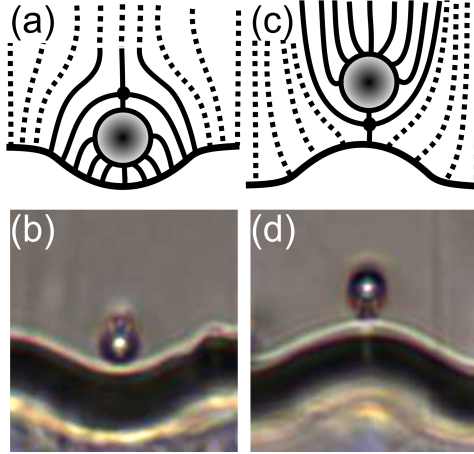


Figure 3.5: Docking of dipoles. Schematic and bright field microscopy images of a particle ($2a = 5 \mu\text{m}$) acting as (a,b) a dipole attracted to a well with its point defect oriented outwards and (c,d) a dipole attracted to a peak with its point defect oriented towards the wall.

3.6. The effect of wall geometry on colloidal behaviors

It is interesting to probe the colloid behavior as the geometry of the “lock” is varied. We find a wide range of behaviors, summarized in Fig. 3.6a, as we change the boundary from one that imposes wells, or shallow wells, to one with wells of greater depth, shown schematically in Fig. 3.6b. We vary colloid diameter $2a$ over the range of 12-17 μm , well depths Δ from 4.5 to 21 μm , and well widths Ω from 16 to 51 μm . Our results indicate that confinement in both the lateral and vertical directions play important roles. When the well width is similar to the particle diameter, and its depth is similar to the particle radius, the lock and key mechanism occurs (filled dots). However, if the colloid is too wide (open dots) the particle is attracted toward the well but becomes stuck on top of it (Fig. 3.6c). Sometimes, in this case, the quadrupole can turn into a dipole pointing away from the wall (open triangles, Fig. 3.6d). If the cavity is too wide and not very deep, the particle does not dock (crosses). However, if the cavity is wide and sufficiently deep to fit the whole colloid inside, the particles does enter the cavity, and the Saturn ring switches to a hedgehog (filled triangles, Fig. 3.6e). Quadrupole-to-dipole transition has been previously induced by electrical field [64], by magnetic field [105], and by flow [42]. Here we show that a distorted

curvature field, without external stimuli, can have a similar effect. A more controlled set of experiments and more detailed analysis of the transition will be presented in the next chapter. For now, it is sufficient to say that for wells of a certain geometry, we can predict the outcome of docking. These results suggest that, by tuning well shape, one can preserve the Saturn ring defect or eliminate it, an outcome of increased interest now with the advent of material assembly within such sites [111].

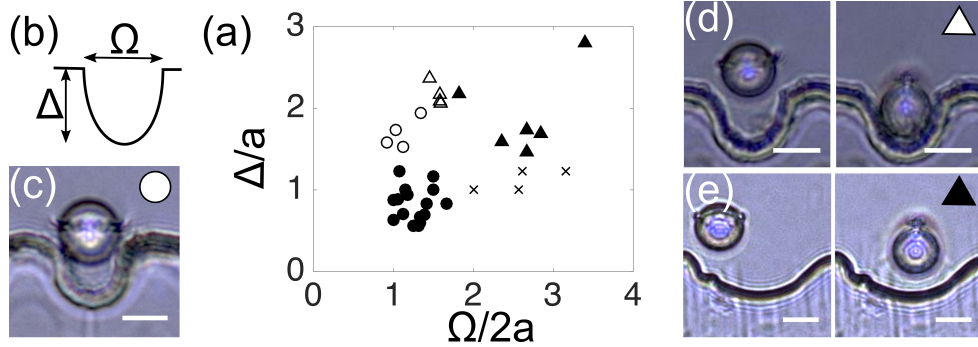


Figure 3.6: Colloids in wells of different dimensions. (a) Phase diagram of behaviors of colloids of radius a in wells of width Ω and depth Δ . Filled circles are cases of successful lock-and-key. Open circles are Saturn ring stuck on top of the wells. Triangles are quadrupole to dipole transitions which are stuck on top of the wells (filled) or enter the well (open). Crosses are cases where the colloids cannot dock. (b) Schematic of wells. (c) Particle with stable Saturn ring trapped at well entrance for $\Omega \approx 2a$ and $\Delta > a$. (d) Quadrupole to dipole transition for $\Omega > 2a$; colloid docks with incomplete entry into well. (e) Quadrupole to dipole transition in a shallow well as the colloid finds an equilibrium distance from the wall. The scale bars are $10 \mu m$.

3.7. Conclusions

We designed a new experimental system to study the interaction of colloidal particles with curved walls that act as sources of splay and bend distortions. The particles migrate towards sites with complementary geometry and similar anchoring. Thus, while particles are typically repelled from planar walls, they are attracted to particular locations on the wavy walls. This ability to turn repulsion into attraction through the curvature of the wall is useful in providing templates to guide colloidal assembly. The distortion of the Saturn rings hints at the complex interaction between the particle's defect and the distorted director field around a structured wall. The range of interaction between the particles and the wall

depends not only on the anchoring of liquid crystals on the particle, but also on the specific type of topographical feature of the wall, suggesting a possible route to sort particles with very small differences in sizes or anchoring strength. In the future, this versatile experimental system can be used to investigate the interaction between different types of “locks” and “keys”. For example, the current experiments only considers spherical particles. However, the investigation could be easily expanded for study particles with different curvatures and anisotropic shapes. Ellipsoids, or faceted platelets, create distortions in the director field and defects which are different from the spherical particles [52], therefore new types of locks, including faceted locks or those that orient high aspect ratio particles, might be carefully designed in terms of shapes and anchoring to have tunable attractions and selectivity of particles. The wall as a source of bend and splay could be recast in other geometries, including “star-like” cross sections that could seed structure growth in differing symmetries. This work could also be expanded to the design of particles with complementary shapes [90], to promote lock and key assembly in the bulk liquid crystal. This system could also be explored for sensing and detection purposes. An example of a sensor sensitive to anchoring was explored in the work by Lin *et al.* [60] for colloidal particles on a nematic droplet.

With respect to the last two examples, the system presented here has the advantage that the location of the sorted particles can be controlled by placing the topographical features on desired locations on a 2D device. This can be exploited, for example, in the design of a microfluidic chip. By varying conditions such as the particles’ size and anchoring, the wall anchoring and geometry, this system is a simple and effective playground to explore various schemes of directed self-assembly. We have shown that sharp corners are able to attract particles at long-range [11, 67] and that the influence of the corners could be felt by particles tens of microns away. In this system, the range of interaction is much smaller. This suggests that ever more exquisite control of the directed assembly of colloids in NLCs can be achieved by combining topographical features that exert a long-range interaction with others that locally guide their position.

In the next Chapter, we will show that by defining a non-singular elastic field through the wavy wall, it is possible to not only position particles precisely near contact with the wall, but also to control migration toward and away from the wall, and assembly at well defined distances from the wall via mediation of well curvature.

Chapter 4

Energy landscape near an undulated boundary

This Chapter is adapted from Ref. [66]. The publication first appeared in Nature Communications [Y. Luo, D. A. Beller, F. Serra, K. J. Stebe, “Tunable colloid trajectories in nematic liquid crystals near wavy walls”, *Nat. Comm.*, 2018, 3841]

4.1. Colloidal assembly in elastic energy landscape

Ever since Brown discovered the motion of inanimate pollen grains, material scientists have been fascinated by the vivid, life-like motion of colloidal particles. Indeed, the study of colloidal interactions has led to the discovery of new physics and has fueled the design of functional materials [22, 69, 116]. External applied fields provide important additional degrees of freedom, and allow microparticles to be moved along energy gradients with exquisite control. In this context, nematic liquid crystals (NLCs) provide unique opportunities [6]. Within these fluids, rod-like molecules co-orient, defining the nematic director field [29]. Gradients in the director field are energetically costly; by deliberately imposing such gradients, elastic energy fields can be defined to control colloid motion. Since NLCs are sensitive to the anchoring conditions on bounding surfaces [8, 87], reorient in electro-magnetic fields [10, 29], have temperature-dependent elastic constants [29] and can be reoriented under illumination using optically-active dopants [57, 70], such energy landscapes can be imposed and reconfigured by a number of routes.

Geometry, topology, confinement and surface anchoring provide versatile means to craft

elastic energy landscapes and dictate colloid interactions [14, 94, 107, 117]. This well-known behavior [6, 85] implies that strategies to dictate colloidal physics developed in these systems are robust and broadly applicable to any material with similar surface anchoring and shape. Furthermore, the ability to control the types of topological defects that accompany colloidal particles provides access to significantly different equilibrium states in the same system. Thus, the structure of the colloid and its companion defect dictate the range and form of their interactions.

By tailoring bounding vessel shape and NLC orientation at surfaces, one can define elastic fields to direct colloid assembly [6]. This was shown for NLC controlled by patterned substrates [59, 81], optically manipulated in a thin cell [76], or in micropost arrays [11, 56], grooves [67, 77, 91], and near wavy walls [68, 97]. In Chapter 3, the energy fields near wavy walls have been exploited to demonstrate lock-and-key interactions, in which a colloid (the key) was attracted to a particular location (the lock) along the wavy wall to minimize distortion in the nematic director field. However, the elastic energy landscapes obtainable with a wavy wall are far richer, and provide important opportunities to direct colloidal motion that go far beyond near-wall lock-and-key interaction.

In this system, elastic energy gradients are defined in a non-singular director field by the wavelength and amplitude of the wavy structure, allowing long ranged wall-colloid interactions. Colloids can be placed at equilibrium sites far from the wall that can be tuned by varying wall curvature. Unstable loci, embedded in the elastic energy landscape, can repel colloids and drive them along multiple paths. In this work, we develop and exploit aspects of this energy landscape to control colloid motion by designing the appropriate boundary conditions. For example, we exploit metastable equilibria of colloids to induce gentle transformations of the colloids' companion topological defects driven by the elastic fields. Since topological defects are sites for accumulation of nanoparticles and molecules, such transformations will enable manipulation of hierarchical structures. We also create unstable loci to direct particle trajectories and to produce multistable systems, with broad

potential implications for reconfigurable systems and microrobotics. Finally, we combine the effects of the NLC elastic field and of an external (gravitational) field to demonstrate fine-tuning of the particles' sensitivity to the size of their docking sites.

To mold the elastic energy landscape near a curved boundary, we use more or less the same set as in the previous chapter. Fabrication of the cell is explained in detail in Chapter 2, Section 2.1.3. When observed through the microscope from a bird's-eye view, this configuration forms a quasi-2D system in the (x, y) plane, where y is the distance from the base of a well in the direction perpendicular to the wall. Unless otherwise specified, when reporting colloid position, y denotes the location of the colloid's center of mass (COM). The wavy structure has wavelength λ , radius of curvature R and amplitude A , as shown in Fig. 3.1c.

4.2. Attraction to well

To determine the range of interaction of a colloid with undulated walls of differing λ , a magnetic field is used to move a ferromagnetic colloid (radius $a = 4.5 \mu\text{m}$) to a position y far from the wall and x corresponding to the center of the well. The magnet is rapidly withdrawn, and the colloid is observed for a period of 2 minutes. If the colloid fails to approach the wall by distances comparable to the particle radius within this time, the colloid is moved closer to the wall in increments of roughly a particle radius until it begins to approach the wall. We define the range of interaction H^* as the maximum distance from the base of the well at which the colloid starts moving under the influence of the wall (Fig. 4.1). In these experiments, the Saturn ring defect was sometimes pinned to the rough surface of the ferromagnetic particles. To eliminate this effect, these experiments were repeated with homeotropic magnetic droplets with a smooth interface whose fabrication is described in the Methods section. The results did not change. A typical trajectory is shown in Fig. 4.1a in equal time step images ($\Delta t = 125 \text{ s}$). For small λ (*i.e.* $\lambda \lesssim 40 \mu\text{m}$), H^* increases roughly linearly with λ . However, at larger λ , the range of interaction increases only weakly. A simple calculation for the director field near a wavy wall in an unbounded medium in the one elastic constant approximation and assuming small slopes predicts that

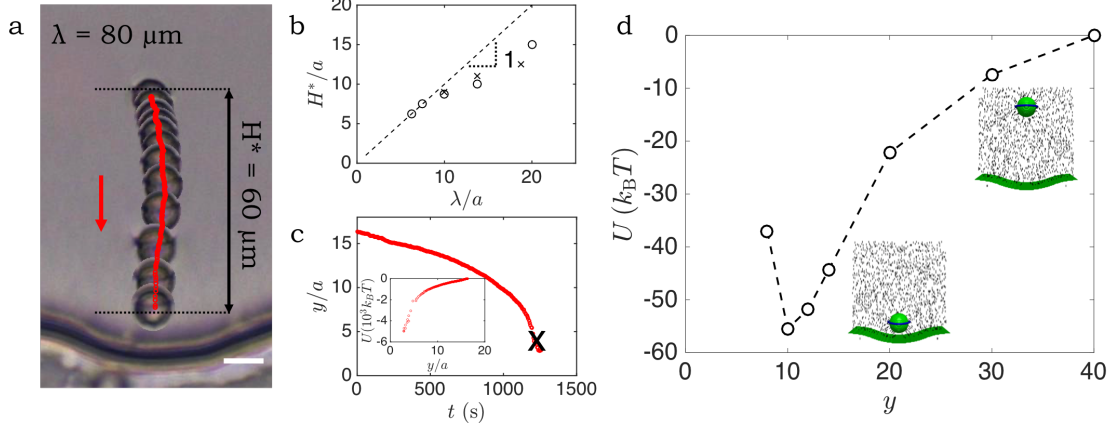


Figure 4.1: Colloid-wall interaction range versus wavelength λ . A ferromagnetic homeotropic colloid with a Saturn ring defect is used to establish the range of interaction H^* of the colloid with the wall. (a) An equal time step ($\Delta t = 125$ s) image is shown for the case $\lambda = 80$ μm , $H^* = 60$ μm . (b) Range of interaction H^* versus the wavelength of the feature λ for homeotropic droplets (open circles) and homeotropic colloids (crosses). (c) The position of the particle y with respect to time t . Inset: Energy dissipated to viscosity along a particle trajectory U with respect to the particle position y . The cross shows where we truncate the trajectory for integration along the path to infer the dissipation. The scale bar is 10 μm . (d) Potential energy by Landau de Gennes (LdG) simulation. The energy of a colloid with Saturn ring defect is simulated by placing it at different distances above a well with normalized radius $R/a = 7$, and normalized wavelength $\lambda/a = 8.5$, where a is the radius of the colloid.

the distortions from the wall decay over distances comparable to λ [68]. However, for λ much greater than the thickness of the cell T , confinement by the top and bottom slides truncates this range (which is explained in more detail in the next section), giving rise to the two regimes reported in Fig. 4.1b: one that complies with the linear trend and one that deviates from it. A similar shielding effect of confinement in a thin cell was reported in the measurements of interparticle potential for colloids in a sandwich cell [110].

The colloid moves toward the wall along a deterministic trajectory. Furthermore, it moves faster as it nears the wall (Fig. 4.1c), indicating steep local changes in the elastic energy landscape. This motion occurs in creeping flow (Reynolds number $\text{Re} = \rho va/\eta \approx 1.15 \times 10^{-8}$, where ρ and η are the density and viscosity of 5CB, respectively, and v is the magnitude of the velocity of the colloid). The energy U dissipated to viscous drag along a trajectory can be used to infer the total elastic energy change; we perform this integration

and find $U \sim 5000 k_B T$. In this calculation, we correct the drag coefficient for proximity to the wavy wall according to [9] and for confinement between parallel plates according to [28] (see Chapter 3, Section 3.4 for more details). The dissipation calculation shows that gradients are weak far from the wall and steeper in the vicinity of the wall. The elastic energy profile found from the LdG simulation as a function of particle distance from the base of the well is consistent with these observations (Fig. 4.1d). The particle finds an equilibrium position in the well. At larger distances from the wall, the energy increases first steeply, and then tapers off (Fig. 4.1d). For wide wells ($\lambda > 15a$), the energy gradient in x near the wall is weak, and the drag is large. In this setting, the colloid can find various trapped positions, and introduce error to the energy calculation. Therefore, the trajectory is truncated at around $y = 15 \mu\text{m}$ from contact with the wall.

4.3. Modeling the effect of confinement

Our setup consists of a colloid in a sandwiched cell. Pair interaction in sandwich cell is truncated at particle distance comparable to cell thickness [110]. For small T/λ , we expect the range to be truncated as well. This effect is modeled by both Landau deGennes (LdG) and COMSOL simulations.

At the glass slide, (Fig. 4.2a, left panel) the oriented planar anchoring is enforced. In the bulk, the wavy wall is a source of distortions (Fig. 4.2a, right panel). We have performed these simulations for a number of cell thicknesses T for fixed $\lambda = 30$; results for $T = 15$ mesh spacing is shown in Fig. 4.2a. By considering slices in xz -plane (constant y), we determine the average absolute values of \mathbf{n} in that plane. This quantity captures the magnitude of the distortion; a value close to 0 means the director field is oriented the same way as the far-field director. As expected, the distortion decays with distance from the wavy wall (Fig. 4.2b). For infinite T , the director distortion decays exponentially with decay length λ ; this asymptote is plotted as the dashed line in Fig. Fig. 4.2b. For finite T , the distortion field decays more rapidly, owing to the anchoring energies on the top and bottom of the cell.

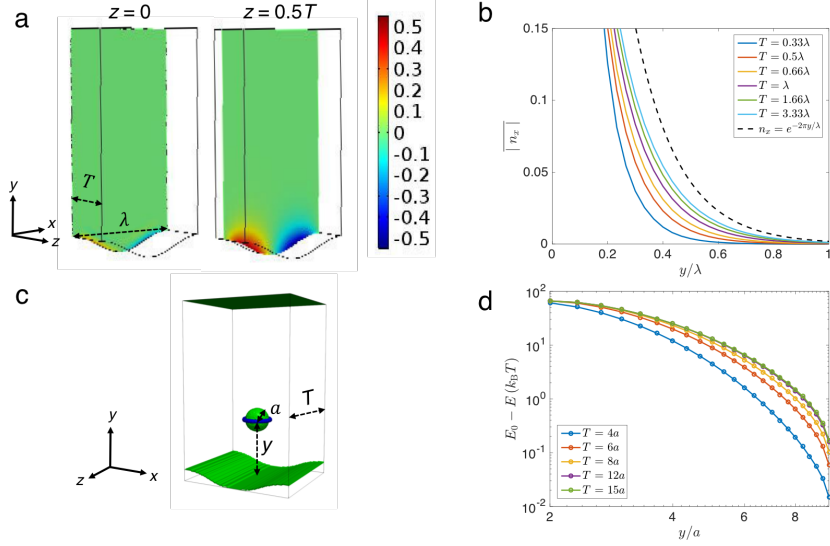


Figure 4.2: Confinement truncates the decay length of wall perturbations in the director field. (a) The color denotes the deviation from 0 of the n_x - component of the director field, which decays with distance y from the wavy wall. The color bar denotes the magnitude of the distortion. At $z = 0$, the wall imposes uniform planar anchoring; thus, at this slice, $n_x = 0$. At the plane $z = 0.5T$ corresponding to the mid-plane between top and bottom plates, the distortion is strongest. (b) The absolute value for n_x , averaged across the gap, versus the colloid's distance y from the bottom of the well. The dotted line corresponds to exponential decay, the limit for an infinite gap width. (c) Schematic of the configuration for LdG simulation of a colloid of radius a with COM at height y above the bottom of the well in a cell of thickness T with a Saturn ring defect. (d) The energies from LdG numerical modeling for cell of thickness T vs. y , normalized by radius of the colloid.

To relate these findings to the distance H^* at which the colloid interacts with the wall, LdG simulation is used to calculate the total energy of the system with a colloid with homeotropic anchoring in a Saturn ring configuration. The colloid of radius a is placed at various distances y from the wavy wall, centered above the well (Fig. 4.2c). The energy of the system is plotted against the distance y normalized by the radius a on a log-log plot for different cell thicknesses T ($= 4a, 6a, 8a, 12a, 15a$, Fig. 4.2d) The plot confirms that confinement diminishes the range of the interaction of the wall.

4.4. Equilibrium position: Splaying matching and distorted Saturn rings

The wall shape also determines the colloid's equilibrium position y_{eq} , *i.e.* the distance between the colloid's center of mass and the bottom of the well. In fact, we show that the

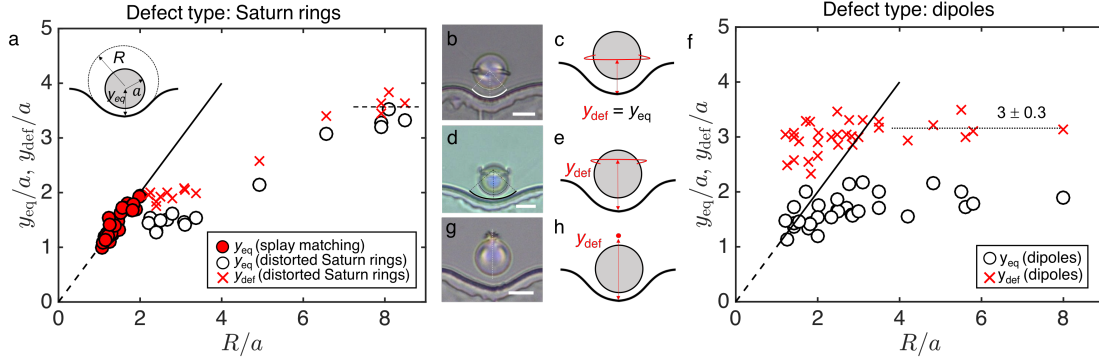


Figure 4.3: Particle-wavy wall interactions. y_{eq} and y_{def} measure the equilibrium distance relative to the bottom of the wells of the wavy wall for the COM of the colloid and the defect. (a) Filled red circles denote splay matching cases, where the Saturn ring sits at the equatorial position ($y_{\text{def}}/a = y_{\text{eq}}/a$). Crosses denote location of distorted Saturn rings, $y_{\text{def}}/a > y_{\text{eq}}/a$. Open circles indicate the height of the center of mass (COM) of the colloid. The dotted line denotes flat wall limit. Inset: Schematic of system geometry. (b-c) Experimental bright field microscopy image and schematic of splay matching. (d-e) Experimental bright field microscopy image and schematic of distorted Saturn ring. (f) Heights of the center of mass (COM, open circles) and hedgehog defects (crosses) of the colloid with dipole defects. (g-h) Experimental bright field microscopy image and schematic of dipoles and their defects. The scale bars are $10 \mu\text{m}$.

particles do not always dock very close to the wall. Rather, they find stable equilibrium positions at well-defined distances from contact with the hills and wells. We probe this phenomenon by varying colloid radius a and well radius of curvature R (Fig. 4.3a). At equilibrium, y_{eq} is equal to R . That is, the colloid locates at the center of curvature of the well (Fig. 4.3b, c). In this location, the splay of the NLC director field from the colloid matches smoothly to the splay sourced by the circular arc that defines the well. As R increases, this splay matching requirement moves the equilibrium position of the colloid progressively away from the wall.

However, for wide wells with $R \gg 2a$, the elastic energy from the wall distorts the Saturn ring, displacing it away from the wall (Fig. 4.3d, e). When this occurs, the equilibrium position of the colloid is closer to the wall. For all such colloids, the height of Saturn rings (Fig. 4.3a crosses: $y = y_{\text{def}}$) and that of the center of mass of the particles (Fig. 4.3a open circles: $y = y_{\text{eq}}$) do not coincide. Specifically, the particle moves closer to the wall, and the

disclination line becomes distorted, *i.e.*, the Saturn ring moves upward from the equator of the particle so that the particle-defect pairs become more dipole-like (Fig. 4.3g, h). For comparison, we plot the center of mass of particles with point defects sitting near the wall (Fig. 4.3f). We observe that, when the colloid radius is similar to the radius of the wall ($R/a \approx 2$), there is a similar “splay-matching” zone for the dipoles; however, as we increase R/a , the behavior changes. In this regime, the dipole remains suspended with its hedgehog defect at a distance of roughly $y_{\text{def}}/a = 3$ from the base of the well for wells of all sizes. The equilibrium distance of particles with distorted Saturn rings (Fig. 4.3a open circles) is intermediate to equilibria for particles with undistorted Saturn rings and colloids in dipolar configurations with point defects. LdG simulation corroborates the finding that dipoles and quadrupoles equilibrate at different distances from the wall, and that the particle with undistorted Saturn ring sits at $y_{\text{eq}} = 1.8a$ (Fig. 4.4a), while the particle with distorted Saturn ring (Fig. 4.4b) and dipole (Fig. 4.4c) sit at $y_{\text{eq}} = 1.6a$ and $y_{\text{eq}} = 1.5a$, respectively.

A colloid positioned directly above a well moves down the steepest energy gradient, which corresponds to a straight path toward the wall. The energy minimum is found when the particle is at a height determined by R/a , consistent with our experiments (Fig. 4.3b). We also note that at $R/a = 7$, we find $y_{\text{COM}}/a = 3.5$, which corresponds to the equilibrium distance of colloids repelled from a flat wall. However, even at these wide radii, the elastic energy landscape above the undulated wall differs significantly from the repulsive potential above a planar boundary, which decays monotonically with distance from the wall [15]. For colloids above the wide wells, energy gradients in the y -direction are small, but gradients in the x -direction are not. As a result, particles migrate laterally and position themselves above the center of the wells. We have postulated and confirmed the splay matching mechanism to be the driving force of the colloid docking. We expect that by using a liquid crystal that has different elastic constants we can enhance or suppress this effect. For example, for a LC with $K_{11} > K_{33}$, the colloids will preferentially sit closer to the wall to favor bend distortion over splay.

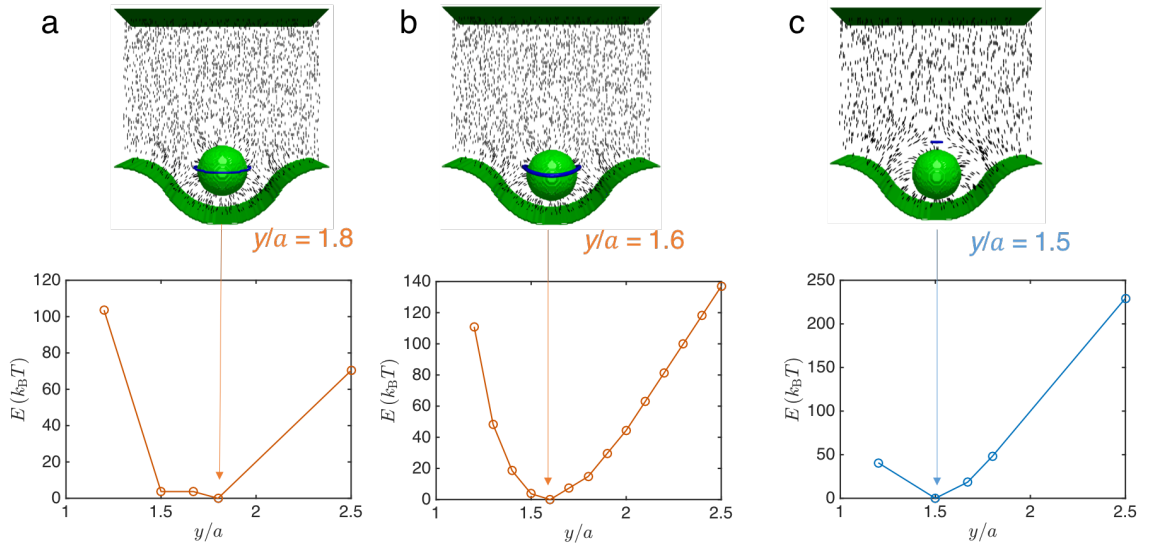


Figure 4.4: Energy of the quadrupole and dipole in wells. (a) Saturn ring reaches lowest energy at $y_{\text{eq}}/a = 1.8$ (splay matching) when simulated with 2.6x core energy where the ring does not distort. (b) Saturn ring reaches lowest energy at $y_{\text{eq}}/a = 1.6$ (distorted Saturn ring) when the 1x core energy. (c) Dipole reaches lowest energy at $y_{\text{eq}}/a = 1.5$ when simulated with 2.6x core energy and initialized with dipolar configuration around the particle. $a = 135 \text{ nm}$, $R = 243 \text{ nm}$, $R/a = 1.8$ in all cases. We have verified that the same equilibrium position hold for system of different sizes as long as the core energy is the same as the cases simulated here. The reference energy is set to be the minimum energy stage corresponding to the equilibrium position.

4.5. Dynamics of quadrupole-to-dipole transition

For micron-sized colloids in an unbounded medium, the dipole is typically the lowest energy state [65]; electrical fields [64], magnetic fields [102] or spatial confinement [32] can stabilize the Saturn ring configuration. In Chapter 3, we showed that a colloid with a Saturn ring defect, stabilized by confinement far from the wavy wall, became unstable and transformed into a dipolar structure near the wavy wall [68]. However, in those experiments, the transformation occurred very near the wall, where the dynamics of the colloid and surrounding liquid crystal were strongly influenced by the details of wall-particle hydrodynamic interactions and near-wall artifacts in the director field. Here, to avoid these artifacts, we use wells with a smooth boundary where $R > a$ and amplitude $A > a$ (specifically, $A = R = 15 \mu\text{m}$ and $\lambda = 60 \mu\text{m}$ or $A = R = 25 \mu\text{m}$, and $\lambda = 100 \mu\text{m}$). These wells are deeper and are best described as semicircular arcs with rounded corners.

We exploit these wider wells to position a colloid with a companion Saturn ring several radii above the wall. The elastic energy field distorts the Saturn ring, and drives a gentle transition to a dipolar defect configuration, as shown in Fig. 4.5a in time lapsed images.

The confinement from the top and bottom glass stabilizes the Saturn ring. The wavy wall, however, exerts an asymmetrical elastic energy gradient on the Saturn ring, displaces it away from that wall, and ultimately destabilizes this configuration. Once the transition to dipole has taken place, re-positioning the particle away from the wall with a magnetic field does not restore the Saturn ring (Fig. 4.5b). The location of the colloid y and the evolution of the polar angle of maximum deflection θ are tracked and reported in Fig. 4.5c. This transition is not driven by hydrodynamics; the Ericksen number in this system is $\text{Er} = 8 \times 10^{-4}$, a value two orders of magnitude lower than the critical value $\text{Er} = 0.25$ at which a flow-driven transition from quadrupole to dipole occurs [42].

Previously, Loudet and collaborators [63] studied the transition of a colloid with a Saturn ring defect to a dipolar configuration in an unbounded medium, prompted by the fast

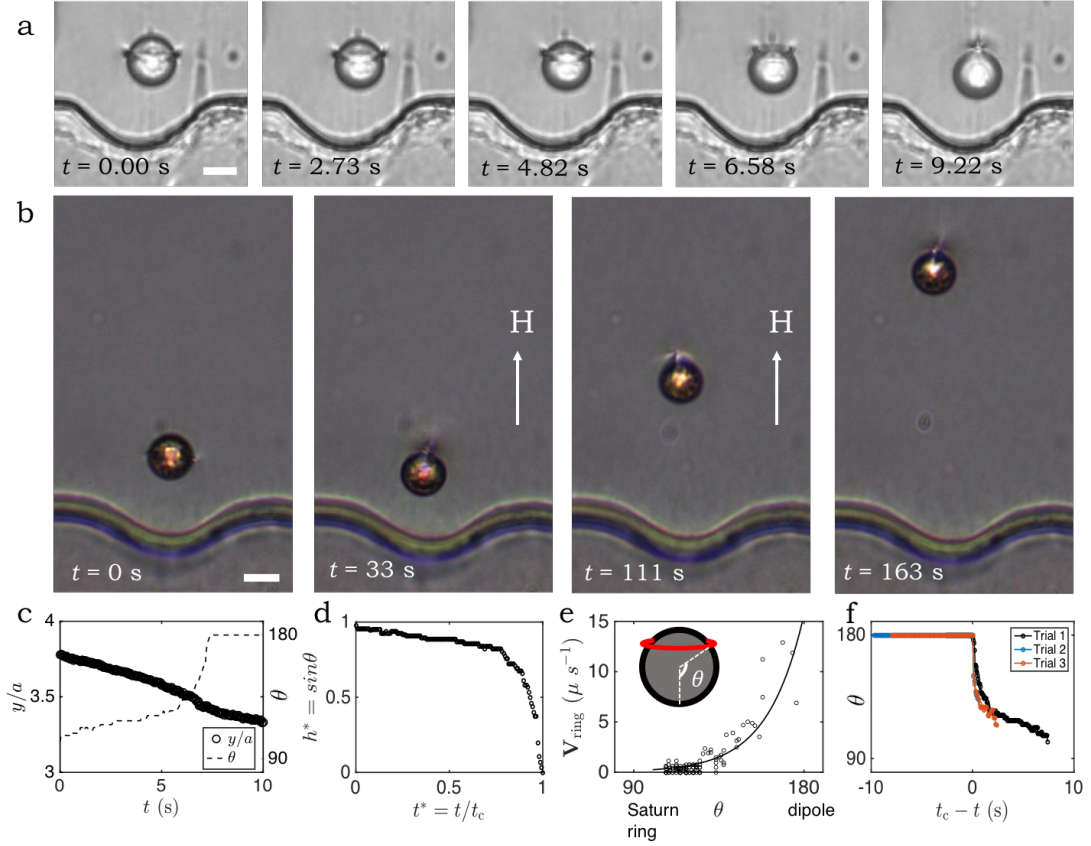


Figure 4.5: Dynamics of the quadrupole to dipole transition. (a) Time-lapse image of a Saturn ring transforming to a dipole at a metastable position remotely from the wall defined by the elastic energy field. (b) Time-lapse image of a Saturn ring transforming to a dipole, then an magnetic field is switched on, moving the particle away from the wall, the quadrupole to dipole transformation is irreversible even though the curvature source has been removed. The scale bars are $10 \mu\text{m}$. (c) The y location of the colloid's center of mass (COM) and evolution of the polar angle θ during the transition. Initially, the colloids assume the $\theta = 90^\circ$ (Saturn ring) configuration, which gradually evolves to $\theta = 180^\circ$ as the COM continuously moves towards the wall. After the transition to a dipolar configuration, the particle approaches the wall. (d, e) Reduced ring size and velocity from our system reveal similar dynamics of transition as shown in Fig. 2 in Reference [63]. The solid line serves as guide to the eye. (f) θ vs. $t_c - t$ plot shows three experimental runs of transition in similar geometry. In (c-e), t_c is the time at which $\theta = 90^\circ$.

removal of the stabilizing electric field. Although these two sets of experiments take place in very different physical systems (confined vs. unconfined, withdrawal of an electric field vs. an applied stress field via boundary curvature), the slow initial dynamics and the total time of transition are common features shared by both (Fig. 4.5d, e).

The dynamics of the transition are reproducible across particles of different sizes, and additional runs with different sized walls and even in the case where debris is collected by the topological defects on the way. However, Loudet et al. observed a propulsive motion attributed to back flow from reorientation of director field in the direction opposite to the defect motion. In our system, the motion is smooth and continuous as the colloid passes through the spatially varying director field. Furthermore, the velocity of the droplet decreases right after transition; we attribute this, in part, to the change in the drag environment (Fig. 4.5c)

There are cases in which the transition does not occur; rather, the Saturn ring remains distorted. In such cases the polar angle then ranges from $\theta = 103^\circ$ to 130° . For polar angles larger than 130° , the transition always occurs, indicating that this is the critical angle for the transition. This value, however, differs from that measured in [99]. This difference may be attributed to the differing confinement of the cell. Differences in anchoring and elastic constants may also play a role.

4.6. Simulation of quadrupole-to-dipole transition

In deeper wells ($A > a$), the polar angle increases as the colloid migrates into the well. LdG simulation reveals that, in the dipolar configuration, there is less distortion in the director field near the colloid owing to bend and splay matching, and that it is indeed more favorable for a colloid with dipolar defect to locate deep within the well (Fig. 4.6a-d). In simulation, we compute the energy of a colloid both far (State 1: $y = 5a$, reference state) and near the wavy wall (Fig. 4.6a-d) to locate the equilibrium site for both the Saturn ring and dipolar configurations (State 2: $y = 1.8a$ and $y = 1.5a$, for Saturn ring and dipolar

configuration, respectively). Details of this calculation are given in Methods. Using the same geometrical parameters and anchoring strength for the LdG numerics, we stabilize a dipolar configuration by initializing the director field by the dipolar far-field ansatz [103]. While colloids in both configurations decrease their energy by moving from State 1 to State 2, the decrease in energy is 2.9 times greater for the dipolar case (Fig. 4.6c,d). This change is determined by differences in the gradient free energy, corresponding to reduced distortion in the nematic director field.

Stark [104] argues that the stabilization of a Saturn ring under confinement occurs when the region of distortion becomes comparable to or smaller than that of a dipole, assuming the same defect energy and energy density. Yet this argument does not apply here because the presence of the wavy wall strongly alters the energy density at various regions in the domain (Fig. 4.6a-d). We can consider the polar angle θ and the director field as our “reaction coordinate” to characterize the transition between the Saturn ring state ($\theta = 90^\circ$) and the dipolar state ($\theta = 180^\circ$, Fig. 4.6e). An energy barrier exists between these two states far from the wall. The experiment indicates that this barrier is eliminated by the elastic energy field of the wall as the colloid approaches the well for certain geometries.

Since this reorganization occurs in creeping flow and at negligible Erickson number, it occurs in quasi-equilibrium along the reaction coordinate. In principle, this suggests that insight can be gained into the transition energy between the two states by simulating the equilibrium value for θ and corresponding system energy E for a colloid Saturn ring configuration at various fixed heights above the wall. Unfortunately, we are limited in how thoroughly we can explore this concept. The particle radii in our experiments are too large to be accurately reproduced in simulations, and must be re-scaled with caution, owing to the correlation length which does not scale with system size.

In particular, our simulations are limited to particle radii for which the dipole is more costly than the Saturn ring everywhere in the domain, *i.e.* far from the wall and in its vicinity. Our experiments, recall, are performed with particle radii for which the dipole

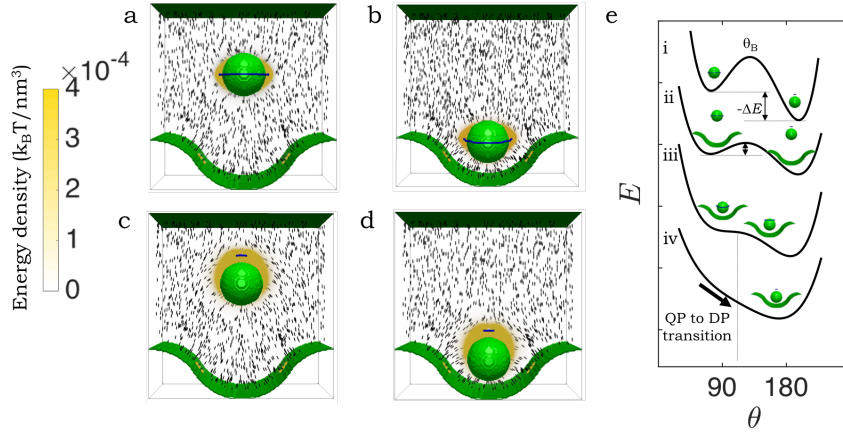


Figure 4.6: Simulated energy density for dipole and quadrupole near a wavy boundary. By exploring the energy for colloids in dipole (DP) and Saturn ring (QP) configurations at various positions above the well for fixed colloid size and wavy wall geometry, the equilibrium heights for the Saturn ring are found. (a) A Saturn ring located at the reference state far from the wall (State 1, $y = 5a$). (b) A Saturn ring located at its equilibrium location (State 2, $y = 1.8a$), a decrease of $203.5 k_B T$ from State 1. (c) A dipole located at the reference state far from the wall (State 1, $y = 5a$). (d) A dipole located at its equilibrium location (State 2, $y = 1.5a$), with an energy decrease of $585.01 k_B T$ from State 1. (e) Schematic representation of the total energy of the system E versus the reaction coordinate θ for several distances y from the well, changing from far from the well to close to the well (i through iv) as E decreases. The presence of the well shifts the angle of the energy barrier's maximum to the right (increasing θ) and decreases the energy barrier until it is eliminated as the particle moves closer to the wall.

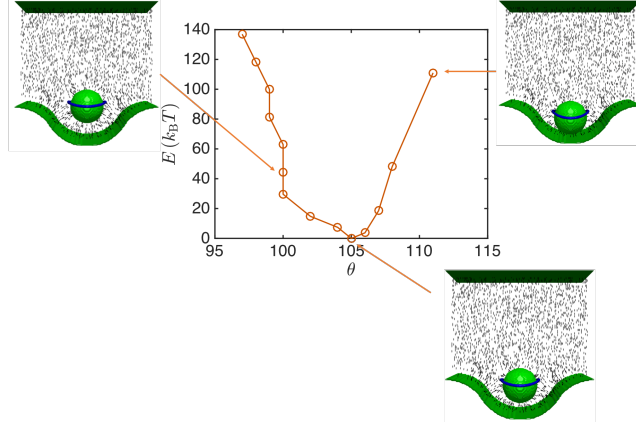


Figure 4.7: Simulation of total energy of the system E versus the reaction coordinate θ . The reaction coordinate denotes the polar angle of the Saturn ring. Snapshot of the equilibrium simulation is attached with the particle is located at various distances from the well. The particle has minimum energy when it is located at the equilibrium position. The reference energy is that of particle at equilibrium position.

is the stable state, and the Saturn ring is metastable. Thus, direct calculations cannot yet capture the manner in which the energy landscape near the wall eliminates the energy barrier between and Saturn and dipole configuration, driving the transformation. Rather, direct calculations of system energy E versus θ for small colloids with stable Saturn rings simply show an energy minimum and an equilibrium ring displacement at their equilibrium height above the well (Fig. 4.7).

We can compare the system energy for quadrupolar and dipolar configurations by computing $\Delta E = E_{\text{dipole}} - E_{\text{quadrupole}}$ (Fig. 4.8). This quantity is always positive for colloidal radii accessible in simulation. By moving closer the the wall, however, ΔE decreases (Fig. 4.6a-d). To explore how ΔE scales with colloid radius, we calculate ΔE in systems of similar geometries in which all length scales are increased proportionally with a for a range of values (colloid radius $a = 90, 135, 180, 225, 270$ nm). The total energy consists of two parts, the phase free energy which captures the defect energy, and the gradient free energy which captures the distortion of the field. The hedgehog defect does not grow with the system size, while the Saturn ring grows with the linear dimension of the system. Thus, the difference in the phase free energy ΔE_{phase} between dipole and quadrupole is always linear

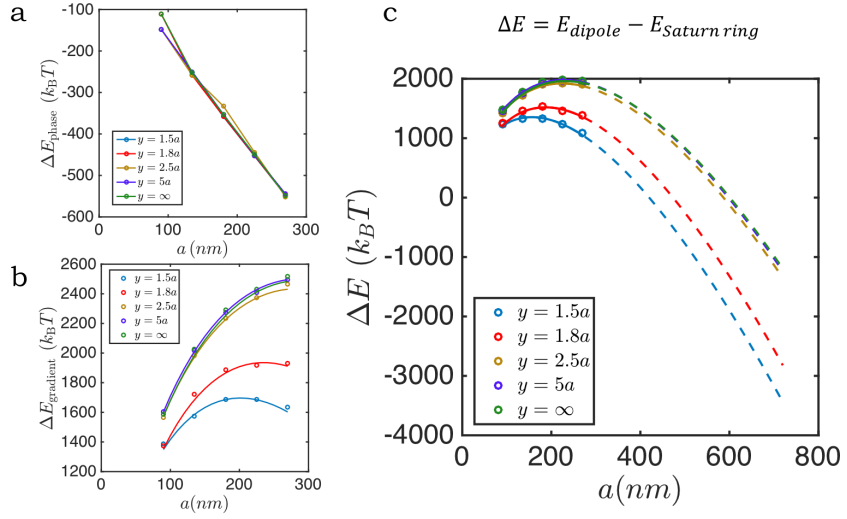


Figure 4.8: Simulated energy density for dipole and quadrupole near a wavy boundary. By exploring the energy for colloids in dipole (DP) and Saturn ring (QP) configurations at various positions above the well for fixed colloid size and wavy wall geometry, the equilibrium heights for the Saturn ring are found. (a) A Saturn ring located at the reference state far from the wall (State 1, $y = 5a$). (b) A Saturn ring located at its equilibrium location (State 2, $y = 1.8a$), a decrease of $203.5 k_B T$ from State 1. (c) A dipole located at the reference state far from the wall (State 1, $y = 5a$). (d) A dipole located at its equilibrium location (State 2, $y = 1.5a$), with an energy decrease of $585.01 k_B T$ from State 1. (e) Schematic representation of the total energy of the system E versus the reaction coordinate θ for several distances y from the well, changing from far from the well to close to the well (i through iv) as E decreases. The presence of the well shifts the angle of the energy barrier's maximum to the right (increasing θ) and decreases the energy barrier until it is eliminated as the particle moves closer to the wall.

in a (Fig. 4.8a). However, the gradient free energy $\Delta E_{\text{gradient}}$ has more complex scaling, with a part that scales linearly in a and a part that scales as a $\log(a)$ [103]. Simulated values for $\Delta E_{\text{gradient}}$ are fitted to such a form ($k_1 a + k_2 a \log(a) + k_3$, Fig. 4.8b).

The sum of these two ($\Delta E = \Delta E_{\text{phase}} + \Delta E_{\text{gradient}}$) for different y values is presented in Fig. Fig. 4.8c (circles: simulated results, solid line: fit, dotted lines: extrapolations to micron-sized particles). Note that for large a , comparable to those in experiment, the linear-logarithmic form fitted to $\Delta E_{\text{gradient}}$ is linear in a . Extrapolation of ΔE according to the scaling arguments presented above suggests that ΔE becomes negative for large enough a . In this limit, the dipole becomes the stable configuration everywhere in the domain, in agreement with experiment. Furthermore, this suggests that, as a particle moves closer to the wall, the dipolar configuration is more favored.

These results show that the distortion field exerted by the wavy boundary can be considered as an external field, in some ways analogous to external electrical, magnetic or flow fields. However, the spatial variations in the elastic energy landscape and its dependence on boundary geometry allow gentle manipulations of colloids and their defects that are not typically afforded by those other fields.

4.7. Saturn ring as manufacturing site

So far we have showed excellent control on the location of defect lines. Recent works by Abbott’s group shows that amphiphilic molecules partition preferentially in defects [111, 112]. By doping the molecules with fluorescent dyes, the defects can be visualized. Furthermore, utilizing photopolymerizable amphiphiles, the structure can be fixed and subsequently released. The defect then becomes a “manufacturing site”. Freezing these configurations via polymerization allows us to probe the fundamental nature of the defect core, which cannot be imaged directly. We can reproduce the previous experimental results following the experimental protocols in [112]. We are able to detect signals from both Saturn ring and dipoles (Fig. 4.9a-b). We steer a colloid near the wavy wall (Fig. 4.9c), either with a magnetic field

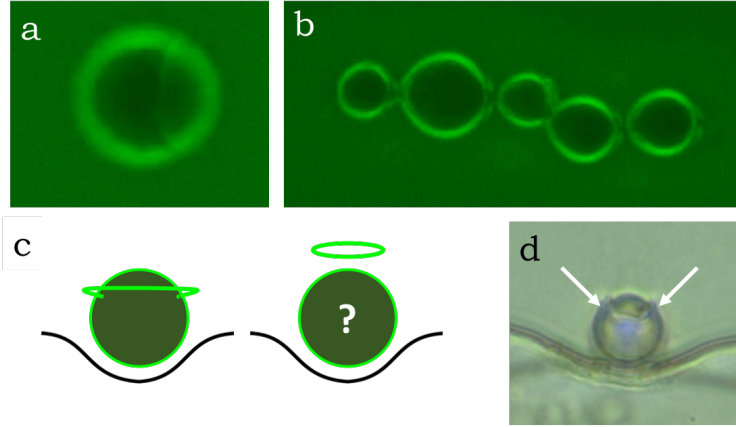


Figure 4.9: Defects as template for assembly. Diyne and BODIPY partition into (a) the Saturn ring (b) dipoles (c) proposed mechanism: as the colloid moves inside the cavity, the Saturn ring is displaced. (d) The displaced defect appears as a slacked ring denoted by arrows.

or by the elastic interaction. The wells are expected to distort the Saturn ring, as before, and eventually make it collapse to a point, but the presence of the amphiphiles can change this scenario. In fact, when a particle with crosslinked defect ring is placed near the wavy wall, the ring appears displaced and slacked (Fig. 4.9d).

4.8. Multiple stable states for particles of various defect types

The elastic energy field in the vicinity of the wall was simulated by placing the center of mass (COM) of a colloid in a Saturn ring configuration at different locations (x, y) . The reference energy is evaluated at $(\lambda/2, \lambda)$, where, recall, λ is the wavelength of the periodic structure of the wall (Fig. 4.10a). The energy in the color bar is given in $k_B T$ for a colloid 54 nm in radius. The vectors in this figure show local elastic forces on the particle, obtained by taking the negative gradient of the elastic energy field. The solid curves indicate a few predicted trajectories for colloids placed at different initial positions in the energy landscape. (Further details of how this energy landscape is generated can be found in Chapter 2, Section 2.2.1). In the preceding discussions, we have focused on attractive particle-wall interactions and associated stable or metastable equilibria, which correspond to the energy minima (blue) above the well. However, the location directly above a hill is an unstable point. When

colloids are placed near this location using an external magnetic field, they can follow multiple diverging paths upon removal of the magnetic field. The particular paths followed by the colloid depend on small perturbations from the unstable point. Trajectories are computed by taking a fixed step size in the direction of the local force as defined by the local energy gradient (Fig. 4.10a).

In our experiments, amongst 28 trials using an isolated homeotropic colloid with a Saturn ring, the colloid moved along a curvilinear path to the well on its left 11 times, to the well on its right 10 times and was repelled away from the peak until it was approximately one wavelength away from the wall 7 times. Three sample trajectories are shown. These trajectories are also consistent with the heat map in Fig. 4.10a. The numerically calculated trajectories (Fig. 4.10a) and their extreme sensitivity to initial position are in qualitative agreement with our experimental results (Fig. 4.10b). Thus, small perturbations in colloid location can be used to select among the multiple paths.

So far we have primarily discussed colloids with Saturn ring defects, but we can also tailor unstable points and attractors for dipolar colloids, and find important differences between the behavior of colloids attracted to wells and those attracted to hills. For example, a dipole pointing away from the wall (Fig. 4.10c) behaves like a colloid with companion Saturn rings in several ways. Both are attracted over a long range to equilibrate in wells, and both have unstable points above hills. Also, when released from this unstable point, both defect structures can travel in three distinct directions (left, right, and away from the wall, Fig. 4.10c). On the other hand, dipoles pointing toward the wall (Fig. 4.10d) behave differently. They are attracted to stable equilibria near hills, and are unstable near wells. Interestingly, when released from a point near a well, these colloids can travel only toward one of the adjacent hills. That is, there is no trajectory above the well that drives them in straight paths away from the wall.

Finally, we observed the behavior of colloids with planar molecular anchoring, which form two topologically required “boojums”, surface defects at opposing poles [86]. They behave

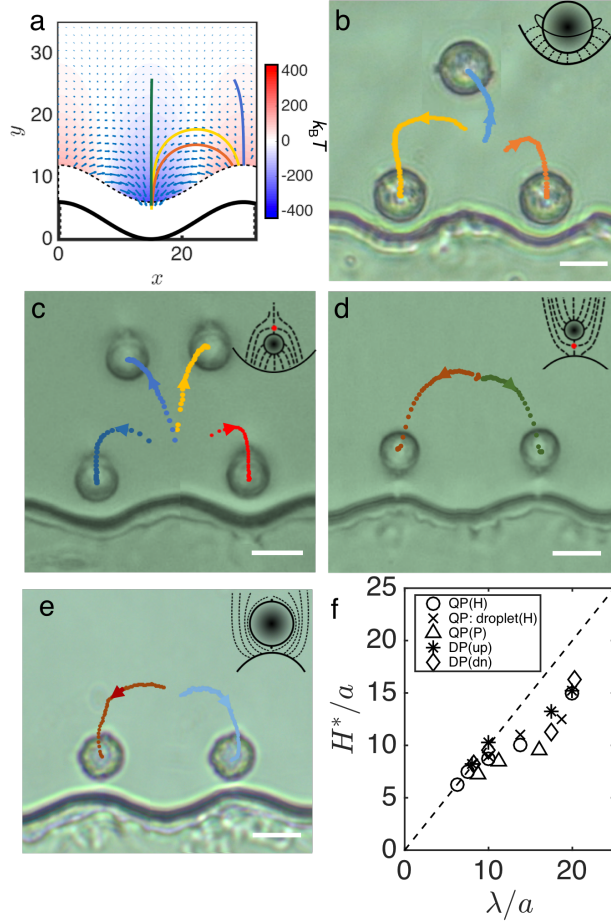


Figure 4.10: Multiple states and reconfigurable docking. (a) Elastic energy field and the resulting forces. (b-e) Particle paths are illustrated by points that indicate particle COM position over time; time step $\Delta t = 5$ seconds between neighboring points. The colored dots denote (b) 3 representative trajectories (out of 28) of a colloid with Saturn ring defect. (c) 4 representatives trajectories (out of 12) of an upward-oriented dipole, (d) 2 representative trajectories (out of 11) of a downward-oriented dipole, and Insets: schematics of colloids with respective defect types. (e) 2 representative trajectories (out of 14) of a planar-anchoring colloid with two boojums released between two neighboring wells. The scale bars are $10 \mu\text{m}$. (f) The range of interaction H^* as a function of λ is similar for homeotropic (H) and planar (P) anchoring, for hedgehog (DP) and Saturn ring (QP) defects, and for solid colloids and droplets.

similarly as downward-orienting dipoles (Fig. 4.10e); they equilibrate near the hills, in accordance with the simulations of [23], and they follow only two sets of possible paths when released from unstable points above a well. The ability to drive particle motion with a gently undulating wall is thus not limited to colloids with companion Saturn rings; the wall also directs the paths of dipolar colloids with homeotropic anchoring and colloids with planar anchoring, decorated with boojums.

These results indicate that the range of repulsion differs for hills and wells. This is likely related to the differences in the nematic director field near these boundaries. While converging splay field lines are sourced from the well, divergent splay field lines emanate from the hill. Both fields must merge with the oriented planar anchoring far from the wall. As a result, hills screen wells better than wells screen hills. The ranges of interaction for various colloid-defect configurations are summarized in Fig. 4.10f; while colloids with each defect structure have distinct equilibrium distances from a flat wall (Fig. 4.11), the range of interaction between colloids and wavy walls follows a similar trend independent of the topological defects on the colloid (Fig. 4.10f).

4.9. Bistable docking of Saturn rings and dipoles

Thus far, we have discussed instances of colloids of different defect structures diverging along multiple paths from unstable points near wavy walls. These features can be used to launch the colloid from one location to another, propelled by the elastic energy field. To demonstrate this concept, we arranged two wavy walls parallel to each other with the periodic structures in phase, *i.e.* the hills on one wall faced valleys on the other (Fig. 4.12a). For wall-to-wall separations more than 2λ , colloids docked, as expected (Fig. 4.12b). For wall-to-wall separations less than 2λ , a colloid, placed with a magnetic field above the peak on one wall, is guided by the NLC elastic energy to dock in the valley on the opposite wall (Fig. 4.12c), thus effectively extending its range of interaction with the second wall. In the context of micro-robotics, such embedded force fields could be exploited to plan paths for particles to move from one configuration to another, guided by a combination of external

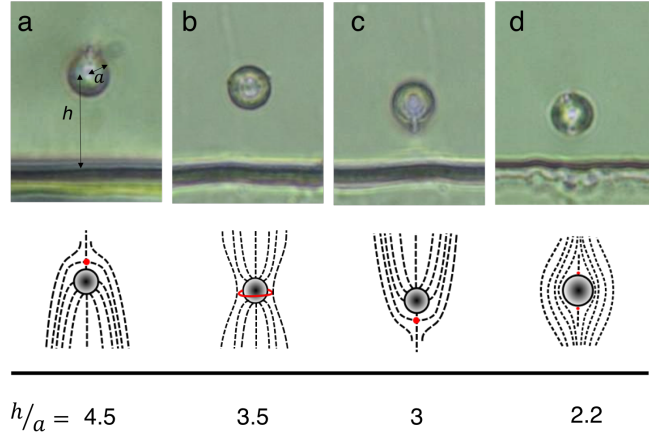


Figure 4.11: Equilibrium distance of particles away from a flat homeotropic wall. Particle diameter $2a = 8.7, 10, 10.2, 9.8 \mu\text{m}$ in a-d. The final equilibrium particle position away from a flat wall for (a) a dipole with its point defect oriented upwards, (b) a colloid with Saturn ring defect, (c) a dipole with its point defect oriented downwards, (d) a colloid with boojums. Defects are illustrated schematically in red in all cases. The scale bars are $10 \mu\text{m}$.

magnetic fields and NLC-director field gradients.

We can exploit these wall-dipole interactions to shuttle the colloid between parallel walls. For walls positioned with their wavy patterns out-of-phase (Fig. 4.12d,), dipoles with point defect oriented upwards are repelled from initial positions above hills on the lower wall and dock on the hill on the opposite wall. However, for walls with their patterns in phase, dipoles with defects oriented downwards released from an initial position above a well dock either at an adjacent hill on the same wall (Fig. 4.12e), or in an attractive well on the opposite wall (Fig. 4.12f).

4.10. Site selection under the influence of gravity

Particles in motion can select preferred places to rest along the wavy wall. Wells with different wavelengths create energy gradients that decay at different, well-defined distances from the wall. Placing wells of different sizes adjacent to each other offers additional opportunities for path planning. In one setting that we explore, a colloid can sample multiple

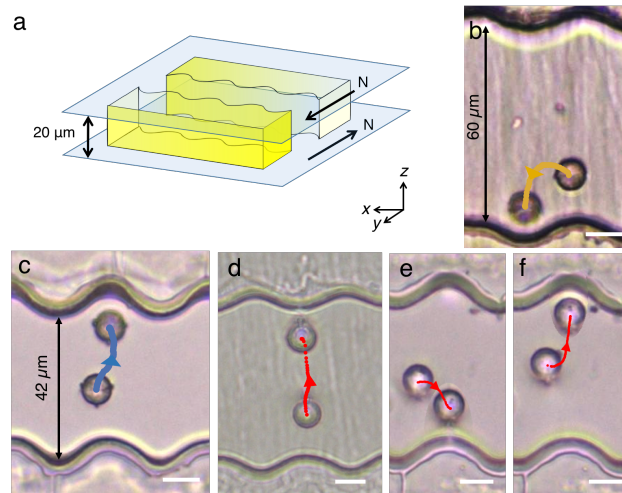


Figure 4.12: Repulsion and bistable docking of dipoles and Saturn rings. (a) Schematic of two parallel walls with a gap comparable to λ between them. (b, c) A magnetic particle with a Saturn ring defect, placed near a hill, with wall to wall separation (b) $60 \mu\text{m}$ and (c) $42 \mu\text{m}$. In (b), the particle is more attracted to the wall on the same side. In (c) the particle is repelled from the hill, and traverses the separation between walls to dock in the well on the opposite side ($2a = 9 \mu\text{m}$). (d-f) Behaviors of the dipoles. The waves of the wall are either out of phase with hill to hill configuration such as in (d) or in phase with hill to valley such as in (e, f). The scale bars are $10 \mu\text{m}$.

wells of varying sizes under a background flow in the x direction. We follow a colloid moving under the effect of gravity. The sample was mounted on a custom-made holder that can be tilted by an angle α (Fig. 4.13a,b) within a range between 10° and 20° so that the colloid experiences a body force in the x -direction. We have verified in independent experiments that, without the wall, the particle moves at a constant velocity due to balance of drag and gravity. In the presence of the wavy wall, the particle's trajectory is influenced by the energy landscape there. We first describe the particle paths over a series of periodic wells, and then describe motion for wells of decreasing wavelengths.

Docking or continued motion in the cell is determined by a balance between the body force that drives x -directed motion and viscous forces that resist it, the range and magnitude of attractive and repulsive elastic interactions with the wall, and viscous drag near the wall. If the particle moves past the well in the x -direction faster than it can move toward the wall, it will fail to dock. However, if interaction with the well is sufficiently pronounced to attract the particle before it flows past, the particle will dock.

For a tilted sample with a wavy wall of uniform wavelength ($\lambda = 70 \mu\text{m}$), colloids initially close enough to the wall dock into the nearest well (Fig. 4.13c, $V_x = 0.01 \mu\text{m s}^{-1}$). Far from the wall, the colloids do not dock. However, the influence of the wall is evident by the fact that the colloids do not remain at a fixed distance from the wall. Rather, the distance from the wall varies periodically, and this periodic motion has the same wavelength as the wall itself (Fig. 4.13d, $V_x = 0.06 \mu\text{m s}^{-1}$).

To simulate the forces on the particle, a particle is placed at different locations near a wall, and the energy of the system is calculated (as detailed in Chapter 2, Section 2.2.1). Gradients in this energy capture the forces on the colloid owing to the distortions of the director field at each location. A uniform body force in the x -direction is then added on the colloid to find the trajectories. We simulated the trajectories for various initial loci. We find two outcomes: for strong x -directed force and/or far from the wall, the particle follows a wavy path (Fig. 4.13e, yellow trajectory); for weak x -directed force and near the wall, the

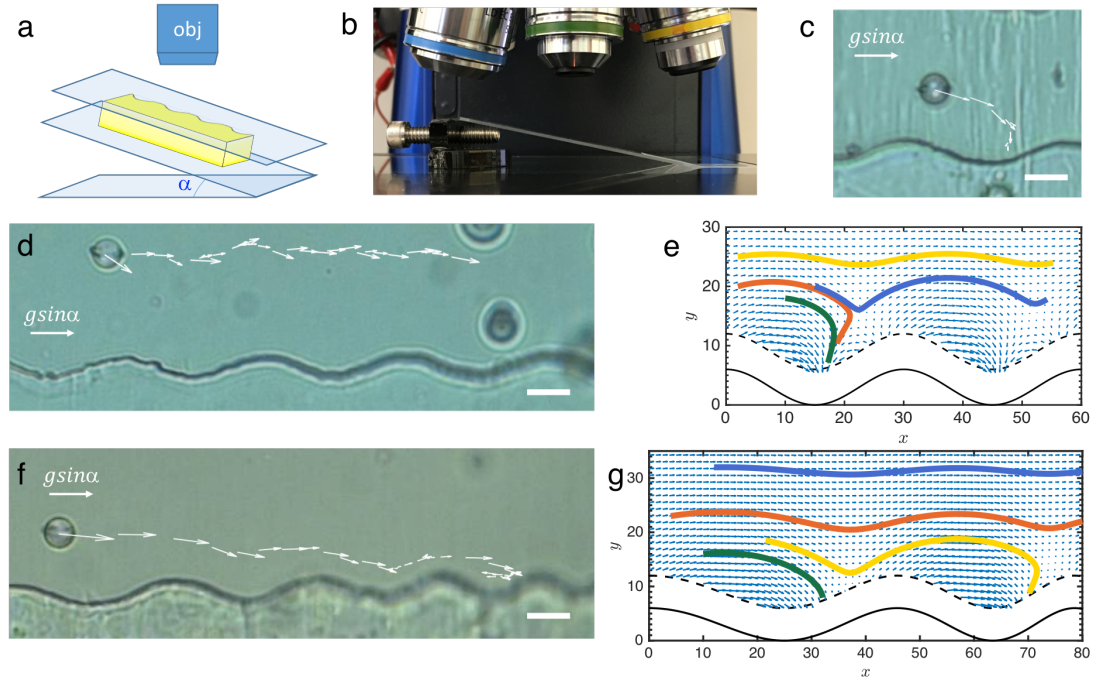


Figure 4.13: A “Goldilocks” colloid in motion docks in a preferred well. (a) Schematic of the experimental setup with tilt angle α to harness gravity to drive colloid motion in x -direction. (b) Image of the setup which allows fine control of the tilt, and thus the x -component of gravitation constant $g \sin \alpha$. (c) A colloid traveling with x -directed velocity $V_x = 0.01 \mu\text{m s}^{-1}$ at tilt angle $\alpha = 11.2^\circ$. (d) A colloid traveling at $V_x = 0.06 \mu\text{m s}^{-1}$ at tilt angle $\alpha = 12.3^\circ$. (e) Particle trajectories at various initial loci predicted for the sum of the elastic energy field and a gravitational potential energy gradient in $-x$ -direction across uniform set of wells ($\lambda = 70 \mu\text{m}$). (f) A colloid traveling at $V_x = 0.09 \mu\text{m s}^{-1}$ at tilt angle $\alpha = 12.8^\circ$ across wells of decreasing wavelengths ($\lambda = 70, 60, 50, 40 \mu\text{m}$). (g) Particle trajectories predicted for the sum of the elastic energy field and a gravitational potential energy gradient in $-x$ -direction. All colloids have $2a = 13 \mu\text{m}$. The scale bars are $20 \mu\text{m}$.

particle docks (Fig. 4.13e, red and green trajectories). A particle slows down right before the hill and speeds up as it approaches the next well. This velocity modulation can be attributed to the interaction with the splay-bend region, similar to particles moving within an array of pillars [14]. Our experiments and simulations are in good agreement, showing both behaviors.

However, a different behavior is observed when we modulate the wavelength of the wavy wall, by placing wells adjacent to each other with different wavelength as defined in Fig. 3.1a. As a particle travels past successive wells of decreasing wavelengths ($\lambda = 70, 60, 50, 40 \mu\text{m}$), the particle moves in the y -direction, closer to the wells, until it eventually is entrained by a steep enough attraction that it docks (Fig. 4.13f, $V_x = 0.09 \mu\text{m s}^{-1}$). This particle, like Goldilocks, protagonist of a beloved children story, finds the well that is “just right”. Simulation of two wells with different wavelengths and a superimposed force confirms these results: we can achieve an additional state not possible with the uniform well, *i.e.* a wavy trajectory that descends and docks (Fig. 4.13g, yellow trajectory). The slight energy difference between wells of different wavelengths underlies the “Goldilocks” phenomena. Since the energy landscape defines zones of strong bend and splay, the ratio between the elastic constants K_{11} and K_{33} is important in determining the particle paths. Such interactions open interesting avenues for future studies, in which the rates of motion owing to elastic forces and those owing to applied flows are tuned, and the trapping energy of the docking sites are tailored, e.g. for colloidal capture and release.

4.11. Conclusions

The development of robust methods to drive microscopic objects along well defined trajectories will pave new routes for materials assembly, path planning in microrobotics and other reconfigurable micro-systems. Strategies developed within NLCs are one means to address these needs. Since the strategies developed in liquid crystals depend on topology, confinement, and surface anchoring, which can be manipulated by changing surface chemistry or texture on colloids with very different material properties, they are broadly applicable

across materials platforms. We have developed controllable elastic energy fields in NLCs near wavy walls as a tool to manipulate the ranges of attraction and to define stable equilibria. We have also exploited elastic energy fields to drive transitions in topological defect configurations. The near-field interaction between the colloid and the wall rearranges the defect structure, driving a transition from the metastable Saturn ring configuration to the globally stable dipolar configuration for homeotropic colloids.

We account for this transformation by means of an analogy between confinement and an external applied field. However, the gentle elastic energy field allows us to access metastable states. As these defect sites are of interest for molecular and nanomaterials assembly, the ability to control their size and displacement will provide an important tool to improve understanding of their physico-chemical behavior, and potentially to harvest hierarchical structures formed within them.

Furthermore, we have developed the concept of repulsion from unstable points as a means to dictate paths for colloids immersed within the NLCs. We have identified unstable sites from which multiple trajectories can emerge, and have used these trajectories to propel particles, demonstrating the multistability made possible by the wavy wall geometry. Finally, we have demonstrated the Goldilocks concept, *i.e.*, that wells of different wavelengths can be used to guide docking of particles moving in a superimposed a flow or via an external force. These concepts lend themselves to actuation and path planning in reconfigurable systems.

In this and the preceding chapter, we have demonstrated fine control over docking and migration a single colloid in NLC near a gently textured boundary. In the next chapter, we relate the concept of docking site developed here to colloidal docking near corners for NLC confined in grooves. We harness the defect-free director field in this geometry to assemble multiple particles. We study the host director field to relate system geometry to regimes it remains defect-free, and to understand the physics of the system as defects appear.

Chapter 5

Wiring particles along director field

This Chapter is adapted from Ref. [67]. The publication first appeared in Physics Review E [Y. Luo, F. Serra, D. A. Beller, M. A. Gharbi, N. Li, S. Yang, R. D. Kamien, K. J. Stebe, “Around the corner: Colloidal assembly and wiring in groovy nematic cells”, *Phys. Rev. E*, 2016, **93**, 032705]

5.1. Colloidal wiring and structure formation in nematic liquid crystals

A motivating study for colloidal assembly in confined NLC exploited the phenomenon of colloidal assembly along defect lines (disclinations) to create wires of colloids [1, 27]. By patterning the surface anchoring on the top and bottom of a sandwich cell, these researchers dictate the origin and termination of a cell-spanning disclination line. Colloids in the bulk become trapped on this line, forming a wire that also spans the cell. The wires can be cross-linked and harvested [1, 27]. However, these disclinations are strong trapping sites. While as the particle-particle interaction scales as $U_{p-p} \approx K\pi a$ where a is the particle radius [85], the particle defect interaction scales as $U_{p-d} \approx \epsilon K a^2 / r$ [65]. As r decreases, U_{p-d} eventually diverges. Colloidal assemblies along disclination lines typically disintegrate only upon melting of the nematic phase. We were inspired by this research to form structures from multiple particles using defect free host director fields. We explore the concept that the gentle elastic energies in the non-singular domain can guide structure formation.

We study colloids suspended in nematic liquid crystal in grooves with homeotropic anchoring. We observe “eyelashes”, topological dipole chains that follow the local, curved director field. These beget wires that connect the groove corners to topographical features on the

cell lid to yield oriented, curvilinear colloidal wires spanning the cell, formed in a non-singular director field. As the groove aspect ratio changes, we find different ground states and corroborate our observation with numerics. These results rely upon on the scale of topographical features, the sharpness of edges, and the colloid-sourced distortions; all these elements can be exploited to guide the formation of reconfigurable structures in nematics.

5.2. Wide grooves

We confine nematic liquid crystal (NLC) in rectangular grooves with corners that act as strong attraction sites for colloids. The experimental setup has been detailed in Chapter 2, a schematic is shown here in Fig. 5.1a.

In wide, shallow grooves ($w = 100\mu\text{m}$ and $h = 50\mu\text{m}$), disclination lines are absent, the director field is non-singular and interior (bottom) corners act as docking sites Fig. 5.1b, inset, the first colloid is polarized, with dipole oriented outwards. Upon docking, each colloid-defect topological dipole attracts more colloids in bulk. In video captured by moving the objective focus the colloids come into focus one by one. One such eyelash is shown in Fig. 5.1b: a chain of dipoles assembles in a curvilinear fashion, following the director field (Fig. 5.1c, d). The director field is approximated with a 2D escape configuration [16]:

$$\theta = 2 \arctan \left(\frac{x}{x_0} \right) \quad (5.1)$$

where θ is the angle between the director and the vertical direction at location x and $x_0 = 40 \mu\text{m}$. We justify this choice because of the director field is defect free. The cross-section of the director field is similar to that of a cylinder in Ref. [16]. The geometry of the groove and the director configuration within will be further discussed later in this Chapter.

More remarkably, under this sculpted director field, a initially randomly dispersed colloidal suspension form roughly equi-spaced curvilinear “eyelashes” that start at interior corners and follow the director field (Fig. 5.2 a,b). A top view of the cell is presented in Fig. 5.2c under polarized optical microscopy (POM), which shows evenly spaced eyelashes along

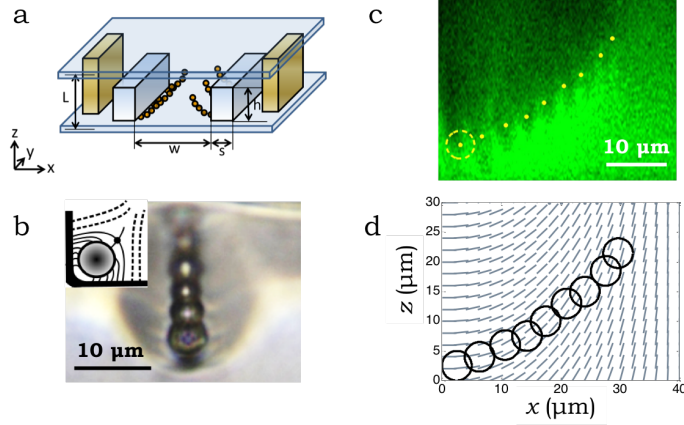


Figure 5.1: A single eyelash. (a) Schematic of the experiment. (b) Top view of the eyelash under bright field (BF). Inset: the bottom corner serves as a docking site. (c) Position of the colloids are found through confocal microscope and (d) superimposed on the director field, the center of mass of the colloids are denoted by yellow dots. In addition, the first colloid anchored at the corner is shown by yellow dotted circle.

the length of the groove. We deduced the director field with the aid of polarizing optical microscopy (POM), fluorescent confocal polarizing microscopy (FCPM, Fig. 5.2c), and via simulation using a Q-tensor based Landau-de Gennes (LdG) model following [3, 5, 89]. Detail of the LdG can be found in Chapter 2, Section 2.2.1, as well as later this chapter. Details of FCPM will be discussed later in this chapter. The director field starts perpendicular to the walls and then bends upwards creating a middle region where it is completely aligned along \hat{z} , as sketched in Fig. 5.2d. This configuration was observed in other LC/colloidal systems with similar geometries [11, 91, 115].

We observe that colloids are attracted to the interior corners (marked 2 and 3 in Fig. 5.2d) between the groove walls and the bottom substrate. These are the regions of strongest splay distortion, where the radius of curvature is small ($\approx 3 \mu\text{m}$ based on scanning electron microscopy measurements). The matching length scale and anchoring conditions between the particle and the corners favors the attraction of the particles, despite the fact that a flat wall with the same anchoring condition would show a repulsive interaction. Although this resembles qualitatively the so-called “key-lock” mechanism [23, 97], the two mechanisms do not precisely coincide: the former has been discussed in the context of particles surrounded

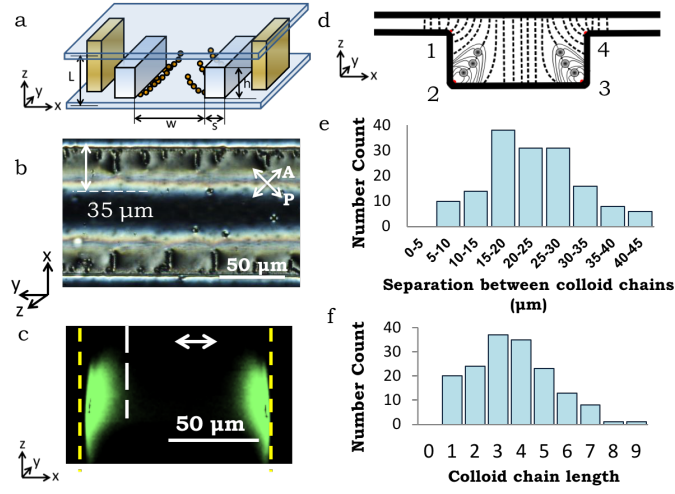


Figure 5.2: Curvilinear assembly forming eyelashes and wires in confined cells. (a) Schematic of cell geometry. (b) POM image of the top view of a channel ($h = 50\mu\text{m}$, $w = 100\mu\text{m}$). Chains are periodically spaced ($\approx 15 - 20\mu\text{m}$) along the bottom edge of the channel. (c) FCPM of a colloid-free channel of the said dimension. Yellow dotted line denote channel boundary. White dotted line denote the range of distortion which is approximately $30\mu\text{m}$. The laser is polarized along \hat{x} (white arrow). (d) Schematic of director field in the groove with the dipolar chains (confirmed by simulation). Histograms of (e) colloidal chain lengths and (f) separations between neighboring dipoles. Only chains that are part of a cluster of 10 or more chains are considered for statistical purposes.

by a “Saturn ring”, a topological quadrupole [29, 48, 107], while here each particle has an associated hyperbolic point defect, making a topological dipole [65, 85]. However, the mechanisms are indeed related: colloids are attracted to docking sites to minimize the distortion of the director field. When the first colloid attaches to the bottom corner, its associated defect points outwards towards the center of the channel. The orientation of the topological dipole propagates along the dipolar chain, which is also outward-pointing (Fig. 5.2d). Thus, typically, the eyelashes are chains of dipoles, starting at the bottom corner of the grooves and following the bending of the director field. The uniform spacing of the eyelashes ($\approx 15\text{-}20\ \mu\text{m}$, Fig. 5.2e), can be attributed to repulsion between the oriented dipolar chains [34]. As dipolar repulsion dictates the spacing between neighboring eyelashes, the polydispersity in spacing between the chains mirrors the polydispersity in the chain lengths (Fig. 5.2f). These assemblies might be exploited, for example, as micro-cilia or micro-mixers. However, many more applications would be possible if we were able not only to *start* and *direct* the wires, but also to *terminate* them and *connect* them between two surfaces: they could template conductive wires or act as soft corrals.

5.3. Point-to-point wiring of particles

To create such connected chains of particles, we added a square pillar array (height $h = 5\ \mu\text{m}$, sides $s = 5\ \mu\text{m}$, pitch $p = 50\ \mu\text{m}$) to the top cover slip, treated to have homeotropic anchoring, like “stalactites”, which may provide a second topographical anchor.

We observe dipolar chains that start at the bottom corner of the groove and follow the director field that bends towards the inverted pillar (Fig. 5.3a). However, a problem emerges at the end of the chain: all the point defects in the chain point outwards, including the last one; the mismatch of dipole orientation prevents the end colloid from attaching to the interior corner at the bottom of the pillar. Instead, the dipolar chain stops at an equilibrium distance from the pillar (Fig. 5.3a,b). A similar scenario takes place when a chain attaches to the pillar first and follows the director field and reaches for the bottom of the channel. The attraction to corners relies upon a particular polarity that propagates

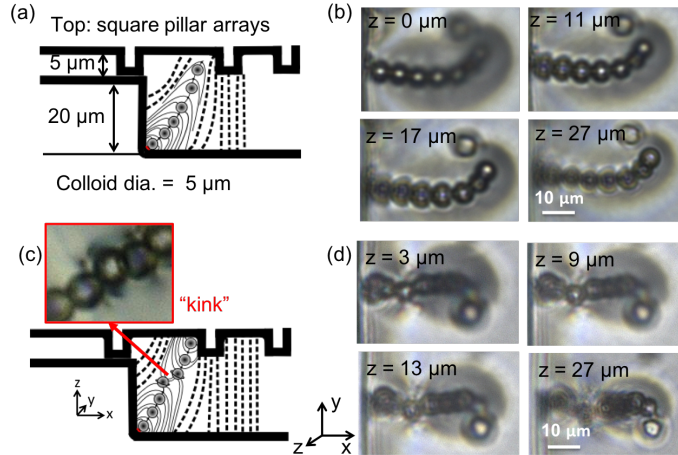


Figure 5.3: Cell-spanning wires created by imposing topographical cues. (a) Schematics of an incomplete wire. (b) BF images with z positions focusing on various points on the wire. The dipole approaches the feature on the top but stops at an equilibrium distance. The chain bends towards the pillar. (c) Schematic and (d) images at different focal planes of a complete wire, formed by reconciling two opposing chains of dipoles with quadrupoles. Inset: experimental observation of a “kink” of connected Saturn rings.

along the chain – is wiring still possible?

The interior corners of the pillars on the top lid can also act as cues to initiate a colloidal chain. Two chains extending from the base of the pillar and the bottom of the groove, respectively, can be guided into close proximity by the director field. When the two dipolar chains are close enough, they have mismatched orientations that frustrate the formation of a wire. However, we observe a restructuring of the defects – the terminal colloids of the two chains become quadrupoles. The partner point defect opens up into a ring that then hugs the colloid, seamlessly connecting two antagonistic chains of dipoles while conserving the topological charge. By eliminating the dipolarity the chains can join in the zig-zag configuration (Fig. 5.3c,d), creating a cell-spanning chain.

5.4. Dynamics of the assembly

We have demonstrated that dipole orientation plays a key role in the formation of the eyelash chains. How do colloids behave far from the corners? We tracked seven sets of

2D trajectories in bulk using optical video microscopy (Fig. 5.4a,b)); the trajectories are decomposed in \hat{x} , perpendicular to the groove axis, and \hat{y} , parallel to it. Migration in \hat{z} is small compared to \hat{x} ($\approx 150 \mu\text{m}$), the reason being that the center of mass of a $5 \mu\text{m}$ colloid levitates $12 \mu\text{m}$ from the bottom wall [54]. We observe that the movement is (roughly) Brownian in \hat{y} (Fig. 5.4c), while ballistic in \hat{x} (Fig. 5.4b,d). We plot the distance $|x - x_f|$ versus time until contact $t_f - t$ (Fig. 5.4b), where x_f and t_f are the final (equilibrium) position and time. To infer the interaction potential U between the particle and the corner, we note that the particle migrates in creeping flow, *i.e.* with Reynolds number $Re = \frac{\rho v l_c}{\mu} = 6.9 \times 10^{-8} \ll 1$ and non-Newtonian effects are negligible, *i.e.* the Erickson number $Er = \frac{\mu v l_c}{K} = 0.03 \ll 1$ based on typical values for the material parameters in literature [30]. Thus, the interaction force $F_{elastic} = -dU/dx$ is balanced by the drag force on the isolated particle $F_{drag} = 6\pi\eta r \frac{dx}{dt}$. We fit the trajectories by truncating them at a distance $d > 70\mu\text{m}$ to ensure a small director gradient and to avoid hydrodynamic interactions with the boundary, and find $|x - x_f| \sim (t_f - t)^{\frac{1}{5}}$. From this power law, we infer that $F_{elastic} \sim 3Ax^{-4}$, and that the particle is attracted toward the corner with a potential $U \sim -Ax^{-3}$, (Fig. 5.4d) compatible with the physical picture of a dipole-dipole interaction.

5.5. Particle-corner interaction

We think of this interaction this way: the corner creates a spatially varying host director field with gradients that are steep in the vicinity of the corner and then weaken far from it (Fig. 5.5a). When the gradients are sufficiently weak, the host field can be expressed in a multipole expansion around any position. A particle at that position perturbs the field, both via the colloid-associated defect and via an induced mode, both of dipolar form, that decay with distance from the particle. These terms interact, yielding the observed potential U . In the steep slope region (Fig. 5.5b), the assumption of weak gradients in the director field no longer applies and the interaction no longer has such a simple form. Rather, we think of this near field interaction as being akin to the lock-and-key mechanism. By nestling in the corner, the colloid removes regions of steep gradients. The particle distortion is well

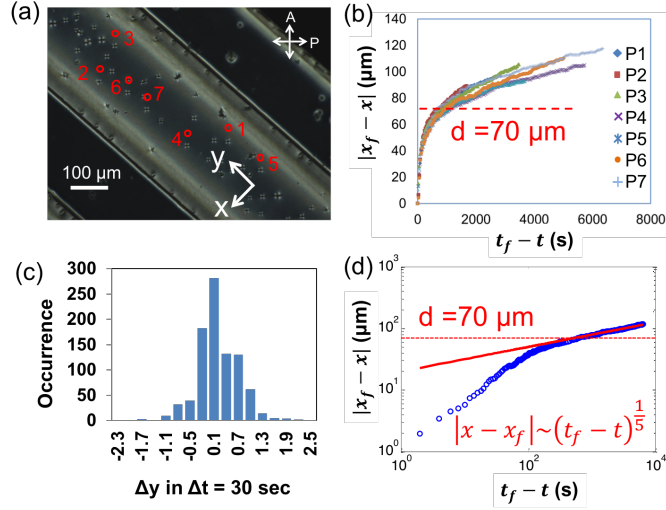


Figure 5.4: Dynamics of assembly for eyelashes. (a) Positions of the colloids tracked in under POM, decomposed in \hat{x} and \hat{y} . (b) \hat{x} -trajectories are ballistic and overlap with each other. The dotted line denotes location of $d = 70 \mu\text{m}$ away from the wall. (c) Displacement distribution Δy in \hat{y} (roughly Gaussian). (d) The $|x - x_f|$ vs. $t_f - t$ plot, fit with a dipolar potential (red solid line) only in the far field (above the red dashed line).

accommodated by the distortion near the wall due to the anchoring conditions of particle and wall. Thus the corner favors the nestling of the particle near the corner, as the liquid crystal can be well oriented in the interstitial region between the particle and the corner, *i.e.* the splay-matching mechanism (Chapter 4, Section 4.4)

Far from the corners, colloids experience a weak interaction and migrate very slowly. During this lag-time, they may also interact with other colloids forming free-floating, short chains in

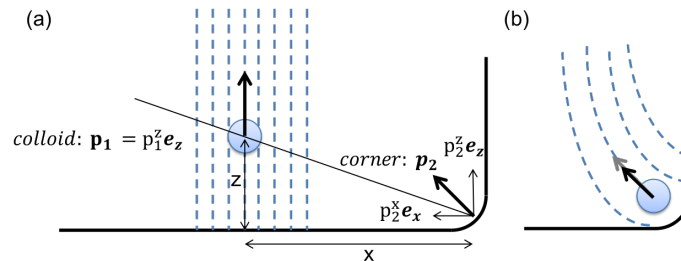


Figure 5.5: Far- and near- field attraction. Schematic of the colloid(1)-corner(2) dipole-dipole interaction in (a) far-field and (b) near-field.

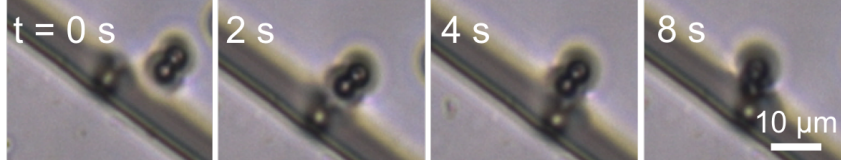


Figure 5.6: Attraction of the corner. A pair of colloids approaches the near-field of a dipole that is already anchored at the bottom corner.

bulk (Fig. 5.6 shows a pair of colloids merging onto an eyelash). These relatively rigid chains migrate to the end of the chain and alter the overall shape of the eyelash. This suggests that the use of narrower grooves would prevent these unwanted aggregates. Furthermore, it would speed up the assembly of both eyelashes and wires (*e.g.* total time of assembly goes from thousands of seconds for channel width $w = 300 \mu\text{m}$ to tens of seconds for $w = 75 \mu\text{m}$). We pursued this task and found that, indeed, narrower grooves do speed up assembly, up to a point. However, strong distortions in very narrow grooves spoil the mechanism.

5.6. Narrow grooves

In narrow grooves, we observe one or more colloid-decorated defect lines, as shown in Fig. 5.7a,b). The changes in colloidal assembly correspond to changes in the director field: in wide grooves, the director field escapes along \hat{z} via splay-bend deformation. In narrower grooves, the two regions of strong splay distortion near the corners come into such proximity that the original configuration is no longer energetically favorable. In the absence of colloids, this leads to an escape in \hat{y} as shown in Fig. 5.7c. However, colloids can lower the free energy cost of defects by inserting themselves into the cores of topological defects [2]. In narrower grooves ($w = 60 \mu\text{m}$, $h = 50 \mu\text{m}$), one of the bottom corners has a bend configuration instead of a splay configuration. This splay-bend transition in corners resemble that discussed in the context of wetting phenomena in 2D grooves [7, 95]. If a colloid is nested near the corner, then the corner can keep the splay distortion. The bend distortion is accommodated on top of the colloid, where the surface anchoring is violated. The compression of the director field leads to breaking the symmetry of the groove: the other bottom corner, in fact, keeps the usual splay distortion with the associated eyelashes as shown in Fig. 5.7d.

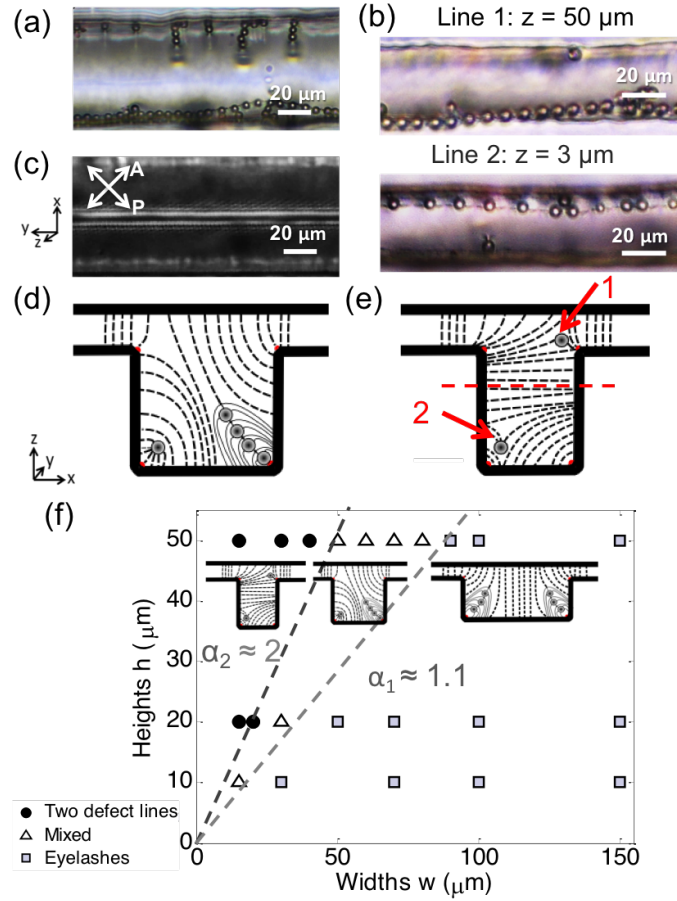


Figure 5.7: Transition from eyelashes along director field to strings of colloids along disclination lines. BF images of (a) mixed state with eyelashes and a disclination line that traps colloids ($w = 60 \mu\text{m}$, $h = 50 \mu\text{m}$), (b) state which traps two defect lines decorated by colloids ($w = 30 \mu\text{m}$, $h = 50 \mu\text{m}$), and (c) POM image of an escape in \hat{y} in a groove with the same dimension as (a) but without colloids. (d-e) Schematics of the director field in (a) and (b) respectively. (f) “Phase diagram” of the structures formed in various geometries. Channel heights h are controlled by spin rates of SU8 photoresist and widths w by photolithography masks.

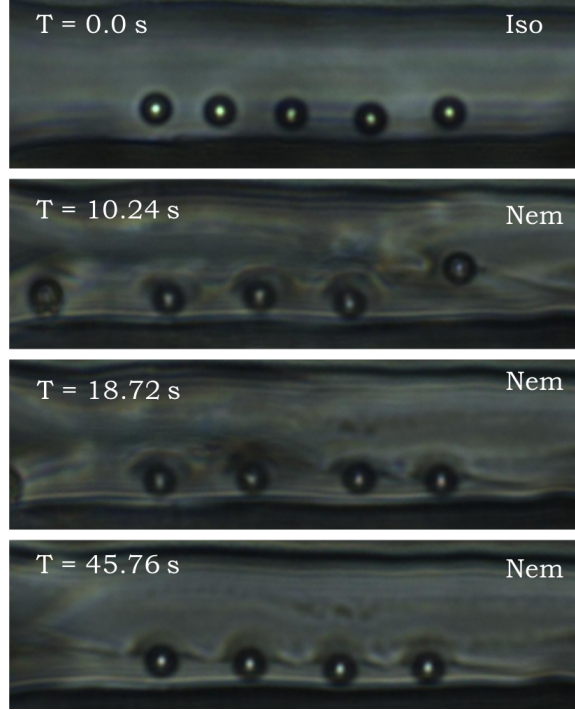


Figure 5.8: Iso-nematic transition in narrow channels. At $T = 0.0$ s the liquid crystal is in isotropic phase, after which it is cooled down to nematic phase. Time-lapse images of the formation of one defect line that collects the colloid initially docked on the corner.

In even narrower grooves ($w = 30 \mu m$, $h = 50 \mu m$), the homeotropic side walls require the director field to align along \hat{x} . The distortion is confined to the top and bottom of the groove. In this configuration, the cell is effectively segregated into two “half cells,” each with hybrid boundary conditions (Fig. 5.7e). which will be further discussed in the next section. The appearance of these defect lines is similar to the case discussed in the context of microfluidic channels [91]: each half cell traps a long defect line that travels along the corners, occasionally crossing the channel in an irregular zig-zag. In this arrangement, “line 1” is pinned at the top edge while “line 2” is located at the bottom, mutually repulsed from each other (see Fig. 5.7b,e). As defect lines form and find their way to either the top or the bottom corner, they collect colloids along the way, creating beads on a chain (Fig. 5.8). The system breaks the yz -plane reflection symmetry and nucleates one or more defects, rather than escaping along \hat{y} , because colloids interact with defects and lower their energetic cost.

These findings suggest that the geometry of the groove determines the mode of assembly. In order to quantify this effect, we built a set of grooves with different heights h and widths w to study LCs in structures with different aspect ratio $\alpha = 2h/w$ (Fig. 5.7f)). Experimentally, the change in colloidal assembly behavior first occurs at $\alpha_1 \approx 1.1$, where the eyelashes stop growing from both sides and only nucleate from one corner. When $\alpha_2 \approx 2$, our system traps two strings of colloids. For $\alpha_1 < \alpha < \alpha_2$ we observe both morphologies. Our observations are in reasonable agreement with our Q -tensor numerics that predict the onset of yz -plane reflection symmetry-breaking at $\alpha_1 = 1.1$ and the alignment in \hat{x} at $\alpha_2 = 2.9$.

To deduce the director field formed within the channels, we used both microscope and LdG simulation specific to this system. The procedures and findings are detailed below. The numerically calculated director fields agree qualitatively with experimental observation. We do not argue, however, that the simulation faithfully mirrors the experiments, due to the different lengthscales involved. In simulation, the colloid is so small that it acts as an impurity; while in experiment one must consider the interaction between the hedgehog and the defect line.

5.7. Fluorescent Confocal Polarizing Microscopy (FCPM)

We performed the experiment with two different LCs: 5CB, which was used in the experimental system, and a binary mixture of low birefringent materials, 4'-butyl-4-heptyl-bicyclohexyl-4-carbonitrile (CCN-47, Nematel GmbH & Co. KG) and 4,4'-dipentyl-bicyclohexyl-4-carbonitrile (CCN-55, Nematel GmbH & Co. KG). This mixture is nematic at room temperature and has low birefringence, and is often adopted as a model system when textures in nematics are characterized using optical methods. The LCs were doped with with 0.01 wt% dye, N,N'-bis(2,5-di-tert-butylphenyl)-3,4,9,10-perylenedicarboximide (BTBP). The dye follows the orientation of the liquid crystal mesogens. By exciting the sample with light of different polarization, we can infer whether the director field has a component in that direction. The dye excites at 534 nm and emits at 585-610 nm [101].

Even with this techniques, samples that contain colloids must be handled with extra care. Initial FCPM trials with 5CB suffered from scattering of index-mismatched colloids and high birefringence, even for a uniformly-aligned cell (Fig. 5.9a,b) where the signal right above the colloid is obstructed by a cone-like shadow (Fig. 5.9b), due to scattering off the colloid. This effect can be mitigated to a great extent by using a low birefringence material such as the CCN mixture. However, in the case of 5CB, the lower defect line, Line 2, trapped more colloids, while in the case of CCN mixture, the top one, Line 1, trapped more colloids. The slight difference might be due to the difference in elastic constants of the LCs, which leads to a different levitation force. The difference translated into a different FCPM image (Fig. 5.9f), where the top corner was slightly darker than the bottom due to scattering from the colloids. Nevertheless, Fig. 5.9f showed a bright region and largely horizontal alignment in mid-height of the cell, which was consistent with the prediction of the director field in Fig. 5.9c.

5.8. Simulations

The specifics of the simulation have been provided in Chapter 2, Section 2.2.1.

We found the minimum energy states by placing the colloid at various locations inside the channel, the energies of different states are first presented in simulation unit, the change in energy is presented in terms of $k_B T$. For channel dimension shown in Fig. 5.10b,c, when the colloid is located in the middle of the cell, the total energy is $U = -4541.64$ (reference). As the colloid “moves” towards the corner, the energy decreases. When the colloid is located at the corner, but the corner has bend deformation as shown in Fig. 5.10b, $U = -4550.01$, or by $31 k_B T$ from the reference; Finally, when the corner has splay deformation, the total energy is further lowered to $U = -4555.98$, or by $54 k_B T$ from reference. Meaning, the system energy can be further lowered by sacrificing surface anchoring on the colloid, creating a melted defect core, in the form of a defect line. For channel dimension shown in Fig. 5.10d,e, we start by placing both colloids at a distance of 45 nm away from all the walls and achieve a total energy $U = -2630.52$ (reference). As we move the colloid to

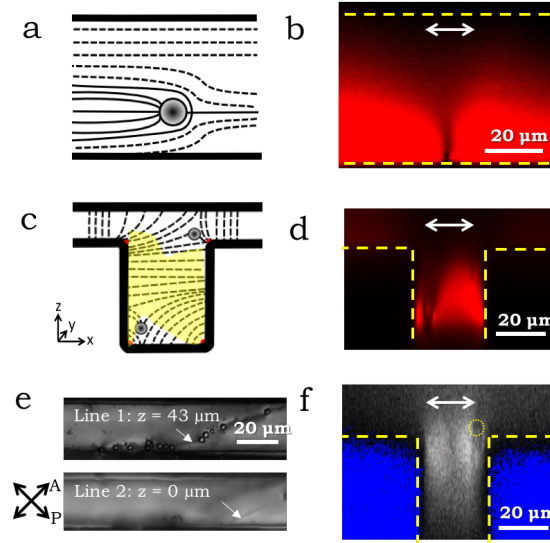


Figure 5.9: FCPM measurements with 5CB and CCN mixture. The scale bars are $20 \mu m$. Yellow dashed lines denotes boundary of the cell in confocal reconstruction (b)(c)(d). (a) A sketch of the director field of a uniformly-aligned planar cell containing a colloid. (b) FCPM of the cell showing a cone-like shadow above the colloid and extinction of signals at about $20 \mu m$ above the the colloid. (c) A sketch of the director field of the director configuration inside of a groove with $h = 50 \mu m$ and $w = 30 \mu m$, where regions of alignment in \hat{x} are highlighted, which are expected to give signal. (d) FCPM of the cell in (c) showing similar extinction pattern and conical section in (b). (e) POM images of the two defect lines in the said cell filled with CCN mixture and colloids. (f) FCPM result of the cell in (e) showing alignment in \hat{x} , consistent with the prediction in (c). The blue color is due to lack of signal (underexposure) inside the groove.

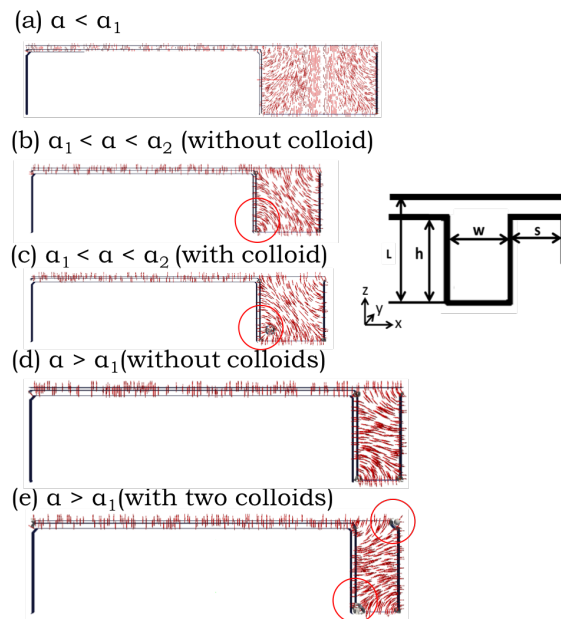


Figure 5.10: Simulation of channels of different aspect ratio. The dimensions of the simulated cases are (a) $h = 225 \text{ nm}$, $w = 450 \text{ nm}$, $\alpha = 1 < \alpha_1$, (c-d) $h = 225 \text{ nm}$, $w = 270 \text{ nm}$, $\alpha_1 < \alpha = 1.67 < \alpha_2$. Red circles denote the corner with bend deformation in (b), simulated without colloids, and splay deformation in (c), simulated with colloids. (e-f) $h = 225 \text{ nm}$, $w = 135 \text{ nm}$, $\alpha = 3.33 > \alpha_2$.

closer and closer to corners, the energy steadily lowers, until it reaches a minimum of $U = -2669.84$, lowered an additional $\Delta U = 149 k_B T$ when both colloids are located at the corners as shown in Fig. 5.10e, which is the lowest energy state for this particular geometry.

The difference of scale may lead to differences in the system behavior in numerics and experiments. Currently available computation power cannot fully resolve the fundamental difference in scale. In particular, given that our system’s colloids are small ($5 \mu\text{m}$) compared with the groove geometry dimensions ($\sim 100 \mu\text{m}$), it is not possible to simulate colloids with dipoles in detail. Thus dipolar chains do not appear in Fig. 5.10a,c. Yet we know they always appear near corners of splay deformation in experiment. There is another important ratio to consider, that of colloid radius d to the anchoring extrapolation length $\xi = K/W$ (K is the elastic constant and W is the anchoring strength). The ratio $d/\xi = 5$ in experiment and 20 in simulation, as the anchoring strength is scaled inversely to system size in simulation. In this work, simulation was used to provide guidance to augment various experimental methods. Nevertheless, in our numerics, as in experiments, the colloids serve to stabilize defect lines. These configurations are consistent with the minimum energy states achieved in simulation in grooves with $\alpha > \alpha_1$. The simulated director configuration is consistent with the experimental observation in BF, XP and FCPM microscopy. The simulation also found similar transition aspect ratios α_1 and α_2 , similar to the phase diagram in Fig. 5.7f obtained by experimental observation. Configurations of the lowest energy state in simulation for all three geometries are shown in Fig. 5.10.

5.9. Conclusion

In conclusion, we have demonstrated two different modes of colloidal assembly in one NLC system. Colloids have “dual-functionalities”: as parts of “eyelashes”, chains of oriented dipoles following a curved director field, or in the more familiar assembly along disclination lines. The intricate energy landscape near regions of high curvature causes a diverse set of structures to form as the groove geometry is varied. These results rely on the interplay of confinement, edge sharpness, and the distortions induced by the colloids and their associated

defects. The eyelashes themselves might be exploited, *e.g.*, as micro-cilia, actuated by flow or by field. By introducing the right topographical cues, they can be manipulated to form full “wires” connecting two walls of a LC cell. This work establishes a new tool to make 3D reconfigurable structures.

Thus far, we have investigated the influence of geometry on a single colloids and multiple colloids. Yet the particle themselves can be tailored for specific interactions, and anisotropic particles are shown to be rich ground to form complex structures [31]. Next, we will look at the interaction of anisotropic particles in NLCs as well as particles near asymmetric walls.

Chapter 6

Open issues

The insights provided within this thesis develop the framework for particle migration and assembly in a sculpted energy landscape within a confined liquid crystalline host. These energy landscapes are controlled by the boundary conditions. Ongoing research builds on the fundamental understanding established in the previous chapters and identifies key extensions and concept space in which we plan to move forward. This work is a collaborative effort by Giuseppe Boniello and Tianyi Yao.

There are a number of ongoing projects that I briefly review here, in order of most to least developed. First, the interactions of ellipsoids near wavy boundaries are addressed. This is a natural extension to the work in proceeding chapters. The interactions of ellipsoids with the walls as a function of ellipsoidal particle aspect ratio and orientation is described in Section 6.1. We also extend the types of wall geometries that we explore. In particular, we study highly asymmetrical wells to explore the concept of a ratchet in Section 6.2, and sharp wall features in order to introduce wall associated defects in Section 6.3. In the presence of these sharp features, the colloid-decorated defect lines get trapped on these features and compete with the docking site where defects are absent. All of the work in this thesis used colloids ranging from $2a = 5\text{-}10 \mu\text{m}$. The ability to precisely position a particles becomes even more challenging for smaller particles, such as those in nanoscale. We have preliminary efforts in which we explore the behavior of particles ($2a = 1 \mu\text{m}$) that are still within optical resolution limit by placing them in a defect-free domain, redesigned to accommodate smaller colloids in Section 6.4.

6.1. Ellipsoids

Anisotropic particles are important tools in studying biological processes such as phagocytosis, which depends heavily on particle shape [13]. They also create much bigger distortion at interface, and their effect must be accounted for in studying capillarity [62]. For that reason, they provide exciting opportunity for particle assembly because they exhibit anisotropic interaction unaccounted for by simple spheres [31]. The ability to generate monodispersed, high-throughput, chemically controllable microparticles of non-trivial shape, merits a field on its own [12, 21, 43, 45].

Particle shape plays a major role in the distortion field made by a colloid in a NLC while topology imposes important constraints on the defects that are realized. A microbullet which is flat on one end and rounded on the other with homeotropic anchoring, always generates a hedgehog defect near the rounded end [30]. Defects tend to pin on the edges while avoiding sharp corner. The wrapping of defect line on edges of the cylinders results in the particle orienting at an oblique angle with respect to the far-field director orientation [5]. Polygonal tiles whose cross-sections are truncated pyramids, also with homeotropic anchoring, always have their defect line loop wrapped around the edge of the larger-area base [92], changing the location of the defect can switch attraction into repulsion [93]. On the other hand, polygonal tiles of planar anchoring form dipoles when the sides are odd and quadrupoles when the sides are even [52], as opposed to the more well-known boojum quadrupoles for spherical particles.

Ellipsoids are natural extension to the spherical particle used previously used for our study [66, 68]. An obstacle that prevent a systematic study of anisotropic particle is finding a way to fabricate particle with controlled anchoring and pinning site, another is the swelling of polystyrene (PS) particle in 5CB. In addressing these two issues, we coat silica on the surface of stretched PS particles, the details can be found in Chapter 2, section 2.1.3. PS particles of two different sizes ($2a = 10, 25 \mu\text{m}$) are stretched. The fabrication process leads to poly-dispersed eccentricities in ellipsoids, and offers opportunities to test out range of

curvatures and aspect ratios (Fig. 6.1a).

6.1.1. Isolated ellipsoids

The defect structure and assembly of homeotropic ellipsoids have been studied previously via simulation and experiments [106]. Dipoles were not included in the discussion, although a dipole-like “tip-ring” configuration has been noted, perhaps due to the limited scale of simulation that is only able to capture nanoparticles. Let θ be the angle between the long axis of the ellipsoid and the y - direction. The tip-ring configuration has lower energy than the mid-plane ring configuration when the particle has orientation $\theta = 0^\circ$. While a particle with Saturn ring defect wrapped around its long axis, and has orientation $\theta = 90^\circ$, it has the absolute minimum energy. In our experiments, with smaller colloids (stretched from $2a = 10 \mu\text{m}$ polystyrene particles), we mostly observe dipolar structures with the dipole localized at the vertex of the ellipsoid (Fig. 6.1b-c). For the ellipsoids with Saturn rings, however, due to the anisotropic shape of the particle, the Saturn ring can wrap around either the minor axis (Fig. 6.1d-e) or the major axis (Fig. 6.1f-g) of the ellipsoid, although the latter occurs far more frequently. This might have to do with the confined nature of our cell, which stabilize the Saturn ring configuration, similar to spherical particles [32]. It is also possible that the particle has limited degree of rotation degree of freedom because of the proximity to top and bottom coverslips. The current state of LdG simulation cannot couple hydrodynamic and elastic interactions, either, and therefore it models the particle as part of the boundary, in equilibrium simulation.

Dipolar ellipsoids are attracted to the hills with their point defect pointing down and assemble head-to-tail to form long chains (Fig. 6.2a), similar to their spherical counterparts [65]. While it is possible for ellipsoids to assemble at 90° with respect to each other if their defects are wrapped along different locations (Fig. 6.2b), it is not commonly observed. The most stable configuration is when two particles assemble in a side-by-side configuration as shown in Fig 6.2c, also confirmed in Ref. [106]. Although we expect the particle to assemble based on their symmetry (quadrupoles), the energy gain of having both particles oriented at

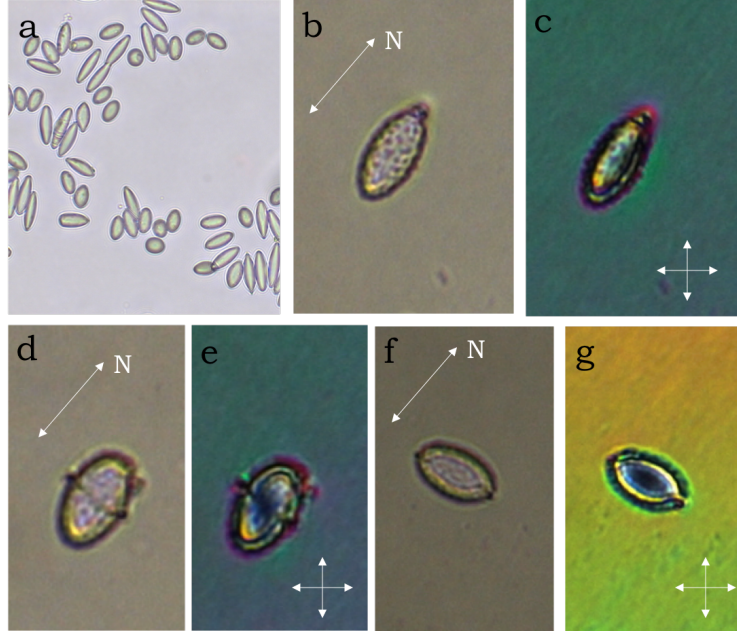


Figure 6.1: Ellipsoids and their defects. (a) Stretched polystyrene ($2a = 10 \mu m$) in water. (b-c) Bright field (BF) and cross-polar (XP) images of a dipole. (d-e) BF and XP images of a Saturn ring wrapped around the minor axis. (f-g) BF and XP images of a Saturn ring wrapped around the major axis.

$\theta = 90^\circ$, and sharing their defect located at the poles, while minimally distort the director field between them, result in a configuration as the one shown in Fig. 6.2c.

6.1.2. Behaviors of ellipsoids near walls

We are interested in exploring the energy landscape of a single ellipsoid next to a wavy wall. We use the same numerical methods (LdG) as specified in Chapter 2, Section 2.2.1 to map out the energy of two otherwise identical ellipsoidal particles ($a = 90 \text{ nm}$, $b = 45 \text{ nm}$, the long and short axis), with the only difference being the orientation of the particle. In Fig. 6.3a, c, $\theta = 0^\circ$; Fig. 6.3b, d, $\theta = 90^\circ$. The two particles have distinct attractive and repulsive regions near the wall. The $\theta = 0^\circ$ case clearly has broader range and farther reach. The $\theta = 0^\circ$ case has a harder time fitting all the way inside the well (Fig. 6.3b). Upon approaching, the particle moves more or less horizontally near the wall (Fig. 6.3b). There is a much smaller attractive region even though the well is large enough to accommodate the

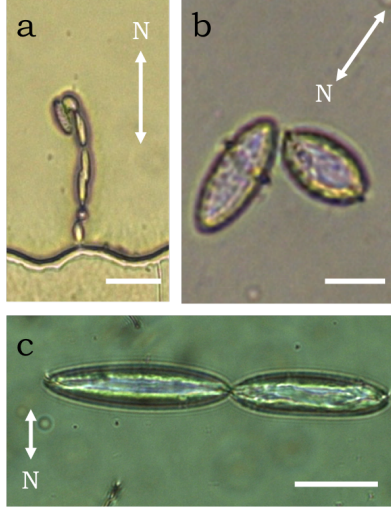


Figure 6.2: The self-assembly of ellipsoids. (a) Dipoles form linear chains. (b) Quadrupoles form kinked structure as they assume based on their symmetry. (c) The most common observed state of the Saturn ring assumes $\theta = 90^\circ$. Two ellipsoids link side-by-side. The scale bars are $20 \mu\text{m}$ in (a) and (c), and $5 \mu\text{m}$ in (b).

colloid. Compare to Fig. 6.3c, where the energy landscape has clearly distinct attractive and repulsive regions near wall, Fig. 6.3d shows that for a particle with $\theta = 90^\circ$, the immediate vicinity of the well is strongly repulsive. It appears that the range of interaction is proportional to the axis of the ellipsoid perpendicular the well. For $b < a$, the range of attraction decays much more quickly for $\theta = 90^\circ$. Intuitively, an elongated object such as the one in Fig. 6.3a will have an easier time fitting inside the well. But in an elastic energy landscape, the reason has more to do with the large volume of LC between the particle and the wall that is able to splay and bend to accommodate the director field around ellipsoid.

For a longer aspect ratio (AR) particle, such as one with $\text{AR} = 4$. The colloid induces even longer interaction range. The colloid range of interaction increase for colloid with $\theta = 90^\circ$ (Fig. 6.4a). But for a high AR object, the attractive region diminishes for a colloid with $\theta = 0^\circ$ (Fig. 6.4b), so is the magnitude of attraction, while repulsion increases. Therefore, it becomes even more difficult for a higher AR object to dock inside the well. In fact, if the particle is larger than the well (Fig. 6.4c), it can still be attracted to the well, sharing its defect with tip of the hill, matching the bend distortion, akin to the case discussed in Ref.

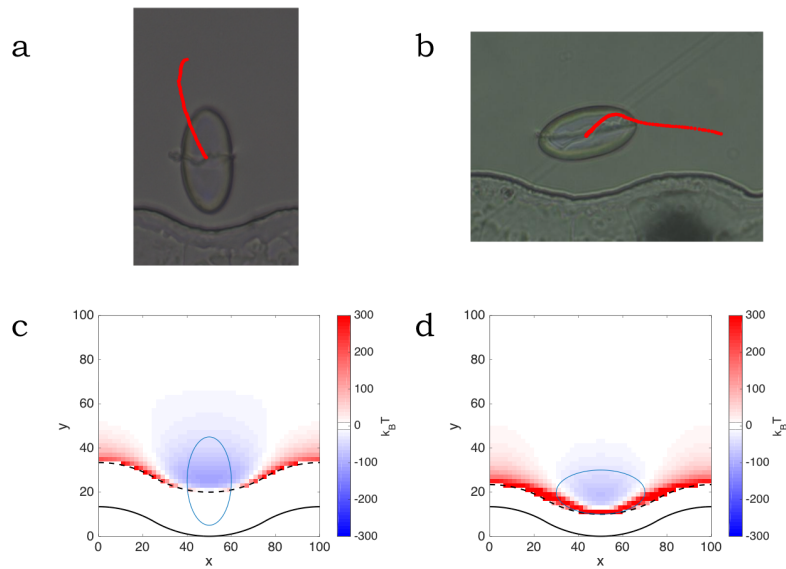


Figure 6.3: Anisotropy docking behavior of ellipsoids (aspect ratio $AR = 2$). (a) An ellipsoid with long axis along the centerline of the well ($\theta = 0^\circ$). (b) An ellipsoid with long axis perpendicular to the centerline of the well ($\theta = 90^\circ$). Red dotted lines denote trajectories. Simulations of total energy of the particle when the center of mass of the particle is located at various locations above the wells for (c) $\theta = 0^\circ$ and (d) $\theta = 90^\circ$. Blue ellipses denote the position the ellipsoid when the system is at lowest energy state. Solid line denotes the wall. Dashed line denotes excluded region below.

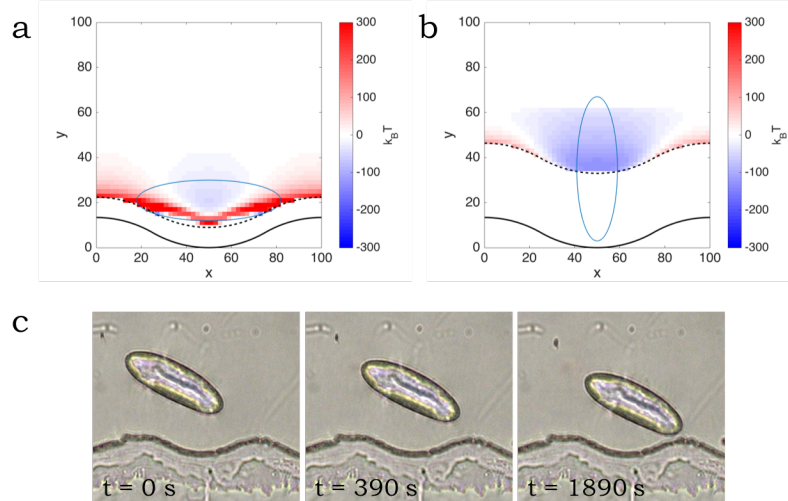


Figure 6.4: Anisotropy docking behavior of higher AR ellipsoids ($AR = 4$). Simulations of total energy of the particle when the center of mass of the particle is located at various locations above the wells for (c) $\theta = 0^\circ$ and (d) $\theta = 90^\circ$. Blue ellipses denote the position the ellipsoid when the system is at lowest energy state. (c) Time lapse image of an ellipsoid of $AR = 4$ docking inside a well that it cannot fit in. The particle docks with one side touching the tip of the hill. Solid line denotes the wall. Dashed line denotes excluded region below.

[97]. But the unfavorable splay energy prevents the ellipsoid from moving further into the well. Thus, the particle docks in a tilted configuration, as shown in Fig. 6.4c. As we have shown in Fig. 4.11 and Fig. 4.3, particle-wall interaction becomes increasingly repulsive as their radii mismatch.

However, a deep well in this case is the perfect docking site for an elongated object, . *i.e.*, the long ellipsoids. Indeed, an ellipsoid can be attracted to dock deep inside the well from a large distance away such as shown in Fig. 6.5. The particle can sense the distortion of the well from far away because of its long aspect ratio. The particle migrates to above the well and eventually inserting itself rapidly into the well. Initially, the Saturn ring is pinned at a slightly tilted configuration, as the particle moves into the well, the tilting is gradually corrected. After the ellipsoid docks, the ring shifts up a little bit to better adopt to the position of the particle. It will be interesting to explore a related type of substrate, a “through-hole”, or a membrane of some sort. In this case, an ellipsoid of the right dimension should be able to plug into the position, preventing transport of a certain material across

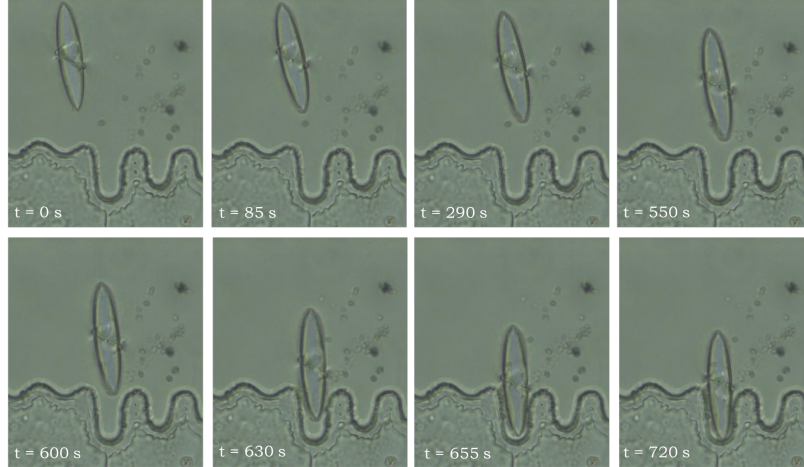


Figure 6.5: Time lapse video of an ellipsoid docking inside a deep well.

the membrane. Upon melting, the ellipsoid can be unplugged, once again allow exchange across the membrane.

6.1.3. Rotation

The dynamic properties of an elongated particle, such as an ellipsoid or a cylinder, are influenced by viscosity anisotropy, and driven by elastic torque [51].

Thus, it is of interest to explore the cases with a tilting angle other than 0° or 90° both in experiment and in simulation. If θ is neither of these values, then the defect will also be tilted, but this state is usually transient. The particles are somewhat constrained in rotation, possibly due to confinement. The defect line may also be pinned. If the particle only deviate slightly from $\theta = 90^\circ$, the director field rearrange. The particle rotates slightly, resulting in a tilted ring. If the particle is closer to $\theta = 0^\circ$, the mid-plane ring wraps around a circumference less than $2\pi b$. This configuration is unstable and transform to the dipolar configuration.

In several instances, we are able to record the transient event of a slightly tilted particle of $\theta \approx 35^\circ$ oriented with a Saturn ring defect transforming into a hedgehog defect (since the Saturn ring is metastable). The point defect always pins at location of highest curvature,

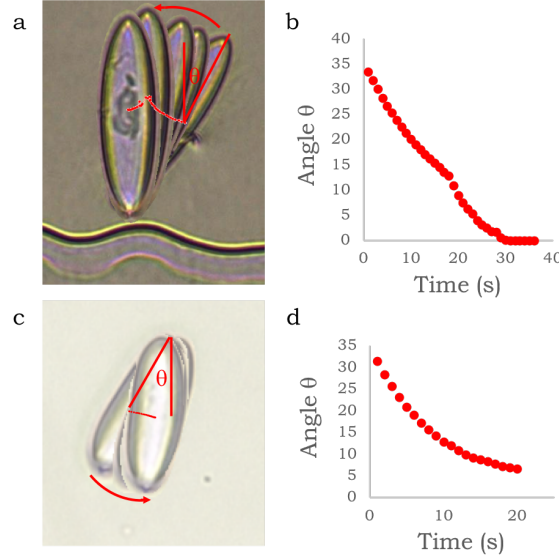


Figure 6.6: Rotation of ellipsoids with dipolar defects. Colloids rotation for (a) near wall and (c) in bulk. Red line tracks the center of mass. θ denote the polar angle. θ vs. t plot for an ellipsoid going through CCW rotation for (b) near wall and (d) in bulk.

located at the pole. The particle always rotates so the dipole is oriented parallel to the global director field ($\theta = 0$), as having a dipole oriented in any other direction is very unfavorable. Dipoles can rotate in bulk as well as near surface. Once they rotate, they interact with the boundary based on the director field around them. For instance, the particle in Fig. 6.6a rotates to dock on top of the hill. Quadrupole-to-dipole transition has been discussed extensively in Chapter 4, Section 4.5-4.6. But the mechanism here are clearly different. In the previous case, the defect transformation is prompted by an asymmetrical director field, while in this case, the defect ring is unstable. Rotation has been observed to take place in bulk (Fig. 6.6c). Similar dynamics of the angle evolution (Fig. 6.6b, d) seems to indicate that the presence of the wall does not really influence particle rotation.

It is possible to image a different class of object, such as a platelet with cross-section of an ellipse. These particle have different distortion at the ends (no component in z). For future work, it will be interesting to compare the behavior of such particles to those of ellipsoids of the same aspect ratio. Next we look at a different kind of anisotropic particle, with wavy side walls that can also serve as docking site for microspheres.

6.2. Asymmetry of particle behaviors near ratchet-like surface

In most of our experimental settings, both the Reynolds number and the Ericksen number are much smaller than unity. Viscous drag balances the elastic force. If the fluid is isotropic, the motion must be reversible. The motion is described by Cauchy momentum equation:

$$\frac{D\mathbf{u}}{Dt} = \frac{1}{\rho} \nabla \cdot \boldsymbol{\sigma} + \mathbf{g} \quad (6.1)$$

where \mathbf{u} is the flow velocity field, $\boldsymbol{\sigma}$ is the stress tensor, \mathbf{g} is all the force per unit mass. For small Reynolds number, \mathbf{g} is negligible. In a liquid crystal, the anisotropy is in the stress tensor, and not in the body force term. Non-Newtonian nature of the fluid gives non-linearity even in Stokes flow. Thus, the trajectory is not truly reversible.

Thus far, we have primarily dealt with symmetrical wells, although aperiodic wells have been explored. In this section, we explore the effect of asymmetry on particle migration. The easiest class of geometry to imagine is a ratchet: an uneven well that is steep on one side (left) and gentle on the other side (right), resembling the side of a ratchet. The ratchet is defined as a device designed so that it is much easier to go one direction versus the other direction [24]. In a sense, the goldilocks experiment is effectively a ratchet (Fig. 4.13), where particle flows one way (big well to small well) and dock, while it does not dock if flowing the opposite way.

An energy map is first constructed by simulating the energy of the system when a colloid is placed at various location, in the absence of external forces (Fig. 6.7), following the same procedure detailed in Section 2.2.1. The energy landscape consists of alternating attractive and repulsive regions. However, the attractive region is asymmetric, and it is stronger on the steeper side.

To map out the colloid trajectory, we take the gradient of the energy field which result in a force field. In simulation, an effective “gravity component” is added everywhere to this

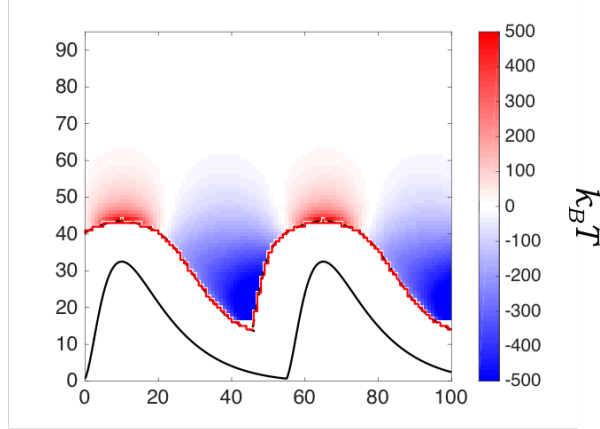


Figure 6.7: Energy landscape near a ratchet surface.

force field. Or else, the particle docks in the closest well. Simulation shows that at high flowing rate, a particle flow in both directions (Fig. 6.8a, b). At moderate flow rate, a particle flows more easily in the direction following than against the teeth of the ratchet (Fig. 6.8c, d). In experiment, the “gravity component” is introduced by tilting the sample as discussed in Section 4.9. At identical tilting angle, a particle flowing in against the teeth of the ratchet (Fig. 6.8e) docks, while one following the direction of the teeth continues to flow, moving in an oscillatory fashion, mimicking the shape of the ratchet underneath, such as the case described in Fig. 4.13d, e. The geometry and behavior of this surface fall much more in line with the behavior of a traditionally ratchet. If a particle moves against the direction of the teeth, it “sees” a stronger attraction site than vice versa, therefore it is more attracted to the well and docks more easily.

It is possible that the colloid in Fig. 6.8e is smaller ($2a = 12 \mu m$), thus it is more strongly attracted to the small confinement of the ratchet geometry, although it experiences the same acceleration as the particle in Fig. 6.8f. Unfortunately, we was unable to test this thoroughly due to the limitation of accuracy of the tilt, and the randomness of colloids’ initial position to establish strict comparison. Nevertheless, it is possible to imagine flowing two population of colloids of different sizes past the ratchet surface. The smaller colloids can dock in a tight well, while the larger colloids cannot due to steric hinderance and elastic

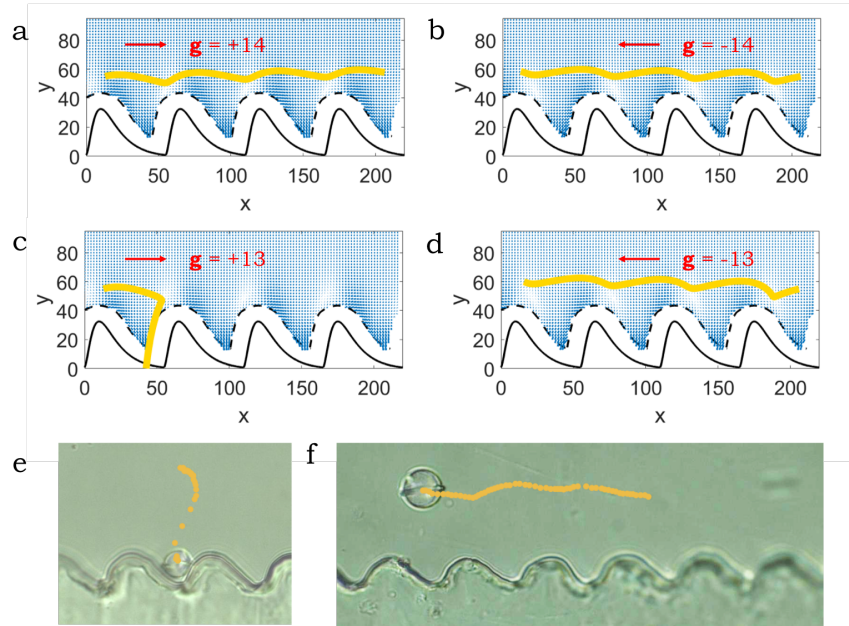


Figure 6.8: Trajectories of particles near a ratchet surface. (a, b) Yellow lines denote trajectories of particles with (a) leftward and (b) rightward “gravity components”, particles flow in both directions. (c, d) At moderate flow rate, the particle docks when flowing against the teeth of ratchet in (c), and flows following the ratchet (d) at identical “gravity components”. (e, f) At identical tilting angle, a colloid ($2a = 12 \mu m$) docks as it flows against the teeth of the ratchet in (e) while a colloid ($2a = 16 \mu m$) keeps flowing when going along the teeth of the ratchet.

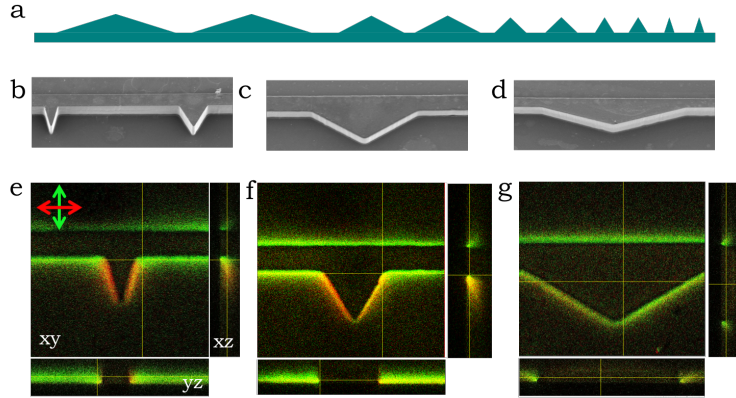


Figure 6.9: NLC near walls with sharp features. (a) Schematic of the mask (b-d) SEM image of the fabricated structures. (e-g)FCPM of the colloid free director field distortion around the teeth with apex equal to (e) 30° (f) 60° (g) 120°

repulsion. Then, it is possible to sort these two types of particles using the uneven surface.

6.3. Hanging chains near sharp features

Thus far, we have been focused primarily on scenarios where the domain is defect-free. Next we will show that a system where defect is present can also interact with corners and curvatures in surprising ways. The sharp features consist of walls decorated with jagged features: triangular prisms whose cross-sections are isosceles triangles. The base angles of the isosceles triangles vary systematically from 15° to 75° at 15° increment (Fig. 6.9a). We use photolithography makes these walls that are about $35 \mu m$ in height. Features of various sharpness are shown in SEM images in Fig. 6.9b-d. The wall is sandwiched between two glass slides. All surface has homeotropic anchoring. At the onset of iso-nematic transition, defect line form between two regions: the well aligned region far from the wall and the distorted region closer to the wall (Fig. 6.9b). The defect line eventually settles and loop around the entire structure. It is situated at the mid-height, as confirmed by FCPM (Fig. 6.9e-g), where the distortion is the strongest.

Colloids ($2a = 5 \mu m$) are dispersed inside the liquid crystal and subsequently loaded into the structure. At the isotropic-nematic transition, there is a defect formed between region

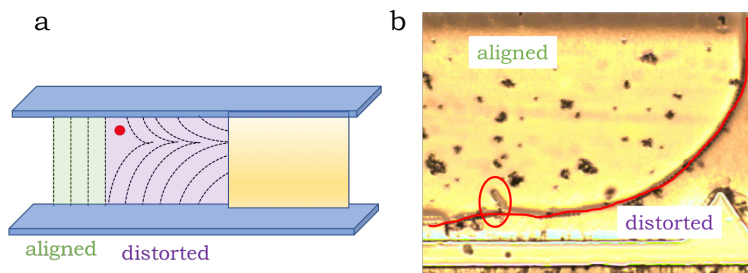


Figure 6.10: Formation of defect line at phase transition. (a) Schematic of the director configuration from a side view. Red dot denote the defect line, observed from the side. There is a well-aligned region (green) far from the features and a distorted region (purple) near the features. (b) BF image of the chain forming at the boundary. A defect line collects colloids during the transition. The red line denote the defect. Circle denotes a chain aggregate which is also attracted to the defect line.

where the homeotropic alignment penetrates completely and region where the alignment is not complete (Fig. 6.10c). The colloids get collected onto the defect line as the defect line is forming, along with aggregates (Fig. 6.10b). This defect chains up in 2D in the plane of observation, forming a long chain of colloids that drifts around the structure. As the colloidal chain sweeps across an area, it collects colloids onto itself. In the process, the chain also reorganizes, straightening itself out. In the end, it is pinned at the corners and the colloids are kinetically trapped in the line such as those shown in Fig. 6.11. Interestingly, when the corners are not as sharp (Fig. 6.11a, b), the chain settle all the way to the pillar; but if the corners are sharp, the chain remains suspended in a trapped state (Fig. 6.11c-e), perhaps due to dipole-dipole attraction between neighboring chain links.

The force a cable experiences determines its shape. For instance, a cable supported by its own weight, *i.e.* the downward force experienced per segment is proportional to the arc length, forms a catenary, or a hyperbolic cosine. While a cable that supports the weight beneath, *i.e.* the downward force experienced per segment is proportional to the projection underneath, forms a parabola. It is interesting to study, for example, how to extract the tension measurements and force the wall exerts on the chain. Since the chain of colloids caught on the tip of the sharp features are pinned (otherwise, the chain would settle), we envision incorporating magnetic colloids and pulling on the string to unpin it. The process

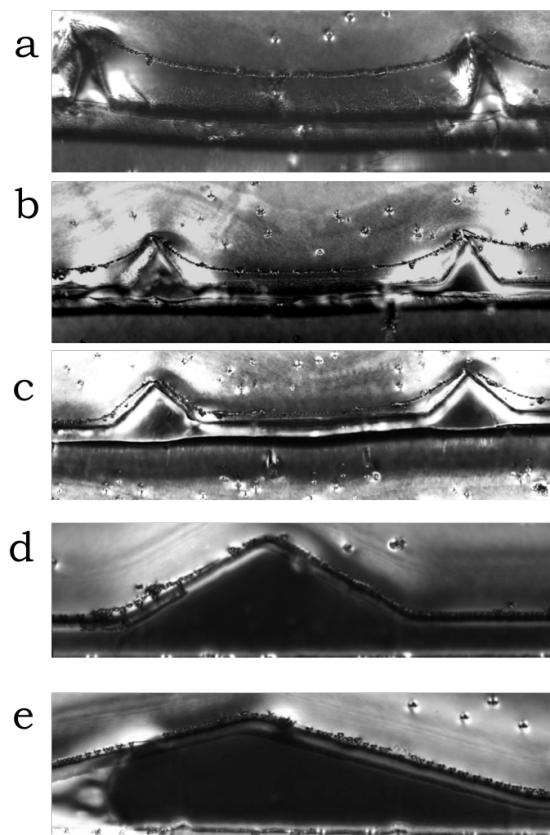


Figure 6.11: Different behaviors of chains get entangled on the structure with different angle. (a) 30° (b) 60° (c) 90° (d) 120° (e) 150°

can be repeated to see if the same equilibrium state is recovered, or if the chain can be detached.

More detailed studies in various fundamental aspects are needed to elucidate how a defect competes with various distortion in the medium, and how defects position themselves in the presence of sharp corners. We have shown that even though corners are strong trapping sites for colloids, when defects are present, these colloids can be easily swept up as the defect line is forming (Fig. 5.8). If sharp features are present, then these lines can be trapped on top of sharp features, while a colloid decorated line can settle all the way to the corner when the features are less sharp. The interplay between defects and non-singular distortion in the director field warrants further investigations.

So far we have focused our effort on the behavior of micron-sized particles. They can be visualized with optical microscopy. But the behavior of nano-particles are even more interesting. We explore them in both a defect-free domain like the ones that discussed so far, and through a different mechanism where they are collected in the Saturn ring defect.

6.4. Scaling down lock-and-key

While micron-scale lock-and-key interaction holds promise for self-healing surface and targeted delivery, more ground-breaking potential of this set up lays in the ability to scale down the system to dictate the motion of sub-micron particles. In nematic liquid crystal, the bulk elasticity scales as length of the system. As a result, the elastic interaction becomes ever weaker as the system scales down. Meanwhile, the particles are more subject to thermal fluctuations. In addition, it becomes more difficult to image sub-micron particles. These are the barriers towards scaling down the lock-and-key interaction.

Efforts have been made to pattern sub-micron particles in defect-free director field through splay-band deformation. As a proof-of-concept, it was shown that chemically patterned surface can position particles with defined spacing. The surface consists of stripes of planar anchoring inside a global homeotropic director field. The top surface is also homeotropic.

So the stripes of planar anchoring creates splay bend deformation, which is used to position the particle with defined spacing [59].

The above results suggest that sub-micron particles can still migrate to locations of matching distortion to lower their energy. The mechanism is robust. We aim to accomplish here what Ref. [59] aims to accomplish by topographical features rather than chemical patterning. Here we demonstrate some preliminary results of velocity modulation as a $1 \mu m$ particle migrates through a corrugated surface consists of grooves ($\approx 1-2 \text{ cm}$ long in one direction, thickness s , width w , and depth $h = 2 \mu m$). We briefly describe the setup here: Instead of having the wavy strip sandwiched between glass slides, the grooves are confined under a glass slide (Fig. 6.12a). All the surfaces are treated to have homeotropic anchoring. Because of the resolution of lithography, the corners are rounded and have the similar undulated features as a wavy wall. The particle drifts along the top of the wall, due to residue flow from the phase transition. In most of the cases, the particle eventually docks and disappears from the field of view. We track the velocity of the particle (Fig. 6.12b). The particle moves faster when it approaches an edge, and slows down closes to the bottom of the groove. This observation indicates that the particles can indeed sense the presence of the wall, and the velocity is modulated by the splay and bend deformation sourced by the wall.

Ultimately, the grooves contains too many docking sites. It would be ideal if we have fewer, more targeted docking sites. One possible path forward is to spray particles onto an a freshly spin-coated SU8 substrate, and make a dimpled surface. The surface will than be baked to cure and replicated to make micron-sized wells. The surface is expected to provide sorting between smaller sized particles which can fit inside the well and bigger ones that cannot.

It is interesting to explore the possibility of nanometric assembly in the presence and absence of defect lines. We may take advantage of nanoparticle's tendency to be collected in the defect line [56, 111], and our ability to transform the defect configuration as a platform to controllably release these object. Yet exploration in the defect-free domain may prove

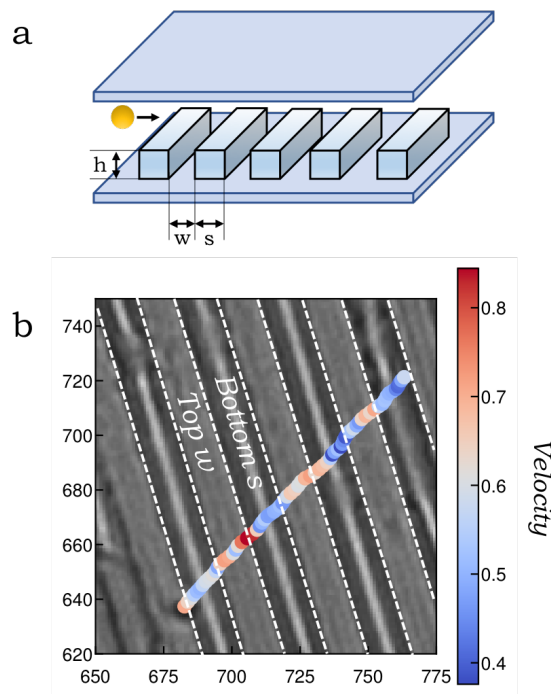


Figure 6.12: Scaling down of the lock-and-key interaction. (a) Schematic of the experimental setup. (b) Velocity tracking of a particle passing through the top of the grooves. The color bar shows the velocity of the particle, which is normalized with respect to the max velocity. The dotted line outlines the edges of the grooves.

equally fruitful. On a substrate with various indentations, particles can find equilibrium positions away from the base of the wells. These equilibrium state open up possibility in constructing meta-surfaces since the trapping energy is far less than that of a defect line in this case.

6.5. Assembly in other LC phases

There are examples of other LC phases in which elastic forces are different, where self-assembly is just as important and topological defects may play a much more prominent role. For instance, Smectic A (SmA) phase consists of layered structure. Within each layer, orientational order persists. In particular, SmA forms geometric defects called focal conic domains (FCDs) under appropriate boundary conditions [4, 37], that can be used as microlenses, enabled by the modulation of the refractive index within the layered structure of the defect [44, 46, 47]. Their arrangement can be tuned by topological features. In a collaborative project, we demonstrate a new approach to assemble smectic microlenses in micropillar arrays. These microlenses are stable, reconfigurable, polarization sensitive, and capable of focusing at different planes.

Chapter 7

Conclusion and outlook

In this thesis, we design the energy landscapes of non-singular director fields in confined NLC as tools to direct colloidal assembly. We demonstrate colloidal docking at preferred sites, migration along preferred paths, and formation of structures guided by the director field in two types of confining vessels. First, we study colloidal assembly in domains with wavy walls; thereafter, we study assembly in NLC filled grooves. To plan particle trajectories, dictate their interactions and define their docking sites, we have developed an understanding of how a particle interacts with its environment as well as with the energy landscape induced by these topographical cues.

In Chapter 3 & 4, we start by precisely positioning colloids with perpendicular anchoring on a wavy wall, at sites of complementary shape. The final position of the colloid depends on the orientation and the type of topological defects, as well as geometry of the well. By varying the width and depth of the wavy wall geometry, we create a platform that enables manipulation, particle selection, and a detailed study of defect structure under the influence of curvature. The characteristic range of influence is related to curvature of the wall. The distortion can be used to position particles, either in contact with the structure or at a distance. In this rich energy landscape, the particles can find more than one equilibrium position, and an external field can allow them to switch between these metastable states. An external field is applied to overcome the energy barriers, while the NLC elastic field guide the particles to precise docking site. We demonstrate that when a particle sediments due to gravity, parallel to wells of different sizes, the particle is able to achieve site selection based on the curvature of the wells.

In Chapter 5, we study colloidal dispersion in 5CB in a set of periodical, rectangular groove structures with homeotropic boundary conditions. This system with corners reveals rich behaviors not seen in cylindrical channels. By varying the geometrical parameters of the structure we observe two modes of assembly: through director field (“eyelashes”) and through defect lines (“pearl necklaces”) along the edge of the grooves. The mode of assembly is determined by the aspect ratio of the groove. The formation of these structures arises as a result of interplay between colloids and liquid crystal field in response to complex boundary conditions.

Chapter 6 highlights some preliminary directions where this research can move forward. The size, shape and orientation of the particles, as well as the boundary geometry must be taken into account to enable control over the resulting structures in this approach. Results summarized here clearly demonstrate that there is a significant potential for the NLC energy landscape to be used for robotics as well as nanomanufacturing.

We conclude with a concept map (Fig. 7.1). In this figure, I convey the breadth of the projects that interest me around this central theme of controlling the director fields in NLCs and smectics to direct colloid assembly. Throughout this experimental study, we guided our thinking by analogies to electrostatics, to capillary assembly, and to configurations that minimize distortions to the director field via splay matching or other arrangements. I aim to seek mechanistic understanding as well as to harness these interactions to make interesting structures and to develop new tools for materials assembly.

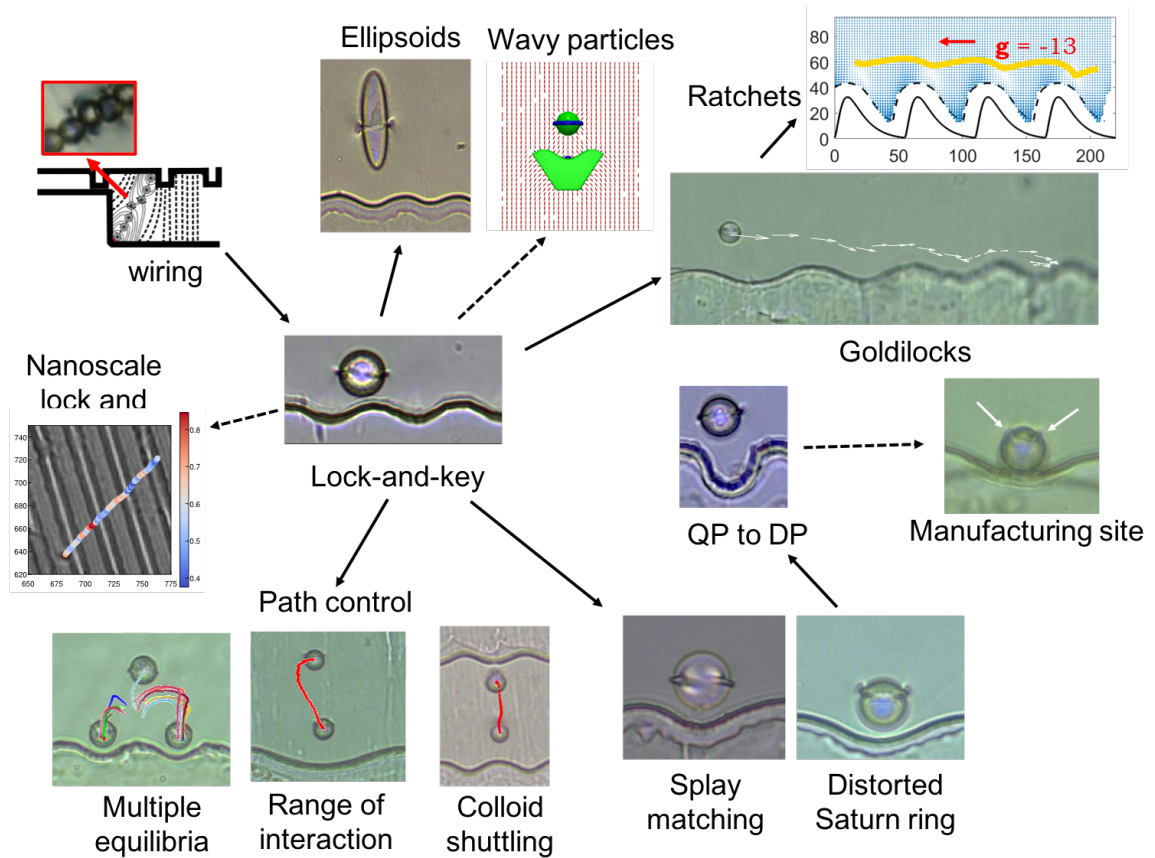


Figure 7.1: Concept map: Denoting how each ideas is connected to each other.

APPENDIX

APPENDIX A. Splay bend small slope analysis

Wall with homeotropic anchoring is located at

$$h(x) = A\cos(kx) \tag{B.1}$$

By using one-constant approximation, we can solve the Laplace Equation:

$$\nabla^2 \mathbf{n} = 0 \tag{B.2}$$

In two-dimension:

$$\begin{cases} \nabla^2 n_x = 0 \\ \nabla^2 n_y = 0 \end{cases} \tag{B.3}$$

$$\frac{\partial^2 n_x}{\partial x^2} + \frac{\partial^2 n_x}{\partial y^2} = 0 \tag{B.4}$$

Obtain general solution and n_x decays to zero at $y = \infty$, in the small slope limit ($kA \ll 1$),

$$n_x = (C_1 \sin(kx) + C_2 \cos(kx))e^{-ky} \tag{B.5}$$

Given boundary conditions (to order kA)

$$\begin{cases} n_x|_{wall} = A\sin(kx) \\ n_x|_{y=\infty} = 0 \end{cases} \tag{B.6}$$

At the wall we expand the expression to the order kA

$$e^{-ky}|_{wall} = e^{-A\cos(kx)} = 1 - A\cos(kx) + \mathcal{O}((kA)^2) \tag{B.7}$$

$$n_x = A\sin(kx)e^{-ky} \tag{B.8}$$

Assuming small variation in y

$$\begin{cases} n_y|_{wall} = 1 \\ n_y|_{y=\infty} = 1 \end{cases} \quad (\text{B.9})$$

$$n_y = 1 \quad (\text{B.10})$$

Locate the surface at

$$F = y - h(x) = 0 \quad (\text{B.11})$$

$$|\nabla F| = \sqrt{1 + \left(\frac{dh}{dx}\right)^2} \approx 1 \quad (\text{B.12})$$

The surface normal is expressed as:

$$\mathbf{n}|_{wall} \approx \nabla F = \mathbf{e}_y - \frac{\partial h}{\partial x} \mathbf{e}_x \quad (\text{B.13})$$

The splay energy density is calculated as

$$S = K(\nabla \cdot \mathbf{n})^2 \quad (\text{B.14})$$

Or

$$S = K(Ak^2)^2 \cos^2(kx) e^{-2ky} \quad (\text{B.15})$$

The bend energy density is calculated, where K is the elastic constant, $K \approx 10^{-11} N$

$$B = K(\mathbf{n} \times \nabla \times \mathbf{n})^2 \quad (\text{B.16})$$

Or

$$B = K(Ak^2)^2 \sin^2(kx) e^{-2ky} \quad (\text{B.17})$$

The total energy density in bulk liquid crystal due to disturbance owing to the structure, with one-constant approximation, in the small slope limit, is

$$S + B = K(Ak^2)^2 e^{-2ky} \quad (\text{B.18})$$

Therefore, we conclude that in this limit, the distortion due to the wall decays exponential into the bulk with characteristic decay length λ^{-1} . But otherwise the total energy remains constant at same y . However, the splay energy source by the colloid can couple to the splay energy component source by the wall and cause the colloid to migrate towards the wall.

APPENDIX B. Matlab routines

This file generates a wavy boundary of cross section specified by the curve, which consists of two intersecting arcs of sections of a sphere, the radius of the wall R and L of the section being simulated are inputs to the function which are included in the main file.

```
function y = hemi(x,R,L)
% R is the radius of the well
% L is the width of the well
x0 = L/2; % center of the curvature
5 y0 = R;
xi = L/4; % inflection point
yi = y0 - sqrt(R^2-(xi-x0)^2);
y1 = 2*yi-R;
x1 = 0;
10 y2 = y1;
x2 = L;

if x>=L/4 && x<3*L/4
    y = y0 - sqrt(R^2-(x-x0)^2);
15 elseif x>=3*L/4 && x<=L
    y = y2 + sqrt(R^2-(x-x2)^2);
elseif x<L/4 && x>=0
    y = y1 + sqrt(R^2-(x-x1)^2);
end
```

The curve has slope:

```
function dy = dhemi(x,R,L)
% R is the radius of the well
% L is the width of the well
x0 = L/2; % center of the curvature
```

```

5 y0 = R;

x0 = L/2; % center of the curvature
y0 = R;
xi = L/4; % inflection point
10 yi = y0 - sqrt(R^2-(xi-x0)^2);
y1 = 2*yi-R;
x1 = 0;
y2 = y1;
x2 = L;

15
if x>=L/4 && x<3*L/4
    dy = (x-x0)*(R^2-(x-x0)^2)^(-1/2);
elseif x>=3*L/4 && x<=L
    dy = -(x-x2)*(R^2-(x-x2)^2)^(-1/2);
20 elseif x<L/4 && x>=0
    dy = -(x-x1)*(R^2-(x-x1)^2)^(-1/2);
end

```

The following main file writes the file to introduce to the LdG code. Number of object and anchoring type and strength must be added in the beginning.

```

% This file takes the function shape and output to .dat file
% that specifies the wavy wall
% assuming periodic boundary condition in y
% define top (A1), bottom (A2), back (A3) and front surface (A4)
5
clc
clf
close all
clear all

```

```

10      %% Define thickness of the structure
      t = 60; %um, in z direction
      R = 90;
      L = 144;

15      % Define scale factor so x & y fall on grid
      % which also gives realistic shapes
      sf = 1;

20      % set grid x,y
      x = 0:1:L*sf-1;
      y = 0:1:20*sf-1;
      z = 0:1:t*sf-1;

25      % making XY indices
      [X1,Y1]=meshgrid(x,y);

      % reshape
      X1 = reshape(X1,1,[]);
30      Y1 = reshape(Y1,1,[]);
      xnew = X1(1);
      ynew = Y1(1);

      % the purpose of this loop is too find all interior points
35      for i = 1:length(X1)
          K1(i) = round(sf*hemi((X1(i)/sf),R,L));
          if Y1(i) < K1(i)
              xnew(end+1) = X1(i);
              ynew(end+1) = Y1(i);
40          end
      end
end

```

```

figure(1)
plot(xnew,ynew,'ko','MarkerSize',1)
45 hold on
plot(X1,K1,'r-','LineWidth',2)
axis equal tight
title('Top surface A1')

50 %% top (A1) + bottom (A2) surface
% initialize
A1 = zeros(length(xnew),7);
% first column, denote object # = 1
A1(:,1) = 1;
55 % give x, y, z coordinates
A1(:,2) = xnew; % x
A1(:,3) = ynew; % y
A1(:,4) = t*sf; % z-thickness of the cell

60 % define surface normals
A1(:,6) = 1; % nz

% bottom surface
A2 = A1;
65 A2(:,4) = 0; % located at zero
A2(:,6) = -1; % nz

%% back surface (A3)
[X3,Z3] = meshgrid(x,z);
70 % reshape
X3 = reshape(X3,1,[]);
Z3 = reshape(Z3,1,[]);
figure(2)

```

```

plot(X3,Z3,'ko','MarkerSize',1)
75 title('Back surface A3')
axis equal tight

% initialize
A3 = zeros(length(X3),7);
80

% first column, denote object # = 1
A3(:,1) = 1;

% give x, y, z coordinates
85 A3(:,2) = X3; % x
A3(:,3) = 0; % y
A3(:,4) = Z3; % z

% define surface normal
90 A3(:,6) = -1; % ny

%% wavy front surface (A4)
% same x,z coordinates as A3
X4 = X3;
95 Z4 = Z3;
for i = 1:length(X4)
Y4(i) = round(sf*hemi((X4(i)/sf),R,L));
end

100 % initialize
A4 = zeros(length(X4),7);
nx = zeros(length(X4),1);
ny = zeros(length(X4),1);

105 % first column, denote object # = 1

```

```

A4(:,1) = ones(length(X4),1);

% give x, y, z coordinates
A4(:,2) = X4'; % x
110 A4(:,3) = Y4'; % y
A4(:,4) = Z4'; % z

% define surface normal
for i = 1:length(X4)
115 nx(i) = -dhemis(X4(i)/sf,R,L);
end
ny = ones(length(nx),1);
nx = nx./sqrt(nx.^2+ny.^2);
ny = ny./sqrt(nx.^2+ny.^2);
120 A4(:,5) = nx; % nx
A4(:,6) = ny; % ny

figure(3)
plot(X4,Y4,'ko','MarkerSize',1)
125 hold on
%quiver(X4,Y4,nx',ny',1,'ShowArrowHead','off','LineWidth',1)
quiver(X4,Y4,nx',ny',1,'LineWidth',1)
axis equal tight
xlabel('x')
130 ylabel('y')

%% Find interior points
% the purpose of this loop is too find all interior points
X7 = 1;
135 Y7 = 1;

for i = 1:length(X1)

```

```

    K1(i) = round(sf*hemi(X1(i)/sf,R,L));
    if Y1(i) < K1(i) && Y1(i)>0
140       X7(end+1) = X1(i);
           Y7(end+1) = Y1(i);

        end
    end

145 figure(4)
    plot(X7,Y7,'ko','MarkerSize',1)
    hold on
    plot(X1,K1,'r-','LineWidth',2)
    axis equal tight
150 title('Top surface A1')

    A7 = zeros(length(z)*length(X7),7);
    A7(:,1)=1; % object#
    A7(:,5)=1; % nx

155 for m = 1:length(z)
        A7((m-1)*length(X7)+1:m*length(X7),2)=X7; % x
        A7((m-1)*length(X7)+1:m*length(X7),3)=Y7; % y
        A7((m-1)*length(X7)+1:m*length(X7),4)=z(m); % z
160 end

    % Open .dat files to write
    fid = fopen('conf_T_4a.dat','w');
    formatSpec = '%d %d %d %d %f %f %f\n';
165 fprintf(fid,formatSpec,A3'); % front surface
    fprintf(fid,formatSpec,A4'); % back surface
    fprintf(fid,formatSpec,A7'); % interior
    fclose(fid);

```

Finally, to fit an energy landscape, it is easiest to give Matlab some form of function to fit a set of data x, y, z where (x,y) are the coordinate and z is the energy at that point. The input does not have to be on a square grid. Here is a 5 variable fit for goldilocks' trajectory.

```
% fit data and plot
ft = fittype('a*cos(c/(d-e*x)*x)*exp(-b*(y+3))',...
'indepenent', {'x', 'y'}, 'dependent', {'z'},...
'coefficients',{'a','b','c','d','e'});
5 opts = fitoptions(ft);
opts.StartPoint = [500 0.1266 2*pi 55 0.32];
opts.Robust = 'LAR'; % robust fitting
[sf,gof] = fit([x1,y1],z1,ft,opts);
```

BIBLIOGRAPHY

- [1] Agha, H., Fleury, J.-B., and Galerne, Y. (2012). Micro-wires self-assembled and 3d-connected with the help of a nematic liquid crystal. *Eur. Phys. J. E*, 35(9):1–12.
- [2] Araki, T., Serra, F., and Tanaka, H. (2013). Defect science and engineering of liquid crystals under geometrical frustration. *Soft Matter*, 9(34):8107–8120.
- [3] Beller, D. A. (2014). *Controlling Defects in Nematic and Smectic Liquid Crystals Through Boundary Geometry*. PhD thesis, University of Pennsylvania.
- [4] Beller, D. A., Gharbi, M. A., Honglawan, A., Stebe, K. J., Yang, S., and Kamien, R. D. (2013). Focal conic flower textures at curved interfaces. *Phys. Rev. X*, 3:041026.
- [5] Beller, D. A., Gharbi, M. A., and Liu, I. B. (2015). Shape-controlled orientation and assembly of colloids with sharp edges in nematic liquid crystals. *Soft Matter*, 11(6):1078–1086.
- [6] Blanc, C., Coursault, D., and Lacaze, E. (2013). Ordering nano-and microparticles assemblies with liquid crystals. *Liquid Crystals Reviews*, 1(2):83–109.
- [7] Blow, M. L. and Telo da Gama, M. M. (2013). Interfacial motion in flexo-and order-electric switching between nematic filled states. *J. Phys. Condens. Matter*, 25(24):245103.
- [8] Brake, J. M., Mezera, A. D., and Abbott, N. L. (2003). Effect of surfactant structure on the orientation of liquid crystals at aqueous- liquid crystal interfaces. *Langmuir*, 19(16):6436–6442.
- [9] Brenner, H. (1961). The slow motion of a sphere through a viscous fluid towards a plane surface. *Chem. Eng. Sci.*, 16(3-4):242–251.
- [10] Brochard, F., Pieranski, P., and Guyon, E. (1972). Dynamics of the orientation of a nematic-liquid-crystal film in a variable magnetic field. *Phys. Rev. Lett.*, 28(26):1681.
- [11] Cavallaro, M., Gharbi, M. A., Beller, D. A., Čopar, S., Shi, Z., Baumgart, T., Yang, S., Kamien, R. D., and Stebe, K. J. (2013). Exploiting imperfections in the bulk to direct assembly of surface colloids. *Proc. Natl. Acad. Sci. U.S.A.*, 110(47):18804–18808.
- [12] Champion, J. A., Katare, Y. K., and Mitragotri, S. (2007). Making polymeric micro- and nanoparticles of complex shapes. *Proc. Natl. Acad. Sci. U.S.A.*, 104(29):11901–11904.
- [13] Champion, J. A. and Mitragotri, S. (2006). Role of target geometry in phagocytosis. *Proc. Natl. Acad. Sci. U.S.A.*, 103(13):4930–4934.
- [14] Chen, K., Gebhardt, O. J., Devendra, R., Drazer, G., Kamien, R. D., Reich, D. H., and Leheny, R. L. (2018). Colloidal transport within nematic liquid crystals with arrays of obstacles. *Soft Matter*, 14(1):83–91.

- [15] Chernyshuk, S. and Lev, B. (2011). Theory of elastic interaction of colloidal particles in nematic liquid crystals near one wall and in the nematic cell. *Phys. Rev. E*, 84(1):011707.
- [16] Crawford, G., Allender, D. W., and Doane, J. (1992). Surface elastic and molecular-anchoring properties of nematic liquid crystals confined to cylindrical cavities. *Phy. Rev. A*, 45(12):8693.
- [17] Damasceno, P. F., Engel, M., and Glotzer, S. C. (2011). Crystalline assemblies and densest packings of a family of truncated tetrahedra and the role of directional entropic forces. *Acs Nano*, 6(1):609–614.
- [18] Damasceno, P. F., Engel, M., and Glotzer, S. C. (2012). Predictive self-assembly of polyhedra into complex structures. *Science*, 337(6093):453–457.
- [19] Darmon, A., Benzaquen, M., Čopar, S., Dauchot, O., and Lopez-Leon, T. (2016). Topological defects in cholesteric liquid crystal shells. *Soft Matter*, 12(46):9280–9288.
- [20] del Campo, A. and Greiner, C. (2007). Su-8: a photoresist for high-aspect-ratio and 3d submicron lithography. *J. Micromechanics Microengineering*, 17(6):R81.
- [21] Dendukuri, D., Pregibon, D. C., Collins, J., Hatton, T. A., and Doyle, P. S. (2006). Continuous-flow lithography for high-throughput microparticle synthesis. *Nat. Mat.*, 5(5):365.
- [22] Dinsmore, A. D., Crocker, J. C., and Yodh, A. G. (1998). Self-assembly of colloidal crystals. *Curr. Opin. Colloid Interface Sci.*, 3(1):5–11.
- [23] Eskandari, Z., Silvestre, N. M., Telo da Gama, M. M., and Ejtehadi, M. R. (2014). Particle selection through topographic templates in nematic colloids. *Soft Matter*, 10(48):9681–9687.
- [24] Feynman, R. P., Leighton, R., and Sands, M. (1963). *Ratchet and pawl*, volume 1. Addison Wesley Reading, MA.
- [25] Fialho, A., Bernardino, N. R., Silvestre, N. M., and Telo da Gama, M. M. (2016). The effect of curvature on cholesteric doughnuts. *arXiv preprint arXiv:1608.01653*.
- [26] Fischer, E. (1894). Einfluss der configuration auf die wirkung der enzyme. *Ber. deutsch. chem. Gesell.*, 27(3):2985–2993.
- [27] Fleury, J.-B., Pires, D., and Galerne, Y. (2009). Self-connected 3d architecture of microwires. *Phys. Rev. Lett.*, 103(26):267801.
- [28] Ganatos, P., Pfeffer, R., and Weinbaum, S. (1980). A strong interaction theory for the creeping motion of a sphere between plane parallel boundaries. part 2. parallel motion. *J. Fluid Mech.*, 99(4):755–783.

- [29] Gennes, P.-G. D. and Prost, J. (1993). *The Physics of Liquid Crystals*. Oxford University Press.
- [30] Gharbi, M. A., Cavallaro Jr, M., Wu, G., Beller, D. A., Kamien, R. D., Yang, S., and Stebe, K. J. (2013). Microbullet assembly: Interactions of oriented dipoles in confined nematic liquid crystal. *Liq. Cryst.*, 40(12):1619–1627.
- [31] Glotzer, S. C. and Solomon, M. J. (2007). Anisotropy of building blocks and their assembly into complex structures. *Nat. Mat.*, 6(8):557.
- [32] Gu, Y. and Abbott, N. L. (2000). Observation of saturn-ring defects around solid microspheres in nematic liquid crystals. *Phys. Rev. Lett.*, 85(22):4719.
- [33] Guo, Y., Afghah, S., Xiang, J., Lavrentovich, O. D., Selinger, R. L., and Wei, Q.-H. (2016). Cholesteric liquid crystals in rectangular microchannels: skyrmions and stripes. *Soft Matter*, 12(29):6312–6320.
- [34] Halsey, T. C. and Toor, W. (1990). Structure of electrorheological fluids. *Phys. Rev. Lett.*, 65(22):2820.
- [35] Hegmann, T., Qi, H., and Marx, V. M. (2007). Nanoparticles in liquid crystals: Synthesis, self-assembly, defect formation and potential applications. *J. Inorg. Organomet. Polym. Mater.*, 17(3):483–508.
- [36] Ho, C., Keller, A., Odell, J., and Ottewill, R. (1993). Preparation of monodisperse ellipsoidal polystyrene particles. *Colloid Polym. Sci.*, 271(5):469–479.
- [37] Honglawan, A., Beller, D. A., Cavallaro, M., Kamien, R. D., Stebe, K. J., and Yang, S. (2011). Pillar-assisted epitaxial assembly of toric focal conic domains of smectic-a liquid crystals. *Adv. Mater.*, 23(46):5519–5523.
- [38] Hsieh, W.-T., Hsu, C.-J., Capraro, B. R., Wu, T., Chen, C.-M., Yang, S., and Baumgart, T. (2012). Curvature sorting of peripheral proteins on solid-supported wavy membranes. *Langmuir*, 28(35):12838–12843.
- [39] Hsu, C.-P., Ramakrishna, S. N., Zanini, M., Spencer, N. D., and Isa, L. (2018). Roughness-dependent tribology effects on discontinuous shear thickening. *Proc. Natl. Acad. Sci. U.S.A.*, page 201801066.
- [40] Hung, F. R., Gettelfinger, B. T., Koenig Jr, G. M., Abbott, N. L., and de Pablo, J. J. (2007). Nanoparticles in nematic liquid crystals: Interactions with nanochannels. *J. Chem. Phys.*, 127(12):124702.
- [41] Keuning, J. D., de Vriesy, J., Abelmann, L., and Misra, S. (2011). Image-based magnetic control of paramagnetic microparticles in water. In *Intelligent Robots and Systems (IROS), 2011 IEEE/RSJ International Conference on*, pages 421–426. IEEE.

- [42] Khullar, S., Zhou, C., and Feng, J. J. (2007). Dynamic evolution of topological defects around drops and bubbles rising in a nematic liquid crystal. *Phys. Rev. Lett.*, 99(23):237802.
- [43] Kim, J., Hwang, H. J., Oh, J. S., Sacanna, S., and Yi, G.-R. (2018). Monodisperse magnetic silica hexapods. *J. Am. Chem. Soc.*
- [44] Kim, J. H., Kim, Y. H., Jeong, H. S., Srinivasarao, M., Hudson, S. D., and Jung, H.-T. (2012). Thermally responsive microlens arrays fabricated with the use of defect arrays in a smectic liquid crystal. *RSC Adv.*, 2:6729–6732.
- [45] Kim, J.-W., Larsen, R. J., and Weitz, D. A. (2007). Uniform nonspherical colloidal particles with tunable shapes. *Adv. Mater.*, 19(15):2005–2009.
- [46] Kim, Y. H., Jeong, H. S., Kim, J. H., Yoon, E. K., Yoon, D. K., and Jung, H.-T. (2010a). Fabrication of two-dimensional dimple and conical microlens arrays from a highly periodic toroidal-shaped liquid crystal defect array. *J. Mater. Chem.*, 20:6557–6561.
- [47] Kim, Y. H., Lee, J.-O., Jeong, H. S., Kim, J. H., Yoon, E. K., Yoon, D. K., Yoon, J.-B., and Jung, H.-T. (2010b). Optically selective microlens photomasks using self-assembled smectic liquid crystal defect arrays. *Adv. Mater.*, 22(22):2416–2420.
- [48] Kléman, M. (1989). Defects in liquid crystals. *Rep. Prog. Phys.*, 52(5):555.
- [49] König, P.-M., Roth, R., and Dietrich, S. (2009). Lock and key model system. *Eur. Phys. J.*, 84(6):68006.
- [50] Kurihara, S., Ohta, K., Oda, T., Izumi, R., Kuwahara, Y., Ogata, T., and Kim, S.-N. (2013). Manipulation and assembly of small objects in liquid crystals by dynamical disorganizing effect of push-pull-azobenzene-dye. *Sci. Rep.*, 3:2167.
- [51] Lapointe, C., Hultgren, A., Silevitch, D., Felton, E., Reich, D., and Leheny, R. (2004). Elastic torque and the levitation of metal wires by a nematic liquid crystal. *Science*, 303(5658):652–655.
- [52] Lapointe, C. P., Mason, T. G., and Smalyukh, I. I. (2009). Shape-controlled colloidal interactions in nematic liquid crystals. *Science*, 326(5956):1083–1086.
- [53] Lavrentovich, O. D. (1998). Topological defects in dispersed words and worlds around liquid crystals, or liquid crystal drops. *Liq. Cryst.*, 24(1):117–126.
- [54] Lavrentovich, O. D. (2014). Transport of particles in liquid crystals. *Soft Matter*, 10(9):1264–1283.
- [55] Lee, D., Cohen, R. E., and Rubner, M. F. (2007). Heterostructured magnetic nanotubes. *Langmuir*, 23(1):123–129.

- [56] Lee, E., Xia, Y., Ferrier, R. C., Kim, H.-N., Gharbi, M. A., Stebe, K. J., Kamien, R. D., Composto, R. J., and Yang, S. (2016). Fine golden rings: tunable surface plasmon resonance from assembled nanorods in topological defects of liquid crystals. *Adv. Mater.*, 28(14):2731–2736.
- [57] Legge, C. and Mitchell, G. (1992). Photo-induced phase transitions in azobenzene-doped liquid crystals. *J. Phys. D*, 25(3):492.
- [58] Li, N., Sharifi-Mood, N., Tu, F., Lee, D., Radhakrishnan, R., Baumgart, T., and Stebe, K. J. (2016). Curvature-driven migration of colloids on tense lipid bilayers. *Langmuir*, 33(2):600–610.
- [59] Li, X., Armas-Pérez, J. C., Hernández-Ortiz, J. P., Arges, C. G., Liu, X., Martinez-Gonzalez, J. A., Ocola, L. E., Bishop, C., Xie, H., de Pablo, J. J., et al. (2017). Directed self-assembly of colloidal particles onto nematic liquid crystalline defects engineered by chemically patterned surfaces. *ACS Nano*, 11(6):6492–6501.
- [60] Lin, I.-H., Miller, D. S., Bertics, P. J., Murphy, C. J., de Pablo, J. J., and Abbott, N. L. (2011). Endotoxin-induced structural transformations in liquid crystalline droplets. *Science*, 332(6035):1297–1300.
- [61] Lintuvuori, J., Pawsey, A., Stratford, K., Cates, M., Clegg, P., and Marenduzzo, D. (2013). Colloidal templating at a cholesteric-oil interface: Assembly guided by an array of disclination lines. *Phys. Rev. Lett.*, 110(18):187801.
- [62] Liu, I. B., Gharbi, M. A., Ngo, V. L., Kamien, R. D., Yang, S., and Stebe, K. J. (2015). Elastocapillary interactions on nematic films. *Proc. Natl. Acad. Sci. U.S.A.*, 112(20):6336–6340.
- [63] Loudet, J.-C., Mondain-Monval, O., and Poulin, P. (2002). Line defect dynamics around a colloidal particle. *Eur. Phys. J. E*, 7(3):205–208.
- [64] Loudet, J.-C. and Poulin, P. (2001). Application of an electric field to colloidal particles suspended in a liquid-crystal solvent. *Phys. Rev. Lett.*, 87(16):165503.
- [65] Lubensky, T. C., Pettey, D., Currier, N., and Stark, H. (1998). Topological defects and interactions in nematic emulsions. *Phys. Rev. E*, 57(1):610.
- [66] Luo, Y., Beller, D. A., Boniello, G., Serra, F., and Stebe, K. J. (2018). Tunable colloid trajectories in nematic liquid crystals near wavy walls. *Nat. Comm.*, 9(1):3841.
- [67] Luo, Y., Serra, F., Beller, D. A., Gharbi, M. A., Li, N., Yang, S., Kamien, R. D., and Stebe, K. J. (2016a). Around the corner: Colloidal assembly and wiring in groovy nematic cells. *Phys. Rev. E*, 93(3):032705.
- [68] Luo, Y., Serra, F., and Stebe, K. J. (2016b). Experimental realization of the “lock-and-key” mechanism in liquid crystals. *Soft Matter*, 12(28):6027–6032.

- [69] Manoharan, V. N. (2015). Colloidal matter: Packing, geometry, and entropy. *Science*, 349(6251):1253751.
- [70] Matczyszyn, K. and Sworakowski, J. (2003). Phase change in azobenzene derivative-doped liquid crystal controlled by the photochromic reaction of the dye. *J. Phys. Chem. B*, 107(25):6039–6045.
- [71] McConney, M., Martinez, A., Tondiglia, V., Lee, K., Langley, D., Smalyukh, I., and White, T. (2013). Topography from topology: photoinduced surface features generated in liquid crystal polymer networks. *Adv. Mater.*, 25:5880.
- [72] Mottram, N. J. and Newton, C. J. (2014). Introduction to Q-tensor theory. *arXiv preprint arXiv:1409.3542*.
- [73] Muševič, I., Škarabot, M., Tkalec, U., Ravnik, M., and Žumer, S. (2006). Two-dimensional nematic colloidal crystals self-assembled by topological defects. *Science*, 313(5789):954–958.
- [74] Nikkhou, M., Skarabot, M., Copar, S., Ravnik, M., Zumer, S., and Musevic, I. (2015). Light-controlled topological charge in a nematic liquid crystal. *Nature physics*, 11(2):183.
- [75] Nobili, M. and Durand, G. (1992). Disorientation-induced disordering at a nematic-liquid-crystal–solid interface. *Phys. Rev. A*, 46(10):R6174.
- [76] Nych, A., Ognysta, U., Škarabot, M., Ravnik, M., Žumer, S., and Muševič, I. (2013). Assembly and control of 3d nematic dipolar colloidal crystals. *Nat. Comm.*, 4:1489.
- [77] Ohzono, T. and Fukuda, J.-I. (2012). Zigzag line defects and manipulation of colloids in a menatic liquid crystal microwrinkle groove. *Nat. Comm.*, 3:1709.
- [78] O’Neill, M. E. (1964). A slow motion of viscous liquid caused by a slowly moving solid sphere. *Mathematika*, 11(01):67–74.
- [79] Orlova, T., Abhoff, S. J., Yamaguchi, T., Katsonis, N., and Brasselet, E. (2015). Creation and manipulation of topological states in chiral nematic microspheres. *Nat. Comm.*, 6:7603.
- [80] Peng, C., Guo, Y., Conklin, C., Viñals, J., Shiyankovskii, S. V., Wei, Q.-H., and Lavrentovich, O. D. (2015). Liquid crystals with patterned molecular orientation as an electrolytic active medium. *Phys. Rev. E*, 92(5):052502.
- [81] Peng, C., Turiv, T., Guo, Y., Shiyankovskii, S. V., Wei, Q.-H., and Lavrentovich, O. D. (2016a). Control of colloidal placement by modulated molecular orientation in nematic cells. *Sci. Adv.*, 2(9):e1600932.
- [82] Peng, C., Turiv, T., Zhang, R., Guo, Y., Shiyankovskii, S. V., Wei, Q.-H., de Pablo, J., and Lavrentovich, O. D. (2016b). Controlling placement of nonspherical (boomerang)

- colloids in nematic cells with photopatterned director. *Journal of Physics: Condensed Matter*, 29(1):014005.
- [83] Pires, D., Fleury, J.-B., and Galerne, Y. (2007). Colloid particles in the interaction field of a disclination line in a nematic phase. *Phys. Rev. Lett.*, 98(24):247801.
- [84] Pishnyak, O. P., Tang, S., Kelly, J., Shiyanovskii, S. V., and Lavrentovich, O. D. (2007). Levitation, lift, and bidirectional motion of colloidal particles in an electrically driven nematic liquid crystal. *Phys. Rev. Lett.*, 99(12):127802.
- [85] Poulin, P., Stark, H., Lubensky, T., and Weitz, D. (1997). Novel colloidal interactions in anisotropic fluids. *Science*, 275(5307):1770–1773.
- [86] Poulin, P. and Weitz, D. (1998). Inverted and multiple nematic emulsions. *Phys. Rev. E*, 57(1):626.
- [87] Rasing, T. and Musevic, I. (2004). *Surfaces and Interfaces of Liquid Crystals*. Springer-Verlag Berlin Heidelberg.
- [88] Ravnik, M., Škarabot, M., Žumer, S., Tkalec, U., Poberaj, I., Babič, D., Osterman, N., and Muševič, I. (2007). Entangled nematic colloidal dimers and wires. *Physical Review Letters*, 99(24):247801.
- [89] Ravnik, M. and Žumer, S. (2009). Landau–de gennes modelling of nematic liquid crystal colloids. *Liq. Cryst.*, 36(10-11):1201–1214.
- [90] Sacanna, S., Irvine, W., Chaikin, P. M., and Pine, D. J. (2010). Lock and key colloids. *Nature*, 464(7288):575–578.
- [91] Sengupta, A., Bahr, C., and Herminghaus, S. (2013). Topological microfluidics for flexible micro-cargo concepts. *Soft Matter*, 9(30):7251–7260.
- [92] Senyuk, B., Liu, Q., Bililign, E., Nystrom, P. D., and Smalyukh, I. I. (2015). Geometry-guided colloidal interactions and self-tiling of elastic dipoles formed by truncated pyramid particles in liquid crystals. *Phy. Rev. E*, 91(4):040501.
- [93] Senyuk, B., Liu, Q., Nystrom, P. D., and Smalyukh, I. I. (2017). Repulsion–attraction switching of nematic colloids formed by liquid crystal dispersions of polygonal prisms. *Soft Matter*, 13(40):7398–7405.
- [94] Serra, F. (2016). Curvature and defects in nematic liquid crystals. *Liq. Cryst.*, 43(13-15):1920–1936.
- [95] Silvestre, N. M., Eskandari, Z., Patrício, P., Romero-Enrique, J. M., and Telo da Gama, M. (2012). Nematic wetting and filling of crenellated surfaces. *Phys. Rev. E*, 86(1):011703.
- [96] Silvestre, N. M., Liu, Q., Senyuk, B., Smalyukh, I. I., and Tasinkevych, M. (2014). Towards template-assisted assembly of nematic colloids. *Phys. Rev. Lett.*, 112(22):225501.

- [97] Silvestre, N. M., Patrício, P., and Telo da Gama, M. M. (2004). Key-lock mechanism in nematic colloidal dispersions. *Phys. Rev. E*, 69(6):061402.
- [98] Škarabot, M., Ravnik, M., Žumer, S., Tkalec, U., Poberaj, I., Babič, D., and Mušević, I. (2008a). Hierarchical self-assembly of nematic colloidal superstructures. *Phy. Rev. E*, 77(6):061706.
- [99] Škarabot, M., Ravnik, M., Žumer, S., Tkalec, U., Poberaj, I., Babič, D., Osterman, N., and Mušević, I. (2008b). Interactions of quadrupolar nematic colloids. *Phy. Rev. E*, 77(3):031705.
- [100] Smalyukh, I. I. and Lavrentovich, O. (2002). Three-dimensional director structures of defects in grandjean-cano wedges of cholesteric liquid crystals studied by fluorescence confocal polarizing microscopy. *Phys. Rev. E*, 66(5):051703.
- [101] Smalyukh, I. I., Shiyankovskii, S., and Lavrentovich, O. (2001). Three-dimensional imaging of orientational order by fluorescence confocal polarizing microscopy. *Chemical Physics Letters*, 336(1-2):88–96.
- [102] Stark, H. (1999). Director field configurations around a spherical particle in a nematic liquid crystal. *Eur. Phys. J. B*, 10(2):311–321.
- [103] Stark, H. (2001). Physics of colloidal dispersions in nematic liquid crystals. *Phys. Rep.*, 351(6):387–474.
- [104] Stark, H. (2002a). Saturn-ring defects around microspheres suspended in nematic liquid crystals: an analogy between confined geometries and magnetic fields. *Phys. Rev. E*, 66:032701.
- [105] Stark, H. (2002b). Saturn-ring defects around microspheres suspended in nematic liquid crystals: an analogy between confined geometries and magnetic fields. *Phys. Rev. E*, 66(3):032701.
- [106] Tasinkevych, M., Mondiot, F., Mondain-Monval, O., and Loudet, J.-C. (2014). Dispersions of ellipsoidal particles in a nematic liquid crystal. *Soft Matter*, 10(12):2047–2058.
- [107] Terentjev, E. (1995). Disclination loops, standing alone and around solid particles, in nematic liquid crystals. *Phys. Rev. E*, 51(2):1330.
- [108] Tkalec, U. and Mušević, I. (2013). Topology of nematic liquid crystal colloids confined to two dimensions. *Soft Matter*, 9(34):8140–8150.
- [109] Tourdot, R. W., Ramakrishnan, N., Baumgart, T., and Radhakrishnan, R. (2015). Application of a free-energy-landscape approach to study tension-dependent bilayer tubulation mediated by curvature-inducing proteins. *Phys. Rev. E*, 92(4):042715.
- [110] Vilfan, M., Osterman, N., Čopič, M., Ravnik, M., Žumer, S., Kotar, J., Babič, D.,

- and Poberaj, I. (2008). Confinement effect on interparticle potential in nematic colloids. *Phys. Rev. Lett.*, 101(23):237801.
- [111] Wang, X., Kim, Y.-K., Bukusoglu, E., Zhang, B., Miller, D. S., and Abbott, N. L. (2016a). Experimental insights into the nanostructure of the cores of topological defects in liquid crystals. *Phys. Rev. Lett.*, 116(14):147801.
- [112] Wang, X., Miller, D. S., Bukusoglu, E., De Pablo, J. J., and Abbott, N. L. (2016b). Topological defects in liquid crystals as templates for molecular self-assembly. *Nature materials*, 15(1):106.
- [113] Whitmer, J. K., Wang, X., Mondiot, F., Miller, D. S., Abbott, N. L., and de Pablo, J. J. (2013). Nematic-field-driven positioning of particles in liquid crystal droplets. *Physical review letters*, 111(22):227801.
- [114] Xia, Y., Cedillo-Servin, G., Kamien, R. D., and Yang, S. (2016). Guided folding of nematic liquid crystal elastomer sheets into 3d via patterned 1d microchannels. *Adv. Mater.*, 28(43):9637–9643.
- [115] Xia, Y., Serra, F., Kamien, R. D., Stebe, K. J., and Yang, S. (2015). Direct mapping of local director field of nematic liquid crystals at the nanoscale. *Proc. Natl. Acad. Sci. U.S.A.*, 112(50):15291–15296.
- [116] Yi, G.-R., Pine, D. J., and Sacanna, S. (2013). Recent progress on patchy colloids and their self-assembly. *J. Phys. Condens. Matter*, 25(19):193101.
- [117] Yoshida, H., Asakura, K., Fukuda, J., and Ozaki, M. (2015). Three-dimensional positioning and control of colloidal objects utilizing engineered liquid crystalline defect networks. *Nat. Comm.*, 6:7180.
- [118] Zappone, B. and Lacaze, E. (2008). Surface-frustrated periodic textures of smectic-a liquid crystals on crystalline surfaces. *Physical Review E*, 78(6):061704.